Dissertation
submitted to the
Combined Faculty of Mathematics, Engineering and Natural Sciences
of Heidelberg University, Germany
for the degree of
Doctor of Natural Sciences

Put forward by
David Wachs
born in Herdecke, Germany

Oral examination: May 14, 2025

Atom Trap Trace Analysis of ^{39}Ar: Method Development and Application to Glacier Ice Dating

Referees: Prof. Dr. Werner Aeschbach
Prof. Dr. Norbert Frank

Abstract

Glacier ice stores a unique range of past environmental signals and therefore serves as an invaluable archive of Earth's climatic history. However, to fully exploit this archive, the knowledge of the age distribution of the ice is key. Radiometric dating methods are an important addition to traditional age dating techniques like annual layer counting, especially when these fail due to discontinuities in the record.
This thesis aims to establish the ^{39}Ar dating tracer as a well-understood tool for dating glacier ice. The advent of the atom-optical Atom Trap Trace Analysis (ATTA) technology for ^{39}Ar measurements has been associated with a significant reduction of required sample sizes and the tracer can therefore now routinely be applied to glacier ice.
As a major part of this thesis, the ATTA laboratory in Heidelberg was improved to deliver higher atom count rates for high-quality measurements with large long-term sample throughput.
Furthermore, two studies on Alpine glaciers are presented in this thesis, the summit glacier of Weissseespitze, where part of a 6000 a continuous record was dated, and the Jamtalferner, which is a much younger, highly variable low-altitude glacier. In both campaigns, ^{39}Ar ages are complemented by other tracer ages from radiocarbon or tritium, emphasizing the importance of this tracer in covering the full age range found in Alpine glaciers.
The specific requirements for the application of ^{39}Ar dating to glacier ice are investigated by comparing different ice sampling and sample preparation techniques. Additionally, the diffusion of argon in ice is quantified by ^{39}Ar measurements on a long-stored ice core, showing the negligibility of contamination via this pathway for storage times below several decades.
Finally, to make ^{39}Ar, and also the gaseous dating tracers ^{81}Kr and ^{85}Kr, more conveniently applicable to ice dating, a new gas extraction system was designed, tested and applied to an Antarctic ice core. It enables the gas extraction from the otherwise unused waste line of a continuous flow analysis.

Zusammenfassung

Gletschereis speichert eine einzigartige Bandbreite an historischen Umweltsignalen und dient daher als wertvolles Archiv für die Klimageschichte der Erde. Um diesem Datenschatz jedoch vollständig nutzen zu können, ist die Kenntnis der Altersverteilung des Eises von großer Bedeutung. Radiometrische Datierungsmethoden sind eine wichtige Ergänzung zu traditionellen Altersbestimmungstechniken wie der Zählung von Jahresschichten, insbesondere wenn diese aufgrund von diskontinuierlicher Schichtung versagen.
Das Ziel dieser Dissertation ist es, den ^{39}Ar-Tracer als ausgereifte Methode zur Datierung von Gletschereis zu etablieren. Der Fortschritt der atom-optischen Atom Trap Trace Analysis (ATTA)-Technologie für ^{39}Ar-Messungen hat zu einer erheblichen Reduktion der benötigten Probenmengen geführt, sodass Gletschereis nun routinemäßig auf diesen Spurenstoff hin untersucht werden kann.
Ein wesentlicher Bestandteil dieser Arbeit war die Optimierung des ATTA-Labors in Heidelberg, mit dem Ziel höhere Atomzählraten zu erreichen und damit qualitativ hochwertige Messungen mit nachhaltig hohem Probendurchsatz zu ermöglichen.
Darüber hinaus werden in dieser Dissertation zwei Studien über alpine Gletscher vorgestellt: ein 6000 Jahre zurückreichender, kontinuierlicher Datensatz vom Gipfelgletscher der Weißseespitze, sowie ein Datensatz vom deutlich jüngeren, niedrig gelegenen und stark variierenden Jamtalferner. In beiden Untersuchungen werden ^{39}Ar-Altersdaten um die Altersbestimmung mittels Radiokohlenstoff oder Tritium ergänzt, wodurch die Bedeutung von ^{39}Ar für die Abdeckung des gesamten Altersspektrums alpiner Gletscher hervorgehoben wird.
Die spezifischen Anforderungen der ^{39}Ar-Altersdatierungsmethode werden herausgearbeitet, indem verschiedene Techniken bei der Probennahme und -aufbereitung miteinander vergleichen werden.
Durch Bestimmung der ^{39}Ar-Gehalte in einem lang gelagerten Eisbohrkern, konnte die Diffusion von Argon in Eis quantifiziert und so gezeigt werden, dass die Kontamination durch diesen Prozess für Lagerzeiten von einigen Jahrzehnten vernachlässigbar ist.
Zu guter Letzt wurde ein neues Gasextraktionssystem entwickelt, getestet und auf einen antarktischen Eisbohrkern angewendet, um ^{39}Ar sowie die ebenfalls gasförmigen Datierungstracer ^{81}Kr und ^{85}Kr besser für die Altersdatierung von Eis nutzbar zu machen. Dieses System ermöglicht die Gasextraktion aus der bisher ungenutzten Überlaufleitung eines Continuous Flow Analysis Systems.

Contents

Frequently Used Abbreviations

ACT activated charcoal trap
AMS Accelerator Mass Spectrometry
AOM Acousto Optical Modulator
APD Avalanche Photo Diode
ArTTA Argon Trap Trace Analysis
a.s.l. above sea level
ATTA Atom Trap Trace Analysis
BI beam imaging (usually ^{40}Ar)
BP before present (before the year 1950)
BCE Before Common Era
CE Common Era
CFA continuous flow analysis
Col collimator (referring to the transversal cooling stage as well as its laser)
IUP Institute of Environmental Physics, Heidelberg
KIP Kirchhoff-Institute for Physics, Heidelberg
LIA Little Ice Age
LLC Low Level Counting
LR loading rate (usually ^{38}Ar)
LSS last steady state
MC Monte Carlo method based on repeated random sampling
m.i.e. meters ice equivalent
MOL Magneto Optical Lense
MOT Magneto Optical Trap
m.w.e. meters water equivalent
NPBS non-polarizing beam splitter
PBS polarizing beam splitter
PDF probability density function
QMS quadrupole mass spectrometer
RF radio frequency
STP standard temperature and pressure
WSS Weissseespitze
TMP turbo molecular pump
TU tritium unit
TA tapered amplifier
ZSL Zeeman slower (referring to the vaccuum part as well as the laser)

1 Introduction

Glacier ice represents one of the most invaluable natural archives of Earth's climatic history. Over millennia, glaciers have steadily accumulated layers of snow that, once compacted into ice, encapsulate a wealth of information, from atmospheric gas compositions and aerosol depositions to stable water isotopes and trace impurity content. Their frozen layers serve as time capsules, recording natural climatic variability and anthropogenic influences. As such, ice cores derived from glaciers have fundamentally reshaped our understanding of past climate dynamics, offering insights that range from shifts in temperature and precipitation patterns to broader changes in atmospheric circulation and biogeochemical cycles.

Polar ice records, with their exceptional longevity and relatively undisturbed stratigraphy, have been critical in delineating Earth's climatic transitions over hundreds of thousands of years (e.g. EPICA community members, 2004; NEEM community members, 2013). Yet, despite their profound contributions, polar records are not without limitations. Their remote locations and distinct meteorological conditions mean that they might not fully capture the nuances of climate variability experienced in more densely inhabited regions (Bohleber, 2019).

In contrast, Alpine glaciers offer a complementary and, in many ways, equally essential perspective. Located in mountain ranges that are often in close proximity to major population centers and industrial areas, Alpine ice cores integrate signals of both natural processes and localized anthropogenic impacts. These mid-latitude archives, although sometimes challenged by complexities such as discontinuous layering due to episodic mass loss, can provide higher temporal resolution records that are directly relevant to regions where human activities and natural environmental changes are taking place. Moreover, the dense network of historical instrumental climate records in these regions provides a unique opportunity to cross-validate and calibrate the proxy signals retrieved from Alpine ice. This integration not only deepens our understanding of recent climatic shifts, such as those observed during the Little Ice Age, but also enhances the predictive power of contemporary climate models.

One of the fundamental challenges in interpreting glacier ice as a paleo-climatic archive is establishing a robust age scale. The stratigraphy not only records environmental signals but also encapsulates the history of snow accumulation and glacier growth. In cases where a hiatus in accumulation is followed by renewed glacier growth, a distinct discontinuity arises in the age-depth profile, leading to significantly younger ice above the break. For cold-based glaciers below 4000 m a.s.l. (a target of

this project), the annual deposition of layers is not guaranteed. Furthermore, with the pronounced mass loss of glaciers in recent decades, even surface ages become unknown and can exhibit magnitudes of several centuries. Consequently, the method of annual layer counting becomes unfeasible, and age constraints must be derived solely from radiometric dating techniques. This reliance on radiometric methods is crucial for constructing an accurate chronology, which in turn underpins the paleo-climatic interpretation of the glacier ice record.

For dating glacier ice from the past century, isotopes such as ^{3}H ($T_{1/2}$ = 12.32 a) and ^{210}Pb ($T_{1/2}$ = 22.3 a) are routinely used (Gäggeler et al., 1983; Eichler et al., 2000). In contrast, recent advancements in micro-radiocarbon techniques, which analyze microscopic organic material from glacier ice, have become essential for samples older than approximately 1000 a (Uglietti et al., 2016; Hoffmann et al., 2018). However, micro-^{14}C dating is susceptible to misinterpretation due to contamination, reservoir effects, and possible in-situ production, and these issues have yet to be fully quantified (May, 2009; Hoffmann, 2016; Hoffmann et al., 2018). Additionally, for ice younger than about 1000 a, the ^{14}C method is limited by calibration uncertainties (Ramsey, 1995). Many European Alpine glaciers do not reach ages suitable for ^{14}C dating, often representing remnants of the Little Ice Age, with the majority of their stratigraphy being substantially younger. This creates an urgent need for radiometric dating methods that can accurately date glacier ice in the 100 to 1000 a range.

The noble gas radioisotope ^{39}Ar, with $T_{1/2} = 268 \pm 3$ a (Golovko, 2023), offers an ideal solution for this gap by covering a dating range of 50 to 1000 a, a period for which no other radiometric dating method is available (Loosli, 1983). This dating window is also critical for applications in groundwater management, ocean circulation studies, and climate archives (Lu et al., 2014). Since ^{39}Ar as a noble gas is not involved in geochemical processes, has a well-defined atmospheric source, and a constrained atmospheric input function (Gu et al., 2021; Happel, 2024), it is ideally suited for dating purposes. Yet, its extremely low isotopic abundance in air (^{39}Ar/Ar $= 8.1 \times 10^{-16}$, Collon et al., 2004a) has, until now, limited its routine use. Traditional measurements via Low-Level Counting (LLC) in an underground laboratory at the University of Bern require extensive measuring times (8-60 days) and large water samples (1-3 metric tons), rendering LLC impractical for routine glacier ice dating, even though some polar ice sheet studies have been conducted (Loosli, 1983).

Atom Trap Trace Analysis (ATTA) is an atom-optical technique initially developed for rare Kr isotopes (Chen et al., 1999) and has now been adapted for routine analysis (Jiang et al., 2012), including applications to polar ice (Buizert et al., 2014). By exploiting the high selectivity of resonant photon scattering during laser cooling, ATTA can effectively distinguish the rare ^{39}Ar isotope from its abundant counterparts. This approach, independent of the isotope's half-life, enables rapid analysis with relatively small sample sizes, opening the door to a wide array of applications in Earth and environmental sciences (Lu et al., 2014). At the Kirchhoff-Institute

for Physics in Heidelberg (KIP), a specialized ATTA setup for ^{39}Ar (ArTTA) has been developed. Initial experiments demonstrated its capability for dating large groundwater samples (Ritterbusch et al., 2014), and subsequent improvements have reduced the required sample size to just a few ml STP of Ar (Ebser et al., 2018). For example, obtaining 3 ml STP of Ar now permits practical dating of ocean water (from 10 l). A first effort for ice dating with ^{39}Ar was conducted by Feng et al. (2019), showing the feasibility of measurements of 4-7 kg of ice (yielding 0.5-1.7 ml STP of Ar). Subsequently, ^{39}Ar measurements on ice were used by Ritterbusch et al. (2022) to establish an age scale for an ice core from the Tibetan plateau.

This thesis aims to establish the ^{39}Ar dating technique as a well-understood tool for glacier ice. In order to achieve a common basis and build a general understanding of the atom-optical processes involved, chapter 2 gives an overview of the fundamental concepts of atom trapping. An introduction to the formation and dynamics of glaciers is given in chapter 3, also addressing different age-depth models that can explain age-gradients in an ice sheet and introducing the basic concepts of diffusion of gases in ice.
In chapter 4, the different methods involved in the presented work are discussed: from ice sampling methods in the field to the gas extraction from ice samples and the subsequent measurements in the ATTA laboratory. For the latter, the ATTA apparatus and its components as well as the measurement routine are discussed. Furthermore, an improved analysis of the ATTA measurements that was developed in a partly-supervised master thesis by Kindermann (2024) during the time of this project is introduced. After these three introductory chapters, the focus is turned toward the methodological results of this thesis and the applications to glacier age dating.
While the results presented here mostly concern glacier ice dating and its different aspects, the actual majority of the work during this thesis was done in the ATTA laboratory. Optimizing the system to a good performance and ensuring stability upon reaching it cost large amounts of time and effort. The key findings regarding the optimization of the apparatus and its stable operation are discussed in chapter 5. Furthermore, the parallel project of establishing an online database for all ATTA samples is shortly introduced.
The first methodological aspect of dating glacier ice with ^{39}Ar, treated in chapter 6, is the investigation of possible Ar diffusion into ice during storage. As the collision diameter of Ar is on the threshold of gases with significant diffusion in ice (Huber et al., 2006), the question of maximum storage times before an ^{39}Ar analysis and the key aspects affecting the diffusion are explored.
In chapters 7 and 8, two campaigns of ^{39}Ar dating of Alpine glaciers are presented which were conducted in collaboration with colleagues from the Institute for Interdisciplinary Mountain Research in Innsbruck, Austria. First, the summit glacier at Weissseespitze (WSS), exhibiting a continuous age record reaching back 6000 a, is discussed. ^{39}Ar age data in combination with ^{14}C ages allows a full coverage of its profile. With this, an age model can be fitted and thus a continuous age-depth profile

that can be applied to other depth-resolved tracer data is established. In the second application, the Jamtalferner glacier is explored, which exhibits ages below 300 a for most of its extent. Together with ^{3}H data and findings from human activities in the valley, the picture of a transient glacier closely impacting the life around it over time is drawn.
Chapter 9 tackles a general problem that ATTA measurements of ice samples encounter. For ^{39}Ar, as well as the other ATTA tracers ^{85}Kr and ^{81}Kr, one to several kg of ice are needed per sample. This is a problem, especially for valuable ice cores with limited ice amounts where an ATTA dating measurement has to compete with other analyses for the ice. By designing and testing a gas extraction unit that can be coupled to the routinely applied continuous flow analysis system (CFA) for ice cores, the unused gas from its waste line can be extracted and trapped for a later ATTA analysis. Several tests have been conducted and, eventually, a successful gas extraction campaign from an Antarctic ice core was performed, indicating a reliable system with a very low risk of contamination.
Finally, in chapter 10, two projects that were conducted in collaboration with external partners are briefly summarized. Both show the value of ^{39}Ar in complementing the dating range of ^{14}C: one being an ice core from the Dôme du Goûter which provides a continuous record of aerosols, dust, and sea salt deposition back to the Younger Dryas; the other project is a "horizontal ice core" from a glacier on Svalbard, sampled from the glacier surface along its descent that can help to extend the ice core records of this remote region.

While the initial motivation for this PhD-project was based on the application of the ^{39}Ar dating method to different glacial settings, it very soon became apparent that the most urgent need for this and many other projects of the ATTA collaboration was the actual lab work in the ATTA laboratory at the KIP. Improving its performance as well as ensuring stable and long-term measurement operation therefore quickly became the actual main content of the daily work. The main focus of the PhD-project therefore shifted towards atom-optical topics for the first large part of this thesis. With high numbers of students motivated to write their theses in environmental physics in recent years, the application of the method to glaciers and other environmental systems as well as the interpretation was therefore conducted in slices of smaller bachelor and master projects in close cooperation and with the supervision of the author. In the later part of the thesis, the focus shifted to the final interpretation of the accumulated environmental data, often refining and combining the smaller projects into a bigger picture. Therefore, in most chapters, the bachelor and master theses, which were closely supervised by the author and which laid the basis for this final evaluation, are referenced.
Because of the large bandwidth of technical developments in the ATTA laboratory and applications to environmental systems that were conducted within the ATTA collaboration in Heidelberg in recent years, the evaluation in this thesis had to be restricted to the overarching topic of glacier ice dating. However, as large amounts of the author's time were also invested in the preparation of the laboratory for the

execution of other measurements, the total of 216 environmental samples that were measured during the author's supervision of the ATTA laboratory are listed in the appendix A.5. With this achievement of a large and continuous sample throughput over several years, the ATTA technology has taken the next step, away from a mainly experimental toward a routinely applicable analysis.

2 Fundamentals of ^{39}Ar-ATTA

This chapter introduces the fundamental concepts needed to understand the methods employed in this thesis as well as the environmental systems that are analyzed. First, the main tracer of interest, ^{39}Ar is discussed with its properties and role in dating environmental archives. Subsequently, the basic concepts required for ATTA are introduced.
The second part introduces glaciers as the environmental system in the focus of this thesis, covering their structure and dynamics as well as climatic history.

2.1 Argon and the ^{39}Ar Isotope - Dating with a Noble Gas Radionuclide

Argon is the third most abundant gas in the atmosphere, constituting 0.934 % by volume. However, being a noble gas with no inclination for chemical reactions and being color- and odorless, it was only discovered in 1894 by Lord Rayleigh and Sir William Ramsay, for which the former earned the Nobel Prize in 1904 (Rayleigh and Ramsay, 1895). While 24 known isotopes of Ar exist, only a few are encountered naturally, namely ^{36}Ar, ^{38}Ar, ^{39}Ar, ^{40}Ar and ^{42}Ar. Table 2.1 gives an overview of these isotopes and some of their physical properties. ^{40}Ar is the prevailing isotope, making up 99.6 % of the total Ar. It originates from the decay of ^{40}K which naturally occurs in the earth's crust and mantle. In contrast, primordial Ar e.g. in the sun exclusively consists of ^{36}Ar and ^{38}Ar.
The ^{39}Ar isotope was first discovered by Brosi et al. (1950) in irradiated potassium salts. The atmospheric ^{39}Ar, however, is mainly produced by the spallation

$$^{40}\mathrm{Ar(n,2n)}^{39}\mathrm{Ar}, \tag{2.1}$$

which takes place in the stratosphere through cosmogenic neutrons with energies above the threshold of 10.1 MeV. Work by Gu et al. (2021) and Happel (2024) shows that variations in the cosmic ray flux have changed the ^{39}Ar concentration by maximally 20 % in the past millennia. This is an effect that has to be corrected for when dating with this tracer. Besides the production of ^{39}Ar in the atmosphere there is also production in the ground. Even though this does not have a strong effect on the atmospheric concentration, it can play a role when investigating archives in the subsurface. Work by e.g. Musy and Purtschert (2023) has shown that production via neutron activation of ^{39}K

$$^{39}\mathrm{K(n,p)}^{39}\mathrm{Ar} \tag{2.2}$$

Table 2.1: Characteristic parameters of the main Ar isotopes. Note that the concentration of ^{40}Ar is marginally increasing over time (Bender et al., 2008) and the natural concentration of ^{39}Ar is changing over time due to its cosmogenic production (Gu et al., 2021; Happel, 2024). The last column gives the relative frequency shift in MHz of the cooling transition for the different isotopes to ^{40}Ar. Data taken from IAEA (a), Golovko (2023), Rausch, D'Amico et al. (1999), Collon et al. (2004a), and Welte (2011). ^{37}Ar is listed as it can be used to quantify underground production of Ar (compare Musy et al., 2022).

Isotope	Nat. Abundance [mole fraction]	Nucl. Spin I	$T_{1/2}$	$\Delta\nu_{^{40}\mathrm{Ar}}$ [MHz]
^{36}Ar	0.3336(4) %	0	stable	-450.1
^{37}Ar	-	3/2	35.0 d	-
^{38}Ar	0.0629(1) %	0	stable	-208.1
^{39}Ar	$8.1(3) \times 10^{-16}$	7/2	268(3) a	492.2
^{40}Ar	99.6035(4) %	0	stable	0.0
^{42}Ar	$< 6 \times 10^{-21}$	0	32.9 a	-

is dominant in the first few meters below the surface, before cosmogenic neutrons are stopped by the matrix. This effect does not play a significant role in the dating of e.g. groundwater, however, it can be employed for the new idea of surface exposure dating with ^{39}Ar (compare section 8.4). Further into the subsurface, the production via muon capture reactions such as

$$^{39}\mathrm{K}(\mu^-, \mathrm{p})^{39}\mathrm{Ar} \quad \text{and} \tag{2.3}$$

$$^{40}\mathrm{Ca}(\mu^-, \mathrm{p})^{39}\mathrm{Ar} \tag{2.4}$$

is affecting layers down to several tens of meters of depth, possibly altering the ^{39}Ar concentration in groundwater. Even deeper, the neutron activation becomes dominant again due to neutrons from primordial uranium and thorium. This process is highly dependent on the matrix material and the abundance of the mentioned elements.
For the dating of glacial ice presented here, all these non-atmospheric production processes do not play a significant role, as the target materials such as ^{39}K and ^{40}Ca are not present in significant quantities.

2.1.1 Basics of Radiometric Dating

The interest for ^{39}Ar is sparked by its radioactive properties, mainly its half-life of 268±3 a (Golovko, 2023), which make it unique among other feasible tracers for environmental archives. It decays via β^- decay to ^{39}K.
Figure 2.1 shows the dating ranges of different tracers. In this graph, all tracers except SF_6 and CFCs are based on their radioactive decay properties, the fundamental principles of which will be discussed in the following.

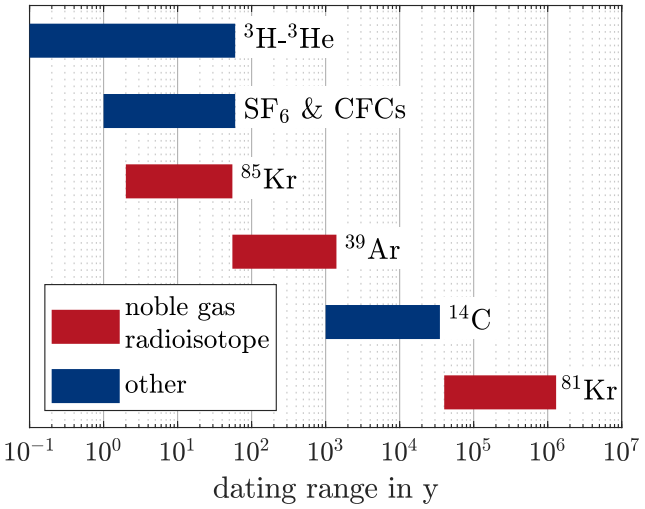

Figure 2.1: Visualization of dating tracers and their applicable dating ranges in years. Note that ^{39}Ar fills the gap between the modern tracers and ^{14}C, which for hydrological systems and glaciers lacks precision below 1000 a. Figure taken from Robertz (2023).

The law of radioactive decay describes the depletion of the number of radioactive atoms N over time t by

$$N(t) = N_0 \cdot \mathrm{e}^{-\lambda t} = N_0 \cdot \mathrm{e}^{-\frac{\ln(2)}{T_{1/2}} t} \tag{2.5}$$

where N_0 is the initial number of radioactive atoms, λ the specific decay constant and $T_{1/2}$ the specific half-life of the species of interest. This can be rewritten to give the decay time in dependence on an initial and current concentration:

$$t = \frac{T_{1/2}}{\ln(2)} \cdot \ln\left(\frac{N_0}{N(t)}\right). \tag{2.6}$$

With this law at hand and a known initial concentration, a measured current concentration can be translated to a time at which e.g. a sample must have been cut off from atmospheric re-equilibration. In the case of glacial ice, this means that the time an air bubble has been closed off from the atmosphere and continuously losing ^{39}Ar due to its decay, i.e. the age of the glacier ice, can be obtained from determining the current ^{39}Ar concentration relative to its initial concentration.

2.2 Argon Isotopes and their Level Structure

In the following, the atomic spectrum of Ar will be discussed, laying the base for the atom-optical methods presented subsequently. In parts, the introduction leans on Ringena (2021) and Robertz (2023).

Ar is a noble gas with 18 electrons and therefore has filled electronic shells with an electron configuration of

$$1s^2 2s^2 2p^6 3s^2 3p^6 = [Ne]3s^2 3p^6. \tag{2.7}$$

Each tuple nl^e denotes an electronic state which is defined by its principle quantum number n and the orbital angular momentum l with values of $l = 0, 1, ..., n-1$. Furthermore, each of these momenta has magnetic sublevels with quantum numbers $m_l = -l, -l+1, ..., l-1, l$. The superscript indicates the number of electrons in this specific level.
The first excited state is reached when an electron is transferred to the energetically next shell, in this case, the 4s shell. Because this happens by exciting an electron from a filled shell the required energy is very high with approximately 11.6 eV. As this translates to wavelengths around 107 nm, light in the vacuum ultraviolet (VUV) regime is required for the excitation from the ground state. Such lasers are not commercially available and therefore the transition for laser cooling does not excite from the ground state but a meta-stable state (lifetime of ≈38 s, Katori and Shimizu, 1993) from which smaller energies and thus commercially available lasers can be employed. The excitation to the meta-stable state is achieved via electron impact excitation in a plasma, a concept which is introduced in section 2.6
The configuration of the states of the cooling transition is given by

$$[Ne]3s^2 3p^5 4s^1 \rightarrow [Ne]3s^2 3p^5 4p^1, \tag{2.8}$$

where the first state is the meta-stable state.
Having introduced the electron configuration is the first step towards the energy level structure. The next important parameter for the level structure is the coupling of the electrons. As discussed, the excited electron occupies a shell of higher n than the others and because the orbital radius scales with n^2 it is significantly further away from the inner ones. With this in mind, the inner part of the electron shells can be described as a 'body' where the electrons couple with each other. This results in a LS-coupling of the total body spin $\vec{S} = \sum_i \vec{s}_i$ and the total body orbit angular momentum $\vec{L} = \sum_i \vec{l}_i$ to the total body angular momentum $\vec{j}_{\text{body}} = \vec{S} + \vec{L}$. The excited electron now couples to this body, first with its orbital angular momentum $\vec{l}$ to $\vec{j}_{\text{body}}$, resulting in $\vec{K}$ with $K = |j_{\text{body}} - l|, |j_{\text{body}} - l| + 1, ..., |j_{\text{body}} + l|$ and finally with its electron spin $\vec{s}$ to $\vec{K}$, resulting in the total angular momentum of all electrons $\vec{J}$ with $J = |K - s|, |K - s| + 1, ..., |K + s|$. The coupled quantum numbers of the body do not change from the meta-stable to an excited state and are therefore valid for both states of 2.8 with $S = 1/2$ and $L = 1$. Thus also the total angular momentum of the body is the same for both states with $\vec{j}_{\text{body}} = 3/2$ (Zappala, 2017; Feng, 2019). Other energy states can also have $\vec{j}_{\text{body}} = 1/2$.
As seen from the numbers in 2.8, the quantum numbers of the excited state electron are $l_e = 1$ and $s_e = 1/2$ and of the meta-stable state electron $l_g = 0$ and $s_g = 1/2$. The resulting coupling possibilites for K are therefore $K_g = (1/2), 3/2$ and $K_e = (1/2, 3/2), 5/2$, with the non-considered numbers in brackets. The energy levels

addressed with the current ATTA method are $K_g = 3/2$ for the ground state and $K_e = 5/2$ for the excited state, resulting in $J_g = 2$ and $J_e = 3$ (again only the relevant ones for ATTA). A convenient notation for these energy states is the Racah-notation

$$nl[K]_J. \tag{2.9}$$

In this notation, the cooling transition appears as

$$4\mathrm{s}[3/2]_2 \rightarrow 4\mathrm{p}[5/2]_3. \tag{2.10}$$

For the stable isotopes of Ar, this is the full description of the quantum numbers. However, for ^{39}Ar a non-zero nuclear spin $I = 7/2$ results in the hyperfine splitting of the energy states. The quantum number J as the total angular momentum has to be replaced by the quantum number F which is given by $F = |I-J|, |I-J|+1, ..., |I+J|$. The right side of figure 2.2 shows the hyperfine splitting of ^{39}Ar. The meta-stable state splits into five substates with $F_g = 11/2, 9/2, ..., 3/2$, the excited state in seven states $F_e = 13/2, 11/2, ..., 1/2$. The cooling transition is then chosen as

$$4\mathrm{s}[3/2]_2(F = 11/2) \rightarrow 4\mathrm{p}[5/2]_3(F = 13/2), \tag{2.11}$$

because due to the selection rules of $\Delta F = -1, 0, 1$ the excited state can only decay back into the ground state. The spontaneous decay rate of the chosen cooling transition, a relevant property for the number of scattering events per time interval and thus the exerted force, is (Metcalf and van der Straten, 2012)

$$\gamma = 2\pi \cdot 5.87\,\mathrm{MHz}. \tag{2.12}$$

Altogether, as indicated in table 2.1, the cooling transition for ^{39}Ar is 492.2 MHz apart from the cooling transition of ^{40}Ar, which lays the foundation for the ATTA method.
Also, the meta-stable state draws its long-lived property from the selection rules. Because they request $\Delta J = -1, 0, 1$, the transition to the ground state is not possible via dipole transitions and is, thus, highly suppressed.
In addition to the cooling transitions, a few other transitions have to be addressed in the ATTA experiment. Because the energy splitting of the hyperfine structure is very small, off-resonant excitation to other energy levels becomes possible. To not 'lose' atoms to a wrong energy state, the atoms from other hyperfine states have to be repumped to the original meta-stable state, requiring additional laser frequencies referred to as repumpers (compare figure 2.2). Furthermore, to selectively de-excite (quench) ^{40}Ar atoms to the ground state a quench laser is employed. As indicated in figure 2.2, the laser excites ^{40}Ar atoms to the $4\mathrm{p}[5/2]_2$ level, from where they can decay down to the ground state and therefore do not cause a noise signal in the apparatus due to off-resonant scattering of the ^{39}Ar cooling lasers.

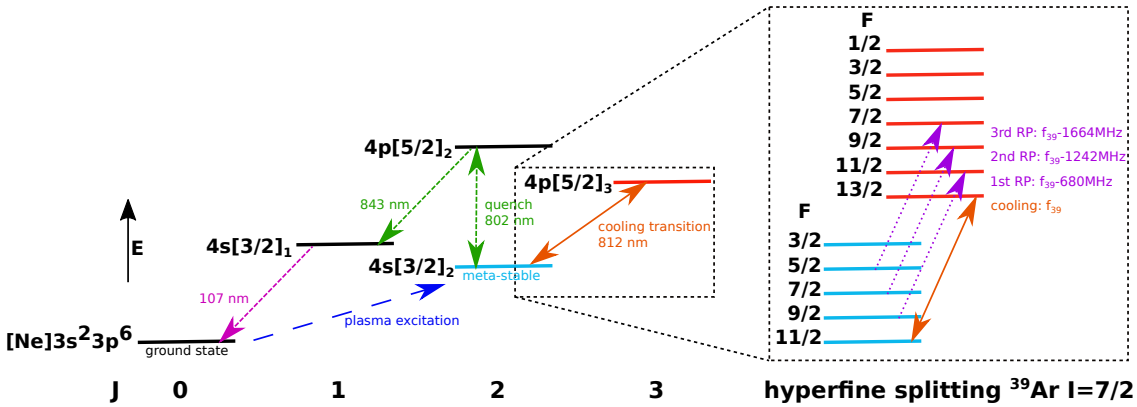

Figure 2.2: Part of the energy spectrum of Ar relevant to ATTA, energy not to scale. The $nl[K]_J$ notation is used. As 107 nm lasers are not available, rf-generated plasma is used to populate the meta-stable state. On the right, the hyperfine splitting of ^{39}Ar due to its nuclear spin of I = 7/2 is shown. The orange arrow indicates the cooling transition from the meta-stable state, purple arrows indicate the repumper transitions for ^{39}Ar (the possible fourth repumper is omitted in the experiment, as it contributes only very weakly). Green arrows indicate the quench transition from the meta-stable state and its decay down toward the ground state and the pink arrow the VUV transition down to the ground state.

2.3 Interaction of Atoms with Light

The ATTA method for trapping and counting ^{39}Ar atoms is based on the principles of laser cooling, which essentially means that force on atoms is exerted from precisely tuned lasers. In the following section, the mathematical basics of the interaction of light and atoms will be given, based on the chapter in Ringena (2021).

Density Matrix Model

To describe the system of an atom and laser light the density matrix model can be employed. The approach will result in the optical Bloch equations and the scattering rate of the photons. The following section closely follows Metcalf and van der Straten (1999), which also gives a more detailed discussion.
In quantum mechanics the normalized wavefunction $|\Psi\rangle$ describes the full system of a pure state. For a Hilbert space of n dimensions, this wavefunction can be expanded in the basis Φ_n with coefficients c_i:

$$\Psi = \sum_{i=1}^{n} c_i \Phi_i. \tag{2.13}$$

Alternatively, one can use the density operator ρ to describe the system. It is defined as

$$\rho = |\Psi\rangle \langle\Psi| . \tag{2.14}$$

From these two equations follows the n×n density matrix, where the n wavefunctions scan the Hilbert space entirely:

$$\rho_{ij} = \langle \Phi_i | \rho | \Phi_j \rangle = \langle \Phi_i | \Psi \rangle \langle \Psi | \Phi_j \rangle = c_i c_j^*. \tag{2.15}$$

However, the description by a pure state does not work anymore when spontaneous emission is introduced into the system. Here, the system becomes a statistical mixture of several states Ψ_n each with probability p_i. The density operator is then written as

$$\rho = \sum_i p_i |\Psi_i\rangle \langle \Psi_i| . \tag{2.16}$$

For a two-level system with excited state $|e\rangle$ and ground state $|g\rangle$, the density matrix from equation 2.15 results in

$$\rho = \begin{pmatrix} \rho_{ee} & \rho_{eg} \\ \rho_{ge} & \rho_{gg} \end{pmatrix} = \begin{pmatrix} c_e c_e^* & c_e c_g^* \\ c_g c_e^* & c_g c_g^* \end{pmatrix} \tag{2.17}$$

for the state given by $|\Psi\rangle = c_e |e\rangle + c_g |c_g\rangle$.
The energy difference between ground and excited state is given by $\Delta E = \hbar\omega_a$. The angular frequency of a laser driving the transition is given by ω_L and the detuning of the laser light $\delta = \omega_\mathrm{L} - \omega_a$ is assumed to be small compared to the resonance frequency: $|\delta| \ll \omega_a$. By assuming a weak coupling ($|\Omega| \ll \omega_\mathrm{L}$) the rotating wave approximation (RWA) can be applied which neglects terms of the Hamiltonian oscillating with frequency $\omega_\mathrm{L} + \omega_a$.
An important parameter for the time evolution of the density matrix elements is the transition's Rabi frequency Ω, which is defined as

$$\Omega = -\frac{eE_0}{\hbar} \langle e | r | g \rangle = \frac{E_0}{\hbar} \mu_{eg} \tag{2.18}$$

with the electron coordinate operator r, the laser light field amplitude E_0, the elementary charge e, and $\hbar$ the reduced Planck constant, and the transition dipole matrix element μ_{eg}. With this number, the evolution equation for the terms ρ_{ij} can be found in expressions similar to

$$\frac{\mathrm{d}\rho_{gg}}{dt} = \frac{\mathrm{d}c_g}{dt} c_g^* + c_g \frac{\mathrm{d}c_g^*}{dt} = i\frac{\Omega^*}{2} c_e \mathrm{e}^{i\delta t} c_g^* - c_g i \frac{\Omega}{2} c_e^* \mathrm{e}^{i\delta t} \equiv i\frac{\Omega *}{2} \tilde{\rho}_{eg} - i\frac{\Omega}{2} \tilde{\rho}_{ge}, \tag{2.19}$$

where $\tilde{\rho_{ge}} \equiv \rho_{ge} \mathrm{e}^{-i\delta t}$ (Metcalf and van der Straten, 1999). Similarly, the time derivatives of the other density matrix elements can be found.
In this system, spontaneous emission can now be described by an exponential decay of the coefficient $\rho_{eg}(t)$ with a constant rate $\gamma/2$:

$$\left(\frac{\mathrm{d}\rho_{eg}}{\mathrm{d}t}\right)_{\text{spont.}} = -\frac{\gamma}{2}\rho_{eg}. \tag{2.20}$$

Combining all this yields the optical Bloch equations (OBEs):

$$\begin{aligned}
\frac{\mathrm{d}\rho_{gg}}{\mathrm{d}t} &= \gamma\rho_{ee} + \frac{i}{2}(\Omega^*\tilde{\rho}_{eg} - \Omega\tilde{\rho}_{ge}) \\
\frac{\mathrm{d}\rho_{ee}}{\mathrm{d}t} &= -\gamma\rho_{ee} + \frac{i}{2}(\Omega\tilde{\rho}_{ge} - \Omega^*\tilde{\rho}_{eg}) \\
\frac{\mathrm{d}\tilde{\rho}_{ge}}{\mathrm{d}t} &= -\left(\frac{\gamma}{2} + i\delta\right)\tilde{\rho}_{ge} + \frac{i}{2}\Omega^*(\rho_{ee} - \rho_{gg}) \\
\frac{\mathrm{d}\tilde{\rho}_{eg}}{\mathrm{d}t} &= -\left(\frac{\gamma}{2} - i\delta\right)\tilde{\rho}_{eg} + \frac{i}{2}\Omega(\rho_{gg} - \rho_{ee}).
\end{aligned} \tag{2.21}$$

These equations can then be solved for the steady state in which the population difference u between excited and ground state is constant, meaning $u \equiv \rho_{gg} - \rho_{ee}$ =constant. Solving the OBEs yields:

$$\frac{\mathrm{d}u}{\mathrm{d}t} = \frac{\mathrm{d}(\rho_{gg} - \rho_{ee})}{\mathrm{d}t} = -\gamma u - i\left(\Omega^*\rho^*_{eg} - \Omega\rho_{ge}\right) + \gamma = 0, \tag{2.22}$$

leading to the solutions

$$u = \frac{1}{1+s} \tag{2.23}$$

$$s \equiv \frac{|\Omega|^2}{\delta^2 + \gamma^2/4} \equiv \frac{s_0}{1 + (2\delta/\gamma)^2} \tag{2.24}$$

$$s_0 \equiv \frac{2|\Omega|^2}{\gamma^2} \equiv \frac{I}{I_s} \text{ with the latter being} \tag{2.25}$$

$$I_s = \frac{\pi h c \gamma}{3\lambda^3} \text{ for } \sigma^{\pm} \text{ polarized light.} \tag{2.26}$$

s is the saturation parameter and s_0 the on-resonance saturation parameter. For a low saturation parameter, $s \ll 1$, the population is mostly in the groundstate whereas for high s the population is equally distributed between ground and excited state ($u = 0$).
The scattering rate γ_s of photons is then given by the spontaneous decay rate γ and the excited state's population ρ_{ee}:

$$\gamma_s = \gamma\rho_{ee} = \frac{s_0\gamma/2}{1 + s_0 + (2\delta/\gamma)^2} \tag{2.27}$$

where δ is the laser detuning and γ the decay rate of the excited state (5.87 MHz, Metcalf and van der Straten, 1999). The result gives a measure of the interaction between the light field and atom with the tunable laser parameters s_0 and δ. It can be seen that with increasing laser power and thus increasing s_0, γ_s saturates at $\gamma_s = \gamma/2$, the maximum possible scattering rate. In the following, the resulting control of the atom and light forces are discussed.

2.3.1 Light Induced Forces

The force a light field exerts on an atom is governed by the above derived scattering rate which gives the time of an absorption and emission cycle of a photon by an atom and the momentum transfer from photon to atom.
The momentum each photon carries is given by $\vec{p} = \hbar\vec{k}$. This momentum is transferred to an atom upon absorption and excites the atom to a higher energy state where the atom stays until it de-excites with the emission of a photon. In the case of spontaneous emission, the direction of the emission is randomly spatially distributed, resulting in a net zero momentum gain of the atom averaged over many emission cycles. In contrast, the absorption of photons of a single laser coming from a specific propagation direction defined by $\vec{k}$ results in a net force $\vec{F}$ from that direction:

$$\vec{F} = \hbar\vec{k}\gamma_s, \tag{2.28}$$

where the scattering rate derived in equation 2.27 gives the absorption-emission cycles per time. Combining the two equations results in

$$\vec{F} = \hbar\vec{k}\gamma\frac{s_0/2}{1 + s_0 + (2\delta/\gamma)^2}. \tag{2.29}$$

It can be seen that the force can be increased with increasing laser power, however saturating at

$$\vec{F}_{\max} = \hbar\vec{k}\gamma/2. \tag{2.30}$$

A very important parameter is the detuning δ of the laser light to the atom's internal energy transition. While this can be manually tuned with a laser, it also experiences shifts due to other effects, of which the Doppler effect and the Zeeman effect will be discussed in the following.

2.3.2 Doppler Effect

The Doppler shift is caused by different frames of reference between atom and photon. It causes a frequency shift of the laser light experienced by the atom depending on the relative velocity of the two. In the atom's frame of reference, the frequency appears shifted by

$$\delta_D = -\vec{k} \cdot \vec{v}, \tag{2.31}$$

with the wavevector $\vec{k}$ of the photon and the atom velocity $\vec{v}$.
The effect is very important for the ATTA method, as the velocities of the atoms in the apparatus range from several hundred m/s down to almost zero velocities and because the laser light is directed at the atoms from many different angles. With the scalar product in equation 2.31, the resulting frequency shift is also dependent on the relative angles. All in all, to tune the lasers to the right frequencies in the right components of the apparatus, the Doppler shift always has to be taken into account and serves as the main tool for selectively addressing atoms of a certain velocity class.

A very good example of the relevance of the Doppler effect is the Zeeman slower, where atoms are cooled down from several hundred m/s velocities to several tens of m/s. As discussed in more detail in section 4.3, the cooling laser here is directed anti-parallel to the atom beam. Therefore, with the deceleration of the atoms, the Doppler shift changes and the atoms go out of resonance and are not further decelerated. To keep the atoms in resonance the subsequently introduced Zeeman effect is employed.

2.4 Interaction of Atoms with Magnetic Fields

In order to manipulate atoms in a lab environment, access to their internal structure is a major step towards more control. By adding magnetic fields to the toolbox, a new type of control is gained over the atom's inner energy levels. To understand the basics of the interactions of atoms with magnetic fields the Zeeman effect will briefly be discussed in the following, more detailed discussion can be found e.g. in Haken and Wolf (2004).

2.4.1 Zeeman Shift

When an atom experiences an external magnetic field $\vec{B}_0$ it experiences a shift in its potential energy depending on the atom's magnetic moment μ. The energy shift due to this Zeeman effect is given by

$$\Delta E_{\text{pot}} = -\vec{\mu} \cdot \vec{B}_0. \tag{2.32}$$

Hereby, the magnetic moment is made up of the total angular momentum of the atom given by $\vec{L}, \vec{J}, \vec{S}$ or $\vec{F}$. In the following, the magnetic moment of the hyperfine structure, $\vec{\mu}_F$, is chosen as a substitute for any magnetic moment $\vec{\mu}_{L,J,S,F}$:

$$\vec{\mu}_F = -\mu_B g_F \vec{F}/\hbar \tag{2.33}$$

with the Landé-factor g_F and the Bohr magneton μ_B.
The Zeeman effect causes the previously degenerate sublevels to shift their energies depending on their magnetic quantum number. For an atom with hyperfine splitting these sublevels are given by $m_F = -F, -F+1, ..., F$.
Considering an external magnetic field in z-direction: $\vec{B}_0 = \vec{e}_z B_z$, the vector of μ_F only has discrete projections on the z-axis, denoted by the quantum number m_F. With this relation, the z-component of the magnetic moment can be written as

$$(\vec{\mu}_F)_z = -\left(\mu_B g_F \vec{F}/\hbar\right)_z = -\mu_B g_F m_F, \tag{2.34}$$

so that the energy difference amounts to

$$\Delta E(F, m_F) = \mu_B g_F m_F B_z. \tag{2.35}$$

The Landé g-factor is given by (Fox, 2006)

$$g_J = 1 + \frac{J(J+1) + S(S+1) - L(L+1)}{2J(J+1)}, \quad \text{respectively} \tag{2.36}$$

$$g_F \approx g_J \frac{F(F+1) + J(J+1) - I(I+1)}{F(F+1)}. \tag{2.37}$$

Thus, the magnetic sublevels split energetically and their separation increases linearly with the magnetic field. Robertz (2023) and Ritterbusch (2013) list the most important Landé factors for the energy levels relevant in ATTA.
Note that these relations only apply to small magnetic fields. At higher field strengths the Paschen-Back effect has to be considered.

With equation 2.35, the detuning δ_Z of a transition from $|Jm_J\rangle$ to $|J'm_{J'}\rangle$ is given by the difference between the two energy shifts ΔE_Z:

$$\delta_Z = (m_J g_J - m_{J'} g_{J'}) \frac{\mu_B B}{\hbar}. \tag{2.38}$$

As a result of the different Landé g-factors for ^{39}Ar due to its hyperfine splitting, the forces in the atom traps are reduced. This is discussed in more detail in the theses of Robertz (2023) and Ritterbusch (2013).

2.5 Cooling and Trapping of Atoms

So far the basic concepts of light interaction with atoms were discussed, which was restricted to one laser from one direction interacting with the atoms. This concept will now be expanded to multiple beams, as their interplay makes up many of the magneto-optical elements of the ATTA apparatus. If laser powers are low enough to neglect stimulated emission, then the forces of the laser beams can simply be added to obtain their joined effect.

2.5.1 Optical Molasses

Considering an atom in one dimension with velocity $\vec{v}$ and two counterpropagating laser beams with wavevectors $\vec{k}$ and $-\vec{k}$, the resulting force can then be written as in the following way with equations 2.29 and 2.31:

$$\vec{F} = \vec{F}_+ + \vec{F}_- = \frac{\gamma \hbar \vec{k} s_0}{2} \left[\frac{1}{1 + s_0 + (2(\delta - \vec{k} \cdot \vec{v})/\gamma)^2} - \frac{1}{1 + s_0 + (2(\delta + \vec{k} \cdot \vec{v})/\gamma)^2} \right], \tag{2.39}$$

taking into account the Doppler shift but no magnetic field. For an atom at rest, the detuning is experienced equal for both lasers by the atom and therefore the net force

adds up to zero.
For low velocities and small detunings, this expression can be approximated with

$$\vec{F} \approx \frac{8\hbar k^2 \delta s_0 \vec{v}}{\gamma(1 + s_0 + (2\delta/\gamma)^2)^2} \equiv -\beta\vec{v}. \tag{2.40}$$

It becomes apparent that a dampening force on the atoms with $\vec{v} \neq 0$ can be realized when choosing $\delta < 0$, as can be seen in figure 2.3. This effect comes from the interplay of the light force with the relative velocity of the atoms to the laser light. Due to the Doppler effect, for a $\delta < 0$, atoms moving towards a laser beam are more on resonance and therefore experience a stronger force and are slowed down, resulting in a general cooling of the atoms in the direction of the laser beams. For a $\delta > 0$ this effect would be reversed and therefore atoms would be heated and accelerated away. This simple setup for atom cooling is called an optical molasses, as it viscously dampens an atom. However, due to the missing spatial dependence of the cooling force, it is not yet fit for trapping atoms. This is the main difference to the magneto-optical trap (MOT), which will be discussed in the following.

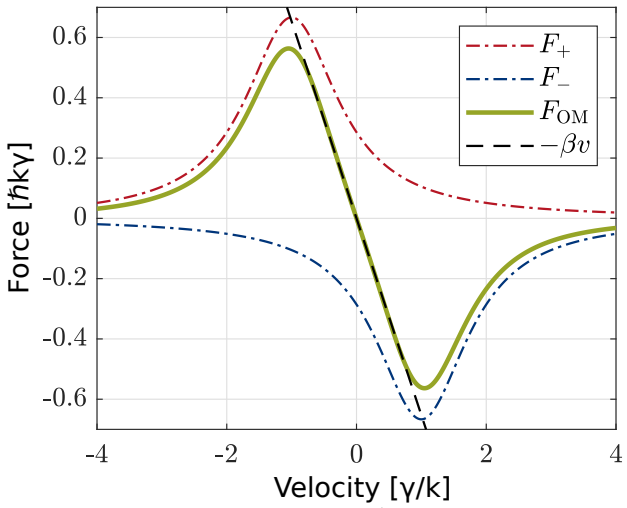

Figure 2.3: The velocity-dependent dampening force for a one-dimensional optical molasses. $F_\pm$ are the forces for each single laser beam, while F_{OM} is the resulting net force. β (compare equation 2.40) can be interpreted as the dampening coefficient of the optical molasses. The saturation parameter is set to $s_0 = 2$ and the laser detuning to $\delta_L = -\gamma$. Figure similar to Metcalf and van der Straten (1999), taken from Robertz (2023).

2.5.2 Magneto-Optical Trap

When adding an inhomogeneous magnetic field to the setup of the optical molasses, the Zeeman effect changes the properties of this setup in such a way that atoms can be trapped at its center. An inhomogeneous magnetic field achieved by coils in an

anti-Helmholtz configuration, introduces a position-dependent shift of the energy levels due to the Zeeman effect, increasing the further away from the trap center an atom is positioned. With this property, a confinement not only in velocity but also in position space is achieved. Since its first publication by Raab et al. (1987) it has proven a very versatile and robust atom trap. Here, an overview of its working principle is given. More detailed elaborations can be found in Chu (1998) and Metcalf and van der Straten (1999).
The inhomogeneous magnetic field is implemented as a quadrupole field $\vec{B}(\vec{r})$, which in one dimension, close to the center, can be approximated by $B(z) = \mathcal{B}z$. In the following $\mathcal{B} > 0$ is assumed. Furthermore, the transition $J = 0$ to $J = 1$ is considered, for which the magnetic sublevels m_J of the excited state, therefore, have a position-dependent energy, compare figure 2.4.
For the one-dimensional case now consider two laser beams traveling in $\pm z$ direction, with polarizations $\sigma^{\pm}$. With these polarizations, the σ^+ beam couples with the $m_J = 0 \to 1$ transition, and the σ^- beam with the $m_J = 0 \to -1$ transition.
The effective detuning experienced by an atom with velocity $\vec{v} = v\vec{e}_z$ is given by

$$\delta_{\pm} = \underbrace{\delta_L}_{\text{laser detuning}} \mp \underbrace{\vec{k}\cdot\vec{v}}_{\text{Doppler shift}} \pm \underbrace{(g_e m_e - g_g m_g)\frac{\mu_B B}{\hbar}}_{\text{Zeeman effect}}. \tag{2.41}$$

Again, the resulting net force is the sum of the two single forces: $\vec{F} = \vec{F}_+ + \vec{F}_-$. The expression can be expanded for small Doppler and Zeeman detunings compared to the laser detuning, resulting in

$$\vec{F} = -\beta\vec{v} - \kappa\vec{r}, \quad \text{with } \kappa = \underbrace{(g_e m_e - m_g m_g)\mu_B}_{=\mu'}\frac{\mathcal{B}}{\hbar k}\beta. \tag{2.42}$$

This equation can be interpreted as the harmonic oscillator with κ being the spring constant and β the dampening coefficient with the definition from 2.40 (Metcalf and van der Straten, 1999).

2.5.3 Isotopic Separation of ^{39}Ar

Having discussed all the relevant properties of Ar and also the atom-optical tools that are available, it can now be brought together to discuss its necessity for the detection of the ^{39}Ar isotope. In a simple approach, having discussed the different energy level structures of the different isotopes, resulting in a shift in the resonance frequency of Δ =492.2 MHz in the preceding sections, one could propose to use simple spectroscopy for the detection of ^{39}Ar. This, however, disregards the influence of non-resonant excitation. Taking a simple model assuming Lorentzian lineshapes, as proposed by Collon et al. (2004b), the selectivity S of a single excitation can be expressed as

$$S = 4 \times \left(\frac{\Delta}{\Gamma}\right)^2 \quad \text{when } \Delta \ll \Gamma, \tag{2.43}$$

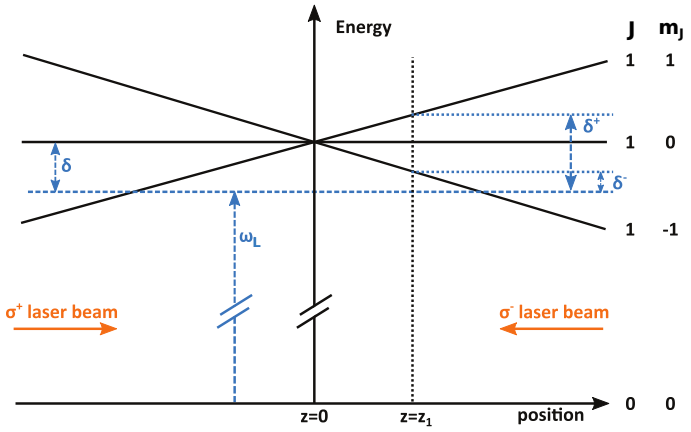

Figure 2.4: Schematic of one dimension of a MOT with the spatial dimension on the x-axis and the energy on the y-axis. The transition from the ground state $|g\rangle = |J = 0, m_J = 0\rangle$ to the excited state $|e\rangle = |J = 1, m_J = 0, \pm 1\rangle$ is driven by laser light with frequency ω_L detuned to the atomic resonance by δ. A linearly inhomogeneous magnetic field causes a splitting of the three excited substates indicated by the black diagonal lines. The center of the trap is defined as the point of zero magnetic field. The magnetic field causes the energy level $|J = 1, m_J = -1\rangle$ to shift to lower energies when moving in the positive z-direction. At location $z = z_1$, the state $|e\rangle = |J = 1, m_J = -1\rangle$ then lies closer to resonance with the laser light and therefore scatters more photons than the other state. Since the transition to this state from $|g\rangle = |J = 0, m_J = 0\rangle$ requires a σ^--photon (in the frame of reference of the atom), the atom selectively scatters the light of the counter-propagating laser beam, resulting in a force towards the trap center. The figure is inspired by Metcalf and van der Straten (1999) and adapted from Ringena (2021).

where Δ is the frequency difference between the isotopes and Γ the interaction linewidth. In the here relevant case, $\Gamma = 2\pi \cdot 5.87\,\mathrm{MHz}$ (Metcalf and van der Straten, 2012) and therefore $S = 712$. Which means that for equal amounts of ^{39}Ar and ^{40}Ar in a sample, every 712 resonant excitations of ^{39}Ar, one off-resonant excitation of ^{40}Ar occurs. With the natural abundance of $R_A = 8.1 \times 10^{-16}$, the probability of a ^{39}Ar resonant photon to scatter an ^{39}Ar atom rather than a ^{40}Ar atom is given by

$$\frac{P_{39}}{P_{40}} = S \cdot R_A = 6 \cdot 10^{-13}. \tag{2.44}$$

This means that a spectroscopy signal would be by far dominated by the off-resonant scattering of ^{40}Ar and thus could not provide a detectable ^{39}Ar signal. The solution for the detection of ^{39}Ar using photon excitation lies in the probability for N consecutive photons to scatter ^{39}Ar over ^{40}Ar:

$$\left.\frac{P_{39}}{P_{40}}\right|_N = S^N \cdot R_A. \tag{2.45}$$

It is apparent that it is only a matter of a high enough N to reach selectivity. In the case of ^{39}Ar, for $N > 6$ photons the selectivity becomes greater than 1 (actually

$P_{39}/P_{40}|_{N=6} = 105$) and grows exponentially with N. Therefore, it is only a matter of designing an apparatus that only receives a signal of ^{39}Ar if it has undergone at least 6 photon scattering events. With laser cooling techniques like the magneto-optical trap, where scattering rates in the order of 10^7 photons/s are to be expected, the detection of an atom at rest at the center of the MOT for a minimum detection time of 40 ms, as is the case in the current apparatus, fulfills these criteria by far. In this way, the ATTA method reaches selectivities far beyond what is needed for the ^{39}Ar detection and is only limited by the total detected atoms.

2.6 Electron Impact Excitations in Inductively Coupled Plasmas

As discussed in section 2.2, the excitation from the ground state to the first excited state cannot be driven by conventional lasers. Therefore, the so far established method is the excitation in a plasma. For the understanding of this process, a brief overview is given in the following

Plasma is one of the four fundamental states of matter and consists of free charged particles. In the here-discussed case, it is a weakly ionized plasma inductively driven by a strong radio-frequency signal (RF) at 100 W and at a frequency of about 150 MHz. The plasma is sustained by ionizing neutral atoms.

The main production mechanism of metastable Ar, Ar^*_m, is electron impact excitation of neutral atoms (Ferreira et al., 1985; Bogaerts and Gijbels, 1995; Belostotskiy et al., 2009):

$$\mathrm{Ar} + \mathrm{e}^- (\geq 11.55\,\mathrm{eV}) \rightarrow \mathrm{Ar}^*_m + \mathrm{e}^-, \tag{2.46}$$

where 11.55 eV is the energy difference between the ground state and metastable state. In addition to this direct excitation to the metastable state, there is a contribution of atoms excited to a higher-lying state which cascade down to the metastable state. There are several loss mechanisms by which atoms are lost from the metastable state. Among these are the electron-induced quenching to a close-lying non-metastable state followed by possible radiative decay to the ground state, collisions with the walls and subsequent relaxation, and also metastable-metastable collisions leading to a relaxation of the one and ionization of the other atom. A more detailed discussion is given in Robertz (2023) and in the Ferreira et al. (1985), Bogaerts and Gijbels (1995), and Belostotskiy et al. (2009).

3 Fundamentals of Glaciers

Glaciers can broadly be defined as bodies of ice that originate from the accumulation of snowfall (Cuffey and Paterson, 2010). In the following sections, the process of ice formation from snow and firn and the different zones of glaciers will be introduced. Subsequently, a short overview of the climate history of the Holocene is given, to provide an idea of what to expect for past glacier dynamics.
The introduction to glaciers, their dynamics, properties, and simple models to describe them is based on Cuffey and Paterson (2010) and lecture notes of the 2018 block lecture series by Pascal Bohleber, Kurt Roth, and Josef Lier.

3.1 Glacier Ice Formation

The ice which makes up glaciers has by definition been formed from snow. In this case, the word 'snow' refers to the material that has not been altered from the state in which it precipitated. Once the snow accumulates on the ground and has compacted a little bit the term *firn* is used. The definition is not uniform in the existing literature, however, as the transformation from snow, via firn to ice is continuous, it is hard to draw strict lines of definitions. Cuffey and Paterson (2010) stated among others the following densities for the continuously compacting material: snow: 50-70 $\mathrm{kg/m^3}$, damp new snow: 100-200 $\mathrm{kg/m^3}$, firn: 400-830 $\mathrm{kg/m^3}$, glacier ice: 830-923 $\mathrm{kg/m^3}$. The force driving the compactification is gravity, such that the weight of the snow from above compresses the snow below. It is obvious that the transformation highly depends on the temperature in the snowpack. For higher temperatures, e.g. found in low-lying Alpine glaciers, the snow compacts very quickly and turns into ice within a few ten meters of the firn column. In contrast, for very cold locations such as Antarctica or Greenland, the compactification occurs much slower and densities of ice are reached at depths around 100 m (Cuffey and Paterson (2010) table 2.2).
While in the context of this thesis, firn is not of further interest, the full focus is set on the glacier ice. This is due to the fundamental difference that defines ice as a material with closed-off pores, while in firn the pores are still interconnected. Thus, the *pore close-off depth* is the important depth at which dating with gas-like tracers such as ^{39}Ar becomes feasible. Above this depth, the pores are essentially connected to the atmosphere and gas is exchanged. However, at the close-off depth the formerly connected pores in the firn are sealed off to form individual bubbles. Further densification of the ice is achieved by the compression of these bubbles.
The density of ice where bubbles account for a fraction ν of the total volume can therefore be calculated via

$$\rho = \nu\rho_\mathrm{b} + (1-\nu)\rho_\mathrm{i}, \tag{3.1}$$

with the density of pure glacier ice denoted by ρ_i and the density of the enclosed gas in the bubbles by ρ_b. The former is usually taken as $917\,\mathrm{kg/m^3}$ (for a temperature around $0^\circ\,\mathrm{C}$ and low pressure, Cuffey and Paterson, 2010).

3.1.1 The Age of Ice

As this thesis focuses on ice dating via the radioactive ^{39}Ar isotope, a short comment on its applicability to glaciers is made. With Ar being a noble gas and therefore not taking part in any chemistry, in the natural environment Ar will always be found as a gas. Dating ice with a gas-like tracer therefore poses the question of to what extent the gas partakes in the glacial dynamics. As discussed in the previous section, the glacial material is defined as ice from the moment when its pores are closed and bubbles in the ice are cut off from the atmosphere. From this moment on, atmospheric air is trapped inside the bubbles (also compare section 3.5.2) and the clock of radioactive decay starts ticking. Dating ice with a gas-like tracer therefore dates the moment of the close-off of the bubbles, rather than the moment of the snowfall. The age difference between the ice age and the gas age, often referred to as Δage, therefore needs to be considered. From the discussion in the previous section, it is apparent that this age difference can vary greatly from location to location. Low values will be found for low-lying Alpine glaciers, increasing with altitude and finally reaching up to several thousand years for ice sheets in Antarctica (Cuffey and Paterson, 2010).
For age dating of groundwater and ocean water, the mixing of different water parcels and therefore the mixing of different ages results in the usual approach of assigning age distributions rather than a single age. In the case of glacier ice dating, a simple tracer age is assumed to pose a valid approach. The much higher viscosity of glacier ice compared to water and the selection of sites exhibiting the preservation of clear annual layers present a different situation than in hydrological systems.

3.2 The Zones of a Glacier

Due to the behavior of glacier ice like a viscous fluid, the accumulated ice of an Alpine glacier at the top of a mountain finds its way down the mountain slope in the shape of extended glacier tongues. In this way, the ice reaches low altitudes with higher temperatures where gradually the mass balance of the glacier becomes negative and the ice starts melting. Therefore, to describe the full complexity of a glacier covering a range of altitudes, different zones of a glacier can be identified. Figure 3.1 schematically shows the transition from the accumulation zone (net gain) down to the ablation zones (net loss) (closely following Cuffey and Paterson, 2010):

- *Dry snow zone:* No melting occurs even in summer
- *Percolation zone:* Some melting occurs in this zone, especially during summer. The meltwater percolates into the snow before refreezing at a certain depth, forming ice layers and lenses. The boundary to the *wet snow zone* is reached,

where the entire snow column from the last winter has been raised to melting temperature.

- *Wet snow zone:* The entire snow of the last winter has reached melting temperatures and the melt water has percolated into deeper firn layers from previous years.
- *Superimposed ice zone:* While in the upper zones layers of refrozen ice are discontinuous and covered by firn, in the superimposed ice zone these layers have merged into one large ice layer and are visible at the surface. The upper boundary can be identified as the transition from firn to ice at the end of the snow-melt season. The lower boundary marks the equilibrium line, further below the glacier has a net loss of ice mass over the course of a year.
- *Ablation zone:* The glacier experiences a net loss of mass every year and therefore the bare ice of the glacier is visible without any firn or superimposed ice on top at the end of the melting season. For many current Alpine glaciers, this zone extends to the top of the glacier, as they are not in equilibrium anymore and are losing mass along their entire profile every year.

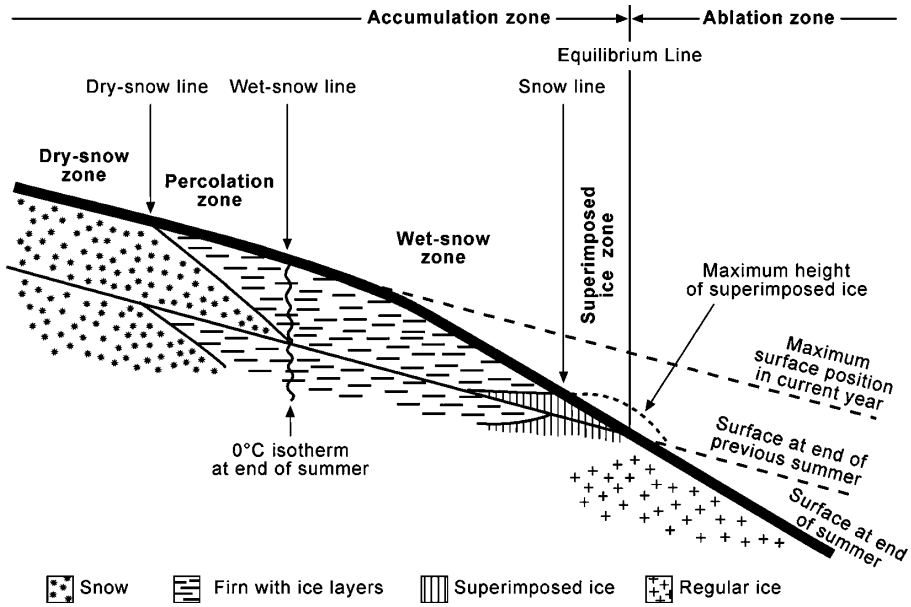

Figure 3.1: The zones of a glacier. Figure taken from Cuffey and Paterson (2010).

3.2.1 Moraines

When the ice of a glacier moves along, it has a strong effect on the topography of its bedrock. Due to its large weight and sliding motion, it scrapes away rock at its interfaces. Furthermore, it can accumulate debris from rockfalls and so on. When reaching an equilibrium state, ice will constantly move downward into the ablation

zone, where the ice is slowly lost. Here, the rocky debris accumulates and forms a so-called terminal moraine. Also along the sides of a glacier tongue, large structures of rocky debris will form in lateral moraines. Due to these structures, the past glacial extent is still visible even when a glacier has long since retreated. As the rocks have often been carved out of the bedrock by the glacial flow, they can be assumed to not have been exposed to daylight before their deposition in the moraine. Therefore, surface exposure dating by cosmogenic nuclides (compare section 8.4) can serve as a valuable method to determine the time of formation of a moraine.

3.3 Stress, Strain and Deformation of Glacier Ice

Ice might seem like a solid material comparable to something like glass, however, it exhibits a very characteristic property, namely that it behaves like a viscous fluid. Thus, under applied stress τ it deforms and flows around obstacles or down a mountain slope. Glacier tongues are the most prominent product of this liquid-like behavior. To approach this property more mathematically, in the following the stress tensor and its relation to the strain rate are discussed.
The entries of the stress tensor $\tau_{i,j}$ are defined as the stress in direction i acting on the surface j. Therefore, the stress vector τ_i is given by

$$\tau_i = \tau_{i,j}(n_j F), \tag{3.2}$$

with n_j the normal vector of a surface with area F. The entries of the stress tensor $\tau_{i,j}$ can be divided into the diagonal elements which represent forces acting perpendicular to a surface as compressive or expansive stress, and into the non-diagonal elements which represent shear stress, acting tangentially on a surface and resulting in shear deformation. Figure 3.2 depicts a scenario of the deformation of an ice block under only normal (left) and pure shear stress (right). In a normal glacier setting, both forces act at the same time, thus thinning and shearing of layers occurs as they move along the flow.
The strain rate of ice $\dot{\epsilon}$, i.e. the relative deformation per time along one axis, is expressed by

$$\dot{\epsilon} = \frac{\partial \epsilon}{\partial t} = \frac{\partial u_x}{\partial x}, \tag{3.3}$$

with the general case again expressed as a tensor:

$$\dot{\epsilon}_{i,j} = \frac{1}{2}\left(\frac{\partial u_i}{\partial x_j} + \frac{\partial u_j}{\partial x_i}\right). \tag{3.4}$$

Empirically, it can be shown that the deformation (strain) rate $\dot{\epsilon}_{i,j}$ is proportional to the n^{th} power of the applied shear stress $\tau_{i,j}$, expressed in *Glen's law*:

$$\dot{\epsilon}_{i,j} = A \cdot \tau_{i,j}^n, \tag{3.5}$$

where the flow parameter A is highly dependent on ice temperature but among others also on ice crystal size and orientation. Both, A and n are determined empirically

with n ranging between 1.5 and 4.2 approximately (Cuffey and Paterson, 2010). Commonly a value of $n = 3$ is used. This stands in contrast to Newtonian viscous fluids which have a linear relation. It means that most of the deformation takes place in regions of highest total stress and therefore typically close to the bed or side margins of a glacier.

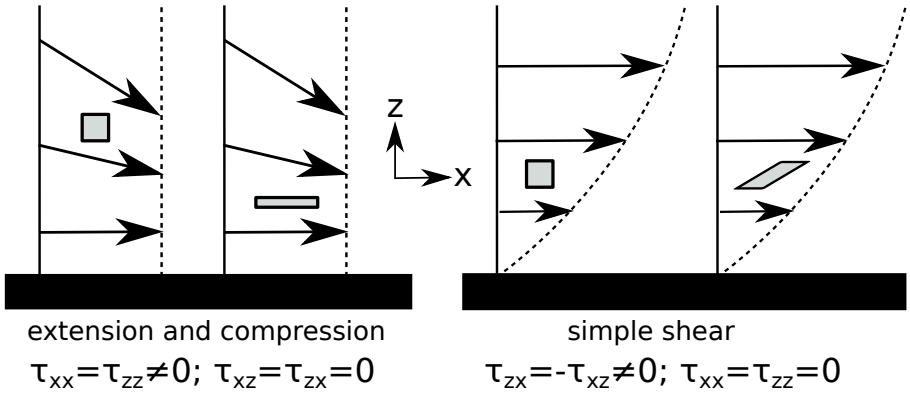

Figure 3.2: A block of ice (shaded area) deforming due to compression/expansion (left) and shear forces (right) along the flow of a glacier. Figure adapted from Cuffey and Paterson (2010).

3.4 Models for Age-Depth Relation of Glaciers

Establishing an age-depth relation for a glacier location or even a single ice core is an important step toward the interpretation of further data and measurements. When layer counting is feasible this is easily done. However, when this is not possible and only a few discrete ages along the ice core are known, a functional relation of age and depth is needed to find a continuous profile.
Modeling the age-depth relation can be done in very intricate ways (e.g. see a 3D full Stokes ice flow model by Licciulli et al., 2020), however, as the focus of this thesis is not the ultra-precise modeling of specific glacier sites it will be restricted to simpler models based on simplified glacier dynamics.

The Nye-timescale

Derived from Glen's flow law, the Nye-timescale (Nye, 1957, 1963; Cuffey and Paterson, 2010) is an early approach to age-depth relationships. It links the age at a certain depth in a kinematic approach with the average vertical velocity over the ice column:

$$\Delta t = \frac{\Delta z}{u_z(z)} \Rightarrow t(z) = \int_0^z \frac{dz'}{u_z(z')}, \tag{3.6}$$

where t is the age of the ice (time since snowfall) and $u_z(z)$ the vertical velocity at depth z. Furthermore, $z = 0$ is set at the glacier surface with the z-axis pointing

downwards. In the model, depth is always given in meters of water equivalent (m w.e.). Here, an expression for $u_z(z)$ is needed.
With the mass balance in m w.e., an equation linking the accumulation rate b to the sum of temporal ice thickness change and spatial changes in the ice thickness H and horizontal velocity u_x is given by:

$$\frac{\partial H}{\partial t} + \frac{\partial}{\partial x}(u_x \cdot H) = b. \tag{3.7}$$

Assuming a spatially and temporally constant H this equation simplifies to

$$\frac{\partial u_x}{\partial x} = \frac{b}{H}. \tag{3.8}$$

With the assumption of incompressible ice ($\frac{\partial u_x}{\partial x} + \frac{\partial u_z}{\partial z} = 0$), equation 3.8 can be rewritten for the vertical velocity. Integrating over z then leads to:

$$u_z(z) = b\left(1 - \frac{z}{H}\right) \tag{3.9}$$

and by inserting into equation 3.6 the wanted age-depth relationship is obtained:

$$t(z) = \frac{H}{b}\ln\left(1 - \frac{z}{H}\right). \tag{3.10}$$

The vertical velocity derived in equation 3.9 therefore linearly decreases with depth while the age increases logarithmically with depth. This model works well for the upper 2/3 of the glacier, however, below it leads to an inconsistency at the ice-rock interface. Here, $u_x(H) \neq 0$ follows from equation 3.8 which contradicts the idea of the glacier being frozen to the bedrock. Furthermore, this model is rather suited for mountain slopes while our glacier location of interest is more of an ice-divide type. Here, the ice flow can differ significantly and therefore needs further discussion.

The Raymond model

The interest in ice-divide-type settings comes from the central regions of the large ice sheets in Greenland and Antarctica. Raymond (1983), therefore, calculated the strain rate for an isothermal ice divide from an idealized model of such a divide. The strain rate is linear for this case:

$$\dot{\epsilon} = -\frac{2b}{H}\left(1 - \frac{z}{H}\right). \tag{3.11}$$

Using equation 3.3, the vertical velocity $u_z(z)$ is determined, and from that the age-depth relation is calculated with equation 3.6:

$$t(z) = -\frac{H}{b}\left(1 - \frac{1}{1 - z/H}\right). \tag{3.12}$$

The main restriction of this model is the assumption of isothermal conditions through the ice column. However, while for polar ice sheets where temperatures differ by up

to 60° C (Cuffey and Paterson, 2010) this is certainly a drawback, for thin alpine glaciers like the later discussed Weissseespitze this should not play a significant role. In this case, the temperature profile varies with season rather than depth. Fischer et al. (2022) show temperature data for the WSS over several years where a variation of a few degrees is visible for layers near the surface. However, averaging these fluctuations over a year gives an almost isothermal ice body.

The 2p model

The Raymond model was later generalized by Bolzan (1985), who introduced a "thinning parameter" p in addition to the accumulation rate b. In the attempt to approximate the ice sheet as a two-layer system, this second parameter accounts for different temperature distributions in the ice, which highly influence the viscosity and thus the parameter A in Glen's law 3.5. The resulting age-depth relation stated in Jenk et al. (2009) is given by

$$t(z) = -\frac{H}{bp}\left(1 - \frac{1}{(1 - z/H)^p}\right), \tag{3.13}$$

which for $p = 1$ is equivalent to 3.12.

3.5 Diffusion

Diffusion is a process by which matter or heat is transported through a system as a result of random molecular motion. Effectively, it leads to a net transport along a gradient, thus smoothing out concentration or heat differences.
The first scientists who took a quantitative approach to diffusion were Fourier (1822) on the subject of heat conduction and later Fick (1855) who applied the formulas to diffusion. The underlying understanding is that the rate of transfer of a diffusing substance through a unit area is proportional to the concentration gradient measured normal to the section, as stated in **Fick's first law**:

$$J = -D\frac{\partial C}{\partial x}, \tag{3.14}$$

with J being the diffusion flux (amount of substance per unit area per unit time [n/m^2·s]), C the concentration of the diffusing substance, and D the *diffusion coefficient* in [m^2/s]. The negative sign arises because diffusion occurs opposite to the concentration gradient.
Using the law of mass conservation

$$\frac{\partial C}{\partial t} + \frac{\partial}{\partial x}J = 0, \tag{3.15}$$

and inserting it into equation 3.14 and assuming a constant D yields the fundamental differential equation of diffusion known as **Fick's second law**:

$$\frac{\partial C}{\partial t} = D\frac{\partial^2 C}{\partial x^2}. \tag{3.16}$$

3.5.1 Diffusion in a Cylinder

As the systems in which diffusion is explored in this thesis are cylindrical-shaped ice cores, the standard cartesian coordinate system is not convenient. Fick's second law 3.16 reformulated in the more convenient cylindrical coordinates with radial diffusion then becomes

$$\frac{\partial C}{\partial t} = \frac{1}{r}\frac{\partial}{\partial r}\left(rD\frac{\partial C}{\partial r}\right). \tag{3.17}$$

For the case of diffusion into a cylindrical ice core, the situation is best described by initial conditions with a constant concentration C_0 outside of the cylinder of radius a and an initial uniform concentration C_1 inside the cylinder, thus:

$$C = C_0 \text{ for } r = a \text{ and } t \geq 0, \tag{3.18}$$

and

$$C = C_1 \text{ for } r \leq a \text{ and } t = 0. \tag{3.19}$$

The solution is given by Crank (1975) as

$$C(r,t) = C_1 + (C_0 - C_1)\left(1 - \frac{2}{a}\sum_{n=1}^{\infty}\frac{\exp(-D\alpha_n^2 t)J_0(r\alpha_n)}{\alpha_n J_1(a\alpha_n)}\right), \tag{3.20}$$

where $J_k(x)$ is the Bessel function of the first kind of order k while α_n are the positive numbers that fulfill $J_0(a\alpha_n) = 0$. Crank (1975) also provides a solution for small times (Dt/a^2 small) and provided r/a is not small:

$$\begin{aligned} C(r,t) = C_1 + (C_0 - C_1)\frac{a^{1/2}}{r^{1/2}}\,\text{erfc}\,\frac{a-r}{2\sqrt{Dt}} + \frac{(a-r)(Dta)^{1/2}}{4ar^{3/2}}\,\text{i erfc}\,\frac{a-r}{2\sqrt{Dt}} \\ + \frac{(9a^2 - 7r^2 - 2ar)Dt}{32a^{3/2}r^{5/2}}\,\text{i}^2\text{erfc}\,\frac{a-r}{2\sqrt{Dt}} + ..., \end{aligned} \tag{3.21}$$

with the error-function complement

$$\text{erfc}\, z = 1 - \text{erf}\, z = \frac{2}{\pi^{1/2}}\int_z^{\infty}\exp(-\eta^2)\mathrm{d}\eta. \tag{3.22}$$

Equation 3.21 can be rewritten in terms of the two dimensionless parameters Dt/a^2 and r/a as long as the former is small ($Dt/a^2 \ll 1$) and r/a not small. Both are fulfilled in all applications throughout this thesis.

Mean Concentration

As this thesis aims to develop a better constraint on the diffusion of Ar in ice by measurements of the rare isotope ^{39}Ar on whole sections of ice cores, there is no access to the detailed radial profile of the diffusing gas. Rather, the bulk of the entered gas is measured and then the diffusion coefficient is calculated. Therefore, the measured concentration has to be compared to the radial integral over equation 3.20:

$$\bar{C}(t) = \frac{1}{\pi a^2}\int_0^{2\pi}\int_0^a C(r,t)\cdot r\mathrm{d}r\mathrm{d}\phi \;=\; \frac{2}{a^2}\int_0^a C(r,t)\cdot r\mathrm{d}r. \tag{3.23}$$

The integral is not solved analytically but computed numerically in this thesis.

3.5.2 Diffusion in Ice

When studying ice cores and trying to infer e.g. past climatic conditions from the gases and other tracers within the ice core, great attention has to be paid to any effects altering the concentration of such tracers apart from the original atmospheric value. When dealing with noble gases, at least any chemical altering of their concentration can be ruled out. However, attention has to be paid to possible effects due to diffusion. On the one hand, diffusion already happens in the ice sheet possibly smearing out signals along an ice core (Bereiter et al., 2014; Pol et al., 2010). On the other hand, once the ice core has been extracted and is stored it is very vulnerable to diffusive contamination by atmospheric air due to its small volume and large surface. E.g. helium, having a small collision diameter, exhibits a very fast diffusion in ice (Gordon Davy and Miller, 1970; Satoh et al., 1996; Friedrich, 2003) which makes storage prior to the analysis impossible. In general, measurements have shown a critical collision diameter of about 3.6 Å, above which diffusion in ice is highly suppressed (Huber et al., 2006). This critical threshold was mainly observed when comparing O_2/N_2 and Ar/N_2 ratios in ice cores, where O_2 and Ar exhibit collision diameters slightly below the threshold while the one of N_2 is slightly above (Craig et al., 1988; Sowers et al., 1989; Bender et al., 1995; Ikeda-Fukazawa et al., 2005; Bereiter et al., 2009; Suwa and Bender, 2008; Kobashi et al., 2015). Also compare figure 3.3. This threshold is caused by the diffusion in ice presumably being limited by the size of the channels in the ice matrix (steric diffusion), meaning that the size of the channels is of the same order as the size of the molecules (or atoms in the case of Ar). Huber et al. (2006) argues that the size of the hexagonal passages in the ice, which are each formed by six H_2O molecules, is about the critical size of 3.6 Å. Compared to this, they list the collision diameters given by Reid (1966) as 3.467 Å for O_2, 3.542 Å for Ar and 3.798 Å for N_2, which shows that Ar and O_2 are just below, N_2 just above the threshold.
However, there is little experimental data to constrain the diffusivities and present values for the diffusion coefficient of Ar as well as O_2 and N_2. The only attempt to measure the diffusion coefficient for Ar that the author is aware of is by Satoh et al. (1996), who determined the diffusivities of He, Ne, and Ar in ice by supersaturating glacial as well as artificial ice and measuring the emitted gas over time. Their results are shown in figure 3.4. For Ar, they obtained only one data point with large uncertainties in the order of $10^{-11}\ \frac{m^2}{s}$ at 263 K.
Efforts have been made to simulate the diffusion process and understand its working principle. Ikeda-Fukazawa et al. (2002), Ikeda-Fukazawa et al. (2004b) and Ikeda-Fukazawa et al. (2004a) for example were able to understand the principle of diffusion as one which breaks the hydrogen bonds, thus, calculating values much larger than previous estimates (compare figure 3.4), which still concluded that diffusion of O_2 and N_2 would be negligible. All these simulations were done for ice from depths where the gas molecules are dissolved in the ice crystal in the clathrate hydrates and where diffusion is driven by the concentration gradient. They used the potential barrier, calculated from the potential energies of the atoms in the lattice for the

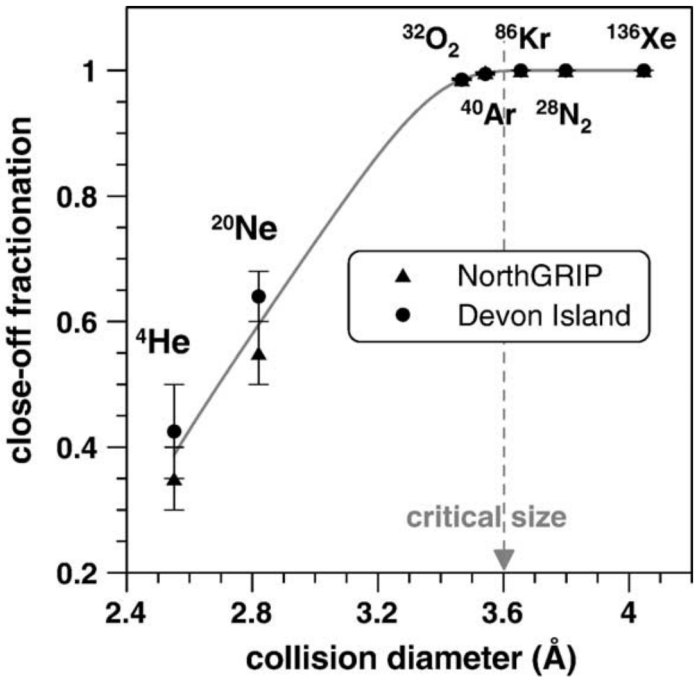

Figure 3.3: Fractionation factors of gases during bubble close-off from model fits plotted against their diameter (diameter values taken from Reid, 1966). Ar is slightly below the critical size of 3.6 Å, above which no fractionation is visible. Figure from Huber et al. (2006).

activation energy Q of the Arrhenius equation:

$$D = D_0 \exp\left(-\frac{Q}{RT}\right), \tag{3.24}$$

where D_0 is the maximal diffusivity at infinite temperature, $R = 8.314\,\mathrm{m^3PaK^{-1}mol^{-1}}$ the universal gas constant, and T the temperature.
Finally, Kobashi et al. (2015) using the results of Ikeda-Fukazawa et al. (2004b) estimates a diffusion coefficient for Ar at 270 K of $D_{\mathrm{Ar}} = 4.0 \cdot 10^{-11}\,\mathrm{m^2s^{-1}}$.
When investigating diffusion during storage, diffusion coefficients for temperatures around -20 °(253 K) are of special interest. Kobashi et al. (2015) presents the following geometrical relationship between the diffusivities of O_2, Ar, and N_2 which provides a temperature-dependent D_{Ar}:

$$D_{\mathrm{Ar}}(T) = D_{\mathrm{O_2}}(T) - \frac{D_{\mathrm{O_2}}(270\,\mathrm{K}) - D_{\mathrm{Ar}}(270\,\mathrm{K})}{D_{\mathrm{O_2}}(270\,\mathrm{K}) - D_{\mathrm{N_2}}(270\,\mathrm{K})} \cdot (D_{\mathrm{O_2}}(T) - D_{\mathrm{N_2}}(T)). \tag{3.25}$$

The values for O_2 and N_2 are calculated with equation 3.24 using the following constants from Ikeda-Fukazawa et al. (2005): $D_{\mathrm{O_2},0} = 3.5 \cdot 10^{-9}\frac{\mathrm{m^2}}{\mathrm{s}}$, $Q_{\mathrm{O_2}} = 9700\frac{\mathrm{J}}{\mathrm{mol}}$, $D_{\mathrm{N_2},0} = 2.0 \cdot 10^{-10}\frac{\mathrm{m^2}}{\mathrm{s}}$, $Q_{\mathrm{N_2}} = 5100\frac{\mathrm{J}}{\mathrm{mol}}$.
The resulting diffusivity of Ar at 253 K is $D_{\mathrm{Ar,253K}} = 3.0 \cdot 10^{-11}\frac{\mathrm{m^2}}{\mathrm{s}}$.

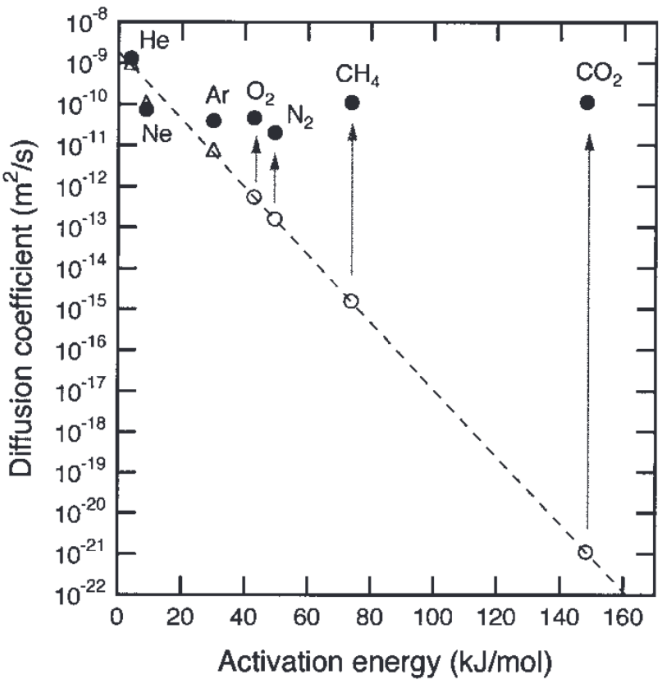

Figure 3.4: Diffusion coefficient D plotted against the potential barrier ΔE for atmospheric gases at 270K. The open triangles are the experimental data from Kahane et al. (1969) and Haas et al. (1971) for He and Ne, and Satoh et al. (1996) for Ar. The open circles are estimates under the assumption of the interstitial diffusion mechanism. The solid circles show the results of Ikeda-Fukazawa et al. (2004b). Figure from Ikeda-Fukazawa et al. (2004b).

Diffusion in Bubbly Ice

So far diffusion has been discussed only for pure ice. However, there are air bubbles present in the ice from alpine glaciers. This changes the situation significantly as one has to think of diffusion in ice with bubbles as a process involving a large reservoir of gases (bubbles) and a medium through which the diffusion takes place (ice). With the focus on the effects of possible atmospheric contamination by diffusion into an ice core, the scenario consists of the following steps: (1) Atmospheric gas dissolving into the ice. The amount of gas per ice volume depends mainly on the solubility of the gas in the ice. (2) Diffusion of the gas inside the ice, driven by a concentration gradient. This can be seen as the bottleneck of the process. (3) Diffusive concentration changes in the ice along the concentration gradient will immediately be compensated by the gas exchange of ice and bubbles. (4) Over time, the concentration gradient in the bubbles will be balanced due to the diffusive flux. In a recent publication, Yi and Han (2024) investigated the diffusion process of noble gases between bubbles theoretically and identified the first step, the dissolution of the gasses as the rate-limiting step. Yan et al. (2019) introduced the idea of scaling the diffusivity simply by the ratio of gas molecules in ice and bubbles in order to account for the bubbles. Thus, the

effective diffusivity is given by

$$D_{\text{eff}} = Z \cdot D, \tag{3.26}$$

where D is the normal diffusion coefficient and

$$Z = \frac{n_{\text{Ar,ice}}}{n_{\text{Ar,bub}}}. \tag{3.27}$$

with $n_{\text{Ar,ice}}$ and $n_{\text{Ar,bub}}$ the number of Ar atoms in the ice and bubbles, respectively. $n_{\text{Ar,ice}} \ll n_{\text{Ar,bub}}$ is assumed.
The number of Ar atoms in the bubbles can be derived from the total number of molecules/atoms in the bubbles and the molar fraction of Ar in the air f_{Ar}. With the ideal gas law, this becomes

$$n_{\text{Ar,bub}} = \frac{p_0 V m_{\text{ice}}}{R T_0} \cdot f_{\text{Ar}}, \tag{3.28}$$

where $p_0 = 101325$ Pa is the atmospheric pressure, V the gas content in ice in $\frac{\text{m}^3}{\text{kg}}$, m_{ice} the mass of the ice sample, R the universal gas constant and temperature $T_0 = 273\,\text{K}$.
The gas content V was calculated by the measured mass m_{ice} and the volume V_g of the extracted gas:

$$V = \frac{V_g}{m_{\text{ice}}}. \tag{3.29}$$

The number of Ar molecules in the ice phase depends on the solubility S_{Ar}, the partial pressure P_{Ar}, and the number of water molecules n_{ice}:

$$n_{\text{Ar,ice}} = S_{\text{Ar}} \cdot P_{\text{Ar}} \cdot n_{\text{ice}}. \tag{3.30}$$

The number of water molecules is given by:

$$n_{\text{ice}} = \frac{m_{\text{ice}}}{M_{\text{H}_2\text{O}}} \tag{3.31}$$

with $M_{\text{H}_2\text{O}} = 0.018\,\text{kg}\,\text{mol}^{-1}$ the molecular weight of water.
The pressure inside the bubbles is in this case assumed to be atmospheric as the depth of alpine ice cores suitable for Ar dating is comparably low and due to the relaxation of the pressure inside the bubbles as argued by Bender et al. (1995). Therefore, the partial pressure is given by

$$P = p_0 \cdot f_{\text{Ar}}. \tag{3.32}$$

Inserted into equation 3.27 one obtains

$$Z = \frac{S \cdot R \cdot T_0}{V \cdot M_{\text{H}_2\text{O}}}. \tag{3.33}$$

The solubility follows the same temperature-dependency as the diffusivity in equation 3.24 (Ikeda-Fukazawa et al., 2005):

$$S = S_0 \exp\left(-\frac{E}{RT}\right), \tag{3.34}$$

where S_0 is the maximum solubility at infinite temperature and E is the activation energy for solution. As $S_{0,\mathrm{Ar}}$ is not available, a similar approach as in equation 3.25 is provided by Kobashi et al. (2015) for solubilities:

$$S_{\mathrm{Ar}}(T) = S_{\mathrm{O_2}}(T) - \frac{D_{\mathrm{O_2}}(270\,\mathrm{K}) - D_{\mathrm{Ar}}(270\,\mathrm{K})}{D_{\mathrm{O_2}}(270\,\mathrm{K}) - D_{\mathrm{N_2}}(270\,\mathrm{K})} \cdot (S_{\mathrm{O_2}}(T) - S_{\mathrm{N_2}}(T)), \tag{3.35}$$

for which the additional constants $S_{\mathrm{O_2},0} = 3.7 \cdot 10^{-13}\,\mathrm{Pa}^{-1}$, $E_{\mathrm{O_2}} = 7900\,\frac{\mathrm{J}}{\mathrm{mol}}$, $S_{\mathrm{N_2},0} = 4.5 \cdot 10^{-13}\,\mathrm{Pa}^{-1}$, and $E_{\mathrm{N_2}} = 9200\,\frac{\mathrm{J}}{\mathrm{mol}}$, (Ikeda-Fukazawa et al., 2005) are used.
The resulting solubility of Ar at 253 K is $S_{\mathrm{Ar},253\,\mathrm{K}} = 7.9 \cdot 10^{-15}\,\mathrm{Pa}^{-1}$.
To give a number to these equations, for the sample DDG-41, further discussed in chapter 6, $1/Z$ resulted in about 75000, which means that 75000 times more Ar is located in the bubbles than in the ice matrix.

3.6 Holocene Climate Variability

While ice cores from the polar regions cover periods of up to several hundred thousand years and therefore the climate variability between glacial and interglacial periods, ice cores from the Alpine regions commonly cover only the last interglacial period, namely the Holocene. However, also the Holocene in itself did not consist of a stable climate. While the current man-made climate change is well known, earlier climate variations are not so much a matter of common knowledge. Therefore, in the following, a brief and by no means complete overview of some of the more pronounced climatic variations of the Holocene is given. The reason for this discussion is that in order to put the knowledge drawn from the different ice dating projects in the following chapters into context, these climate variations are of course one of the defining factors of the glaciation of Alpine regions. The following section closely follows the overview by Wanner et al. (2008) and Wanner et al. (2015) and will mainly mention the different warm and cold periods, as the discussion about their causes and consequences is beyond the scope of this thesis and the debate about the exact drivers, timings, and amplitudes is ongoing.
The Holocene started with the transition of the colder climate of the Younger Dryas to warmer conditions about 11.7 ka BP. Since then, the climate has experienced several multi-decadal to century-scale cooling intervals.
In a very simple approach, the Holocene can be subdivided into four periods. An early Holocene with continuous warming, especially in the Northern Hemisphere between roughly 11.7 and 8-7 ka BP. A middle Holocene with warm temperatures between 8-7 and 5-4 ka BP. A cooler late Holocene between 5-4 ka BP and the onset of the industrialization around 1860 CE, and the warming Industrial Era since about 1860 CE.
The change from the warm middle Holocene to the gradually cooling late Holocene was most probably triggered by the declining orbitally driven insolation in the Northern Hemisphere during the boreal summer. Data suggests that since the Holocene Climatic Optimum, a cooling occurred in the Northern Hemisphere until

the beginning of the Industrial Era (Wanner et al., 2015). With this cooling, reglaciation of the Alpine regions went along, after the ice coverage had presumably reached lower levels than the current ones in the middle Holocene.
The cooling trend after the Holocene Climatic Optimum can be reconstructed from proxy compilations (e.g. Marcott et al., 2013) but stands in contrast to Earth system model simulations which suggest a global warming trend (Liu et al., 2014; Osman et al., 2021). This discrepancy is referred to as the 'Holocene temperature conundrum' (Liu et al., 2014; Essell et al., 2024). Essell et al. (2024) argues that it originates from a bias of the proxy-based large-scale reconstructions towards the Northern Hemisphere, thus not capturing the global mean temperature trend which should have remained stable. On the Northern Hemisphere, orbital forcing led to decreasing summer insolation in the course of the Holocene (Wanner et al., 2008). Therefore, the argued cooling trend after the Holocene Climatic Optimum peaking in the LIA should be understood as a Northern Hemisphere phenomenon with local spatiotemporal variations and not a global one.
Overlaid on this general Northern Hemisphere cooling trend are several multi-decadal to centennial temperature variations. For example, the time of the Roman Empire experienced warmer temperatures until about 500 CE. There is then evidence for a potential cooling during the European Migration Period around 650 CE before the Medieval Warm Period caused warm temperatures again between 700-1000 CE. Subsequently, probably as a result of the general cooling trend being reinforced by major volcanic eruptions, approximately from the year 1300 CE the Little Ice Age (LIA) caused a distinct cooling. During the LIA, glaciers experienced a strong advance, reaching sizes unprecedented at any other point during the Holocene peaking around 1850 CE before giving way to the warming trend of the Industrial Era. For more background on the Little Ice Age please refer to PAGES 2k Consortium (2013), Breitenmoser et al. (2012), Wanner et al. (2022), and Matthews and Briffa (2005). Since 1850 CE, the current warming trend has led to increasing temperatures on a global scale (Neukom et al., 2019) with accelerated impacts since the 1980s (Wanner et al., 2022) and significantly reducing glacier sizes around the world.
All in all, when focussing on the European Alps, the major glacial dynamics of the Holocene can be summarized as the following: during the early and middle Holocene, the Alps lost most of their glaciers below 4500 m resulting in less ice cover than found today. With the onset of the late Holocene, a neoglaciation took place which is nicely seen by the findings of ice with younger ages the more lower-lying the glaciers are (Bohleber et al. (2020), figure 4). The neoglaciation reached its maximum during the LIA around 1850 CE when glacier coverage in the Alps was higher than throughout the entire Holocene before. This also resulted in the emergence of large moraines along the ice margins of the LIA glacier positions, 'overwriting' large parts of the earlier moraine record but still providing valuable evidence for the past glacial dynamics (e.g. Braumann et al., 2021).

4 Methods

In the following chapter the different steps from retrieving a sample at the glacier site, to the gas extraction at the Institute of Environmental Physics, Heidelberg (IUP), and finally to the measurement in the ArTTA lab at the Kirchhoff-Institute for Physics, Heidelberg (KIP) are portrait. Furthermore, a summary of the ATTA measurement method and its different components is given.

4.1 Ice Sampling Methods

There are different ways to retrieve ice samples from a glacier. A very simple approach is to cut ice blocks from the surface of a glacier or other accessible places, e.g. glacier caves (Feng et al., 2019) or ice caves (Colucci et al., in preparation). This method easily provides large amounts of ice, however, it is very limited in its accessibility to the stratigraphy of the glacier as it is restricted more or less to the surface. A much more widely used way to retrieve glacier ice is by coring or drilling. In this case, a hollow coring drill is used to, step by step, drill down into a glacier, every time retrieving a core with the length of the drill set. With this method, the whole ice column of a glacier is accessible, which in the Alps amounts up to several tens or few hundreds of meters (Bohleber, 2019), at the poles to several kilometers (Cuffey and Paterson, 2010). The drills can have different diameters and thus retrieve different amounts of ice per depth. Within the scope of this thesis, ice cores with 2" to 3" diameters were taken. The drawback for a method like ^{39}Ar dating, which requires large amounts of ice (approx. 1-4 kg per sample) is the loss of high-depth resolution as long sections of an ice core might be required per sample. The obvious advantage of coring is the access to the whole depth and thus also to the age profile of a glacier. This way, depending on the location, continuous age records can be obtained with an ice core, e.g. reaching back 800 ka (Jouzel et al., 2007). In the case of drilling, there are several methods available. The ice core can be drilled mechanically or thermally (Talalay et al., 2015) depending on the needs in the field. In the fieldwork leading up to this thesis, all the above-mentioned retrieval methods were applied to varying degrees.

4.2 Argon Gas Extraction from Ice Samples

After the sampling in the field, the ice samples were usually transported to the cold rooms (which are kept at about -20° C) at the IUP in styrofoam boxes. Thereafter, the first step towards the extraction of gas from the ice sample is its cleaning. To

a) b) c)

Figure 4.1: Images of the ice sample preparation: **a)** Cutting off potentially melted and refrozen layers off the surface of an ice block; **b)** Ice core sample after decontamination in the melting vessel; **c)** Melting vessel cooled and evacuated, connected to the extraction line just before melting.

prevent any contamination of the later gas sample by e.g. refrozen meltwater on the outside or in cracks of a sample, thus entrapping modern atmospheric air, a few millimeters of ice are shaved off the outside of the ice cores or blocks, and cracks are scraped out. The smaller the surface-to-volume ratio, the less important role this contamination possibly plays. Therefore, ice cores with large diameters or large ice blocks with no cracks are preferable. Apart from this possible contamination by entrapped atmospheric air, the handling of an ice sample is done very straightforwardly. Different from e.g. radiocarbon analysis, where great care has to be taken for very clean handling and processing of the ice core (Hoffmann et al., 2018), the noble gas extraction from ice cores can be done without a special protocol. A second reason for the removal of the outside layers is the effect of Ar diffusion into the ice during storage (compare chapter 6), which mainly affects the outermost layers.
The prepared ice samples are weighed and put into a 12.6 l stainless steel bucket (compare figure 4.1), which can be closed with a large ISO-K to ISO-KF25 adaptor flange. The bucket is transported to the extraction lab while being cooled in a styrofoam box with dry ice and subsequently attached to the extraction line.

The extraction line was set up by Beyersdorfer (2016) and further developed and characterized by Hopkins (2018). In recent years the extraction lab was supervised and upgraded for a broader range of sample types by Arck (2019) and Arck (2024). The sample preparation procedure for ice samples was already applied in the scope of the work by Feng et al. (2019) for a limited amount of samples. However, during the work performed within this thesis, the extraction procedure was further refined and put into a routine working mode. As the extraction steps were already discussed

in several master and bachelor theses supervised in the scope of this thesis (Krastel, 2022; von Reventlow, 2022; Marks, 2024; Langenbacher, 2024), the steps will only be summarized here. A technical drawing of the extraction line can be found in figure 4.2
Once the ice sample bucket is connected to the extraction line via an ISO-KF25 valve, it is evacuated for about 45 minutes until pressures of around 10^{-2} mbar are reached. The flanges are then leak tested and once the tightness is assured the melting of the ice can be initiated. This is done by putting the bucket into a bath of hot water, while its valve is kept close. Once the ice is entirely melted, the valve can be opened and the gas from the bubbles in the ice (and water vapor) is transported into the extraction line. For a thorough degassing, the bucket is gently shaken. Coming from the bucket, the gas passes a water trap, cooled to about -75° C by a dry-ice-isopropanol mixture, and is then guided onto a gas trap.

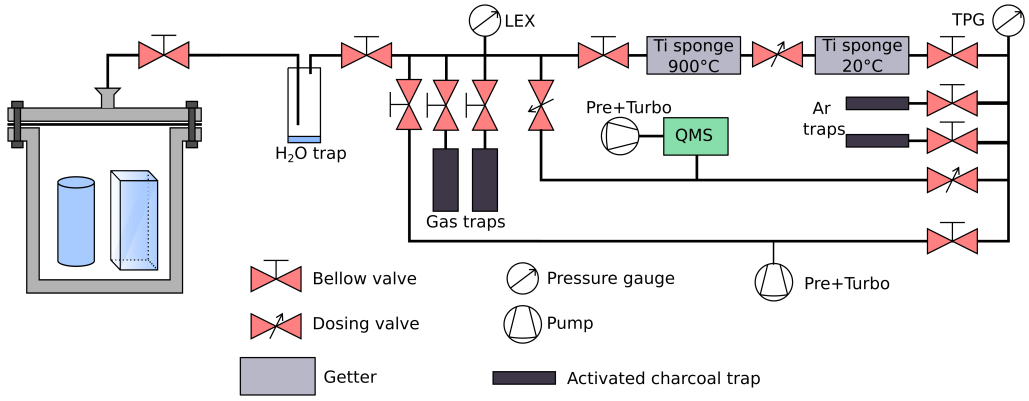

Figure 4.2: Technical drawing of the extraction line for Ar gas from ice samples adapted from Arck (2024). For details see main text.

The gas traps used in the setup are liquid nitrogen-cooled activated charcoal traps (ACTs) of different sizes, depending on the gas amount they are supposed to trap. When cooled to -196° C they behave like suction pumps and adsorb nearly all Ar. To release the gas again, the traps are heated to 150° C by an induction heating device. Once all gas from the ice has been trapped onto the ACT, the valves to the ice bucket and water trap are closed. The ACT can now be heated out and the gas amount and gas composition are checked. For the latter, a quadrupole mass spectrometer (QMS) of type RGA SRS-100 is employed.
The next step is the purification of the gas. Coming from air bubbles, it roughly has an atmospheric composition. Two titanium sponge getters are employed to remove all non-noble gases. The first one at 900° C for reactive gases like N_2, O_2 and CO_2, and the second one at room temperature to adsorb residual H_2. Behind the getters, another ACT is trapping the >98% pure Ar gas. Another step of measuring the gas amount and composition is done here before the gas is frozen onto the final, mobile ACT. This one can then be stored until the measurement in the ATTA lab.

4.3 Overview of the ArTTA Apparatus

The following section gives an overview of the individual components of the ATTA experiment as it is currently set up in the ATTA 1 lab at the KIP in Heidelberg

The effort to establish an ATTA laboratory, also called Argon Trap Trace Analysis (ArTTA) laboratory in Heidelberg dates back to the work of Welte (2011). The hyperfine spectroscopy of ^{39}Ar was conducted (Welte et al., 2009) and first estimations of the ^{39}Ar countrate for atmospheric samples predicted a value of 6 ^{39}Ar atoms per hour (Welte et al., 2010), a value which has been reached in the time frame of the here presented project. Shortly after, a first measurement on ^{39}Ar atoms in an atmospheric sample was reported by Jiang et al. (2011), however, with too low count rates for actual environmental applications. This changed with the work by Ritterbusch et al. (2014) from the laboratory in Heidelberg which reported a count rate of around 3.5 $^{39}\mathrm{Ar\,h^{-1}}$ for modern samples during a groundwater campaign. Furthermore, an intercomparison study with LLC results from the University of Bern successfully confirmed the proportionality of ^{39}Ar-ATTA. The groundwater samples were taken in the vicinity of Heidelberg and revealed ages between modern and more than 644 a already showing the applicability of the ^{39}Ar dating range for typical groundwater systems.
In the following years, further progress of the method in Heidelberg was made by Ebser (2018) who first reached count rates of 6-7 $^{39}\mathrm{Ar\,h^{-1}}$ and established the gas recycling mode for measurements, thus enabling much smaller sample sizes of few kg of water or ice. Furthermore, he developed a Bayesian analysis of the measurement data and applied the ^{39}Ar dating tracer to ocean ventilation (Ebser et al., 2018). Furthermore, Feng et al. (2017) put effort into the development of optimized transversal cooling of the atom beam, applied ^{39}Ar for the first time to ice samples (Feng et al., 2019), and started the work on a second ATTA lab (Feng, 2019) in Heidelberg. While continuing the work on the second lab, Ringena (2021) also demonstrated for the first time that trapping Kr and Ar isotopes at the same experiment with good count rates is possible, thereby showing the feasibility of a *dual-ATTA*. Schmidt (2021) then pushed the measurement of different environmental samples forward with a focus on gas-rich limnological samples, built a new pre-vacuum for the ATTA 1 lab, and provided the code for the Bayesian sample analysis. With a running and continuously measuring ATTA 1 lab, Robertz (2023) worked in the ATTA 2 lab to deepen the understanding of the velocity distributions in the atom beam, setting up better beam diagnostic tools and gaining a better understanding of the plasma source.

Figure 4.3 shows a schematic overview of the ATTA experiment. It includes the vacuum parts and also optical components for the cooling and trapping of the atoms. Note that the figure is only an overview and lacks the exact details, especially about the pre-vacuum and inlet part. However, it shows the most important details and can therefore serve to understand the general setup.
In the following, the components of the apparatus will be introduced from left to right.

As all components have been discussed in earlier theses from the ATTA Heidelberg group, most parts and their working principle will only be briefly discussed and the literature with more detailed elaboration is indicated.

Vacuum System

The vacuum system is designed to meet the trade-off of a maximal inflow of gas through the source tube and the need for minimal background pressure in the MOT chamber. For this purpose, the first vacuum chamber is equipped with two 2000 l/s turbo-molecular pumps (TMP) which keep background pressures at a minimum. In routine operation mode, the working pressure inside the source chamber is at $8 \cdot 10^{-6}$ mbar while the pressure in the MOT chamber stays around $2.5 \cdot 10^{-7}$ mbar. Ebser (2018) provides a first model of the vacuum system, indicating the need for differential pumping stages to achieve a steep pressure gradient in the system. However, during the course of this thesis, the differential pumping stages between the source chamber and the 2D-MOT chamber were removed, as the work by Kindermann (2024) and Moraw (2024) indicated a large local pressure increase within the stages which could lead to deexcitation of the metastable atoms. The differential pumping stages further downstream are still installed but will be removed at the next larger vacuum system alteration.
Downstream of the source chamber, each chamber is pumped with a 300 l/s TMP. All outflows of the TMPs are joined and the gas is compressed into a reservoir with a 50 l/s TMP. In recycling mode, the gas then reenters the source chamber from the reservoir, in throughflow mode, the reservoir is pumped by another 50 l/s TMP and a Pfeiffer ACP 15 roots vacuum pump.
To keep the sample gas clean over the 20 h of routine measurement time, two getters are installed. One is a commercial SAES CapaciTorr HV 200 which is heated and can absorb a wide variety of gases. Due to ongoing problems with high hydrogen levels, a second getter aimed at hydrogen removal was installed which consists of an activated titanium sponge and is operated at room temperature.
Furthermore, an RGA SRS100 quadrupole mass spectrometer is attached to the source chamber and enables a live gas composition analysis in the vacuum system.

Plasma Discharge Source

From the reservoir, the gas flows through the plasma discharge source. To enable subsequent laser cooling it is necessary to excite the atoms to a metastable energy state, from where the atoms can be manipulated with ordinary lasers (compare sections 2.2 and 2.6). To ignite a plasma, high pressures are needed. Therefore, the source tube has a small inner diameter of 10 mm. For the rf-fields to enter, it cannot be metallic and is therefore made of Al_2O_3. Around the last part of the tube, an antenna is wound (compare figure 4.4) which provides the driving rf-field of the plasma. The antenna has a length of 110 cm and usually shows a slight resonance

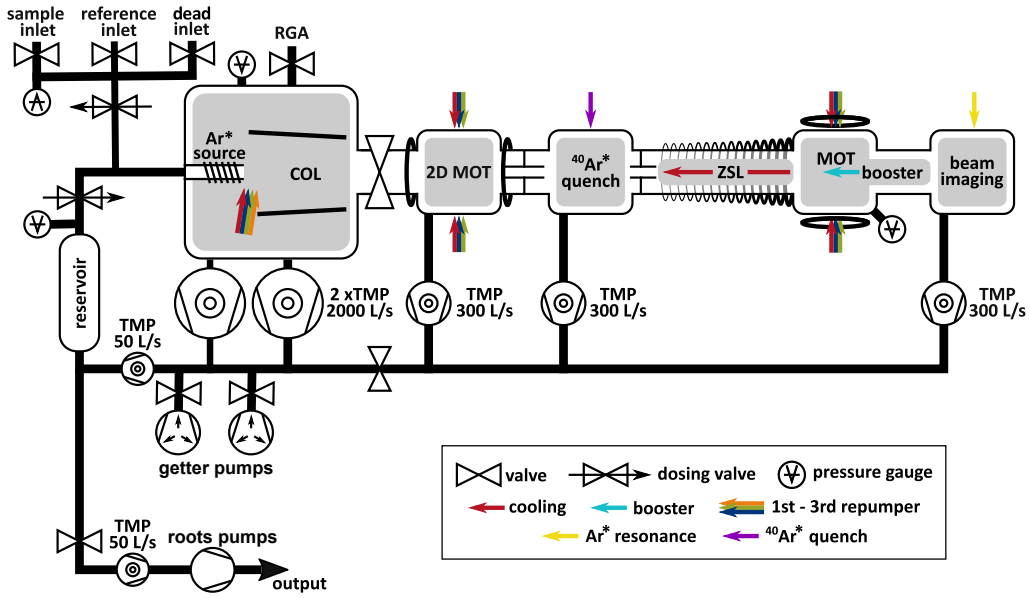

Figure 4.3: Schematic overview of the ATTA apparatus. In the top left, the inlets for aliquots of reference, blank, and sample gas are seen. From here the gas enters the system and ends up in the reservoir. With the subsequent dosage valve, the working pressure can be controlled. From the reservoir, the gas enters the metastable Ar plasma source. To ensure a high pressure gradient between the source and MOT chamber, several turbo-molecular pumps (TMPs) pump the system. The transverse cooling stage of the collimator (Col) and the subsequent focusing unit, the 2D MOT are indicated, as well as the following ^{40}Ar Quench. In the Zeeman-slower (ZSL), the atoms are longitudinally slowed before entering the magneto-optical trap (MOT), where the atoms are trapped and detected via their fluorescence. The last vacuum chamber is for beam alignment. All gas is directed back to the reservoir and re-enters the system. Figure adapted from Robertz (2023).

around 150 MHz, where it is therefore operated. A VCO with a Mini-Circuits ZHL-100W-S+ amplifier supplies the strong rf-signal which is impedance matched with a MFJ VHF matching box.
As the atoms are meant to be trapped within the apparatus, lower velocities are desirable. Therefore, the source is cooled by liquid nitrogen, thus shifting the velocity distribution towards smaller values. The currently installed source is displayed in figure 4.4 where the metal cup through which the liquid nitrogen flows can be seen. Due to the throughflow this source design consumes comparably large amounts of liquid nitrogen, however, a new design by Robertz (2023) has not yet been fully optimized and therefore not yet implemented in the ATTA 1 measurement setup. Robertz (2023) also conducted a quantitative analysis of the rf-source and interested readers are pointed to this work.
Generally, the plasma discharge source is still the part of the ATTA apparatus that has the highest potential for optimization. With an excitation efficiency to the right metastable level of roughly 10^{-3} (Ritterbusch, 2013) it holds great potential for further improvements and, therefore, increase of the countrates.

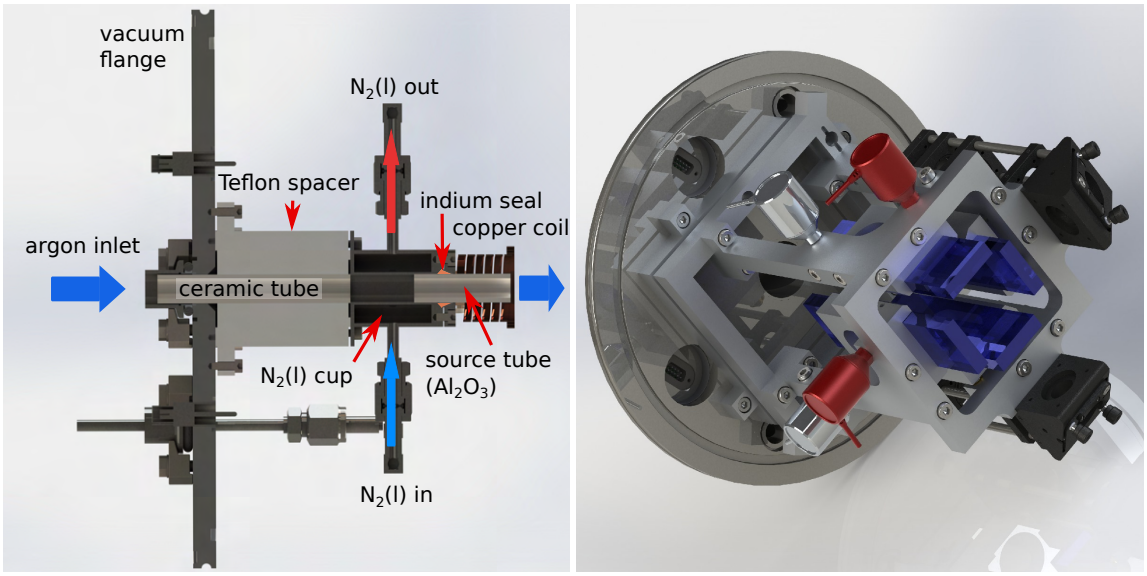

a) b)

Figure 4.4: a) Illustration of the rf-plasma-source. The antenna is made of 1 mm x 4 mm flat copper wire with capton coating and held in place by Rescor 914 holders. In the middle of the coil, the Al_2O_3 source tube is visible, through which the Ar enters the vacuum system. The indicated stainless steel cup is continuously cooled by liquid nitrogen and thermally coupled to the tube by a layer of indium. **b)** The collimator was originally designed by Ritterbusch (2009) and a wider version was implemented by Feng (2019) and is now installed in the ATTA 1 apparatus. The laser light enters through the vacuum fiber connectors and is shaped into an elongated rectangular sheet of light. The 45° mirrors guide the light onto the two pairs of opposing collimator mirrors (in blue), where it is reflected back and forth until it exits at the back. The angles of one of each pair of mirrors can be adjusted from outside the vacuum, as well as the pointing of the whole cage system. For details see main text. Illustrations taken from Ebser (2018).

Collimator

While most of the other components of the ATTA apparatus are only briefly summarized here, the working principle of the collimator will be discussed in more detail as a significant increase of the ^{39}Ar count rate was achieved during the here presented project by optimizing the position of the collimator (see chapter 5).
The ATTA apparatus is equipped with two stages of transversal cooling. The first and most important one is the collimator. Because the atoms exit the plasma discharge source diffusively, one of the key challenges for the ATTA apparatus is the collimation of the atom beam trajectories within a small enough radius. This is needed for a maximal amount of atoms to make their way to the MOT chamber without hitting the walls and thereby deexciting. The technical details of the collimator and their design are discussed by Ritterbusch (2009), Ritterbusch (2013), and Winkelvoß (2024) and a technical drawing can be found in figure 4.4 b). The collimator consists of

two pairs of 40 mm x 160 mm/150 mm mirrors with reflectivities of >99.6%. A flat, rectangular-shaped atom beam is fed by two 1" mirrors at 45° past the short mirror onto the long mirror side from where it is reflected onto the opposite, short mirror. It is reflected back and forth between the two mirrors, with a changing angle relative to the longitudinal axis of the system before exiting the mirrors at the back (compare figure 4.5). Thus, one laser beam is used to address atoms over an extended region while the changing angle changes its Doppler effect with respect to the atoms and thus its detuning. By doing so, the trajectories of different velocity classes of atoms can step by step (reflection by reflection) be collimated.

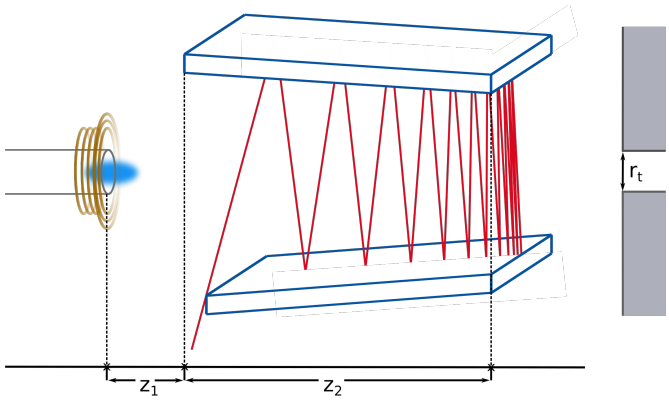

Figure 4.5: Illustration of the plasma source tube with rf-antenna and the collimator mirrors with added indications of the distance between source and collimator, z_1, the length of the collimator z_2, and the radius of the connecting tube to the next vacuum chamber r_t The drawing is not to scale and angles are not the true angles. The laser is added only for visualization and does not depict the true angles and number of reflections.

To understand the limitations of the collimation process, the interplay between maximum radial velocity, maximum longitudinal velocity, and the dimension of the collimator has to be understood. For a constant radial acceleration a, due to the light force within the collimator, the following set of equations for the radial velocity v_r, and longitudinal velocity v_z is derived:

$$(i) \quad v_\mathrm{r} - a \cdot t_2 = 0 \qquad (ii) \quad v_\mathrm{r}(t_1 + t_2) - \frac{1}{2} a t_2^2 = r_t, \tag{4.1}$$

where $t_1 = z_1/v_\mathrm{z}$ and $t_2 = z_2/v_\mathrm{z}$ are the travel times of the atoms from the source to the beginning of the collimator (z_1) and through the length of the collimator (z_2) (compare figure 4.5). The first equation demands the collimation of the atom trajectories (i.e. $v_\mathrm{r} = 0$) within the length of the collimator. The second equation demands the radial spread of the atoms over the distance $z_1 + z_2$ to stay below r_t, in order to pass the subsequent differential pumping stage. Solving these equations derives the maximum radial velocity which can be collimated within a spread of less than r_t, the radius of the subsequent differential pumping stages, and thus can reach

the MOT:

$$v_{\mathrm{rc}} = \frac{\sqrt{2ar_t} \cdot z_2}{\sqrt{z_2^2 + 2z_1 z_2}}; \qquad v_{\mathrm{zc}} = \frac{az_2}{v_{\mathrm{rc}}} = \sqrt{\frac{a}{2r_t}}\sqrt{z_2^2 + 2z_1 z_2}. \tag{4.2}$$

where v_{zc} denotes the corresponding maximum longitudinal velocity. This means that with a higher radial velocity $v_{\mathrm{r}} > v_{\mathrm{rc}}$ the atoms would require a smaller longitudinal velocity than v_{zc} to be collimated, however, meanwhile reaching a larger transverse displacement than r_t. In the case of a larger longitudinal velocity $v_{\mathrm{z}} > v_{\mathrm{zc}}$, the maximum radial velocity which can still be collimated is decreasingly smaller than v_{rc}. The maximum radial velocity which can still be collimated as a function of the longitudinal velocity is obtained by

$$v_{\mathrm{rmax}}(v_{\mathrm{z}}) = \begin{cases} \sqrt{2ar_t + \frac{a^2 z_1^2}{v_{\mathrm{z}}^2} - \frac{az_1}{v_{\mathrm{z}}}}, & v_{\mathrm{z}} \leq v_{\mathrm{zc}} \\ \frac{az_2}{v_{\mathrm{z}}}, & v_{\mathrm{z}} > v_{\mathrm{zc}} \end{cases}. \tag{4.3}$$

The collimator receives light addressing the cooling transition of the atoms as well as three repumper frequencies. The repumper frequencies are needed firstly, to pump the atoms coming from the source to the correct hyperfine state and secondly, to pump them back to this hyperfine state once they are lost due to off-resonant excitation into the wrong excited hyperfine state (compare section 2.2).
All in all, the collimator increases ^{38}Ar loading rates and ^{39}Ar count rates by a factor of about 120 and is therefore a critical element of the apparatus.

2D MOT

After the atoms have made their way through the connecting tube from the source chamber into the 2D-MOT chamber, a second transversal cooling stage focuses their trajectories toward the MOT. This is realized by a 2D MOT, which is often referred to as a magneto-optical lens (MOL). In combination with a magnetic field from two coils in an anti-Helmholtz configuration, two pairs of counterpropagating laser beams exert a force on the atom beam, further collimating and even focusing it. The slight red detuning of the laser frequencies (same detuning as in the 3D-MOT) introduces a transversal-velocity dependence of the light force, while the inhomogeneous magnetic field adds a radial spatial dependence (compare the introduction to magneto-optical traps in section 2.5.2). The 2D-MOT receives the same frequencies as the 3D-MOT, including two repumper frequencies, preventing the atoms from being lost to the wrong hyperfine states.

^{40}Ar Quench

As the vast majority of the Ar entering the system is made up of ^{40}Ar (>99.6% for atmospheric composition, IAEA, a) and as the ^{40}Ar transition is only 492 MHz away from the ^{39}Ar transition there is a significant background of non-resonant light scattered by ^{40}Ar present in the MOT chamber during a measurement. Therefore,

to obtain better signal-to-noise ratios for single-atom detection it is desirable to suppress the scattering of ^{40}Ar. The quench laser at a wavelength of 801.699 nm is tuned in such a way that it excites ^{40}Ar to another excited state from which the atoms can deexcite into the ground state (compare section 2.2 and figure 2.2).
Additionally, the fluorescence signal from the 843 nm light which is emitted upon the deexcitation into the ground state can be used as an absolute atom flux measurement. In contrast to fluorescence detected from a cycling transition, there is a one-to-one correspondence of emitted 843 nm photons and the number of deexcited atoms. For more details, please refer to Robertz (2023), who refined this absolute flux measurement tool.

Zeeman Slower and Booster

So far, the atom beam has been cooled transversally only. However, to trap the atoms in the MOT the longitudinal velocity has to be decreased substantially. For this purpose, a 1.8 m long Zeeman slower (ZSL) is connected to the far side of the quench chamber. It exhibits a long magnetic coil with an increasing number of windings towards the MOT chamber, which creates an increasing magnetic field. Together with a laser with a frequency detuning of about -750 MHz compared to the cooling transition (compare section 4.4), this slower addresses atoms with velocities up to 600 m/s and slows them down to about 60 m/s (details on the ZSL design can be found in Welte, 2011; Feng, 2019). The increasing magnetic field is needed to counteract the decreasing Doppler effect upon deceleration which would cause the atoms to fall out of resonance with the ZSL laser (compare section 2.4).
With decreasing longitudinal velocities two effects come into play. First, transversal heating takes place due to the scattering events in the ZSL. Second, the original and also the now gained transversal velocities increasingly widen the atomic beam with decreasing longitudinal velocities, as the flight time per length increases. Therefore, to prevent a large spread of the atom beam in the last part of the ZSL it is purposefully designed such that a second slowing stage is needed for further deceleration. This is achieved with the Booster, which constitutes a second frequency in the ZSL laser and acts as a second ZSL in combination with the magnetic field of the MOT. Thus, the atoms are slowed down in the MOT trapping region where they already experience the trapping force of the MOT beams.

Magneto-Optical Trap

The magneto-optical trap constitutes the measurement chamber of the apparatus. Here, the atoms are trapped by three counterpropagating pairs of laser beams in combination with a magnetic field from two coils in an anti-Helmholtz configuration (see section 2.5). The laser frequencies are set to a detuning of -8 MHz and thus exert a velocity-dependent force on the atoms. In combination with the inhomogeneous magnetic field, which increasingly shifts the energy levels of the atoms due to the Zeeman effect the further they move out of the MOT center, this configuration

traps atoms in a very confined region at its center. Once trapped here, a clear light signal can be detected even from single atoms as they emit photons from the cycling transition. Connected to the MOT chamber are two detection devices. A CCD camera is mainly employed for the loading rate measurements and the optimization of the MOT and an avalanche photodiode (APD) which is used for the ^{39}Ar detection (for details see Ritterbusch, 2013 and for the exact detection mechanism see Ebser, 2018).

Beam Imaging

The last chamber of the apparatus is the beam imaging chamber. It serves as a beam diagnostic tool for the visualization of the cross-section of the metastable atom beam (for details, see Ebser, 2012). A sheet of ^{40}Ar resonant light is directed through the atom beam with a 45° angle with respect to the longitudinal axis. By looking at the flouresence of the atom beam in this sheet of light the atom beam density can be visualized with a camera. This tool helps to aim the atom beam through the center of the apparatus thus optimizing the balance and angles of the collimator cage and the 2D-MOT beams. As it detects the fluorescence of a cycling transition, it does not provide a reliable signal of the absolute number of metastable atoms in the beam. Slower atoms take longer to transverse the sheet of light and therefore scatter more light resulting in a larger signal. Furthermore, the beam imaging so far only provides a good signal for ^{40}Ar. However, due to the high density of this isotope in the atom beam, it changes e.g. the absorption of light inside the collimator, thus changing its collimation effect. It should therefore not be employed for the optimization of the angle of the collimator mirrors.

4.4 Laser Setup

The laser setup for the ATTA apparatus has to fulfill several demands. It has to provide ten different frequencies with the required power for the experiment. Furthermore, it has to run stably over many days and it has to offer a flexible frequency locking which is needed to switch between the trapping of different isotopes. Therefore, a system is adopted which consists of a reference laser, locked to an Ar spectroscopy cell, and several offset lasers which are offset locked to the reference laser. Furthermore, the quench laser with a frequency 10 nm away from the other lasers has its own spectroscopy locking. All lasers are external cavity diode lasers (ECDLs, Ricci et al., 1995; Hawthorn et al., 2001) from Toptica: three *Toptica DL Pro* and one *Toptica TA100* with an integrated amplifier. The reference laser is locked by saturated absorption spectroscopy in a glass cell with meta-stable ^{40}Ar to the cooling transition $4s[3/2]_2 \rightarrow 4p[5/2]_3$ at 811.754 nm. The quench laser is locked to the transition $4s[3/2]_2 \rightarrow 4p[5/2]_2$ at 801.699 nm. Figure 4.6 gives an overview of the laser system and the important frequencies.
The offset lasers are locked with frequency offset locks (beat locks) to a frequency relative to the reference laser. The functionality and setup of those is discussed

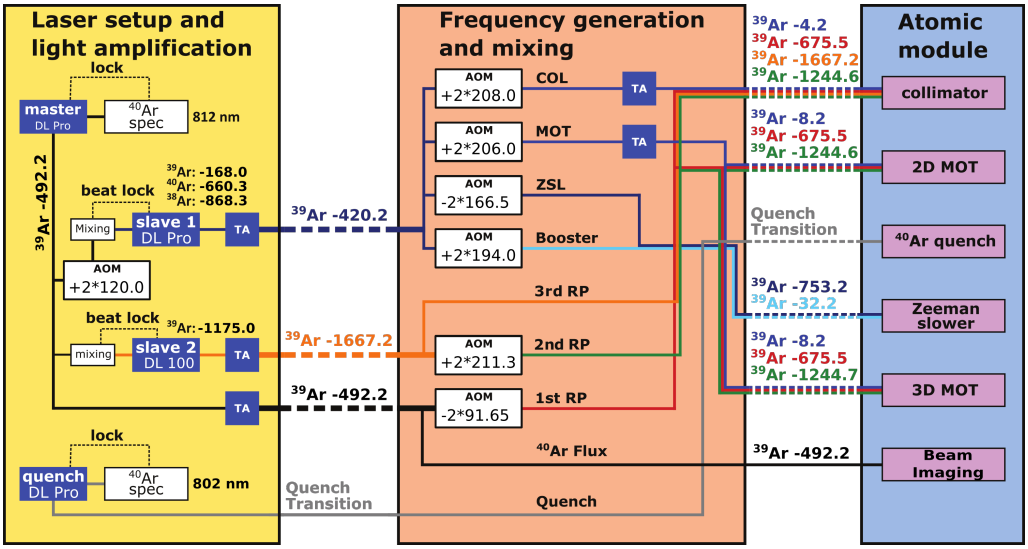

Figure 4.6: Overview of the current laser system in the ATTA 1 lab. On the left side, the laser light generation, locking, and amplification are depicted. In the middle, the frequency shifting with AOMs and mixing is shown. Which frequencies are used for which atomic module is displayed on the right-hand side. Frequencies are given as the ^{39}Ar cooling resonance ± a certain detuning in MHz. Design adapted from Ringena (2021). A more detailed scheme of the optical table can be found in figure 5.6.

in detail in Trautmann (2011) and Kundy (2023). The signal for the offset lock is obtained by overlaying the corresponding offset laser with the reference laser and monitoring the signal on a photodiode. Thus, a beat signal proportional to the relative frequency difference of the two lasers is created and with the help of some electronics can then be used for the locking of the reference laser to a specific relative frequency shift with a PI controller. This kind of frequency locking of the offset lasers allows for very flexible adjustments of the frequency and is therefore very suitable for the fast switching between isotopes.
The first offset laser is used to generate the cooling light for the collimator, 2D- and 3D-MOT as well as the ZSL and Booster laser and is therefore referred to as the *cooler laser*. A second offset laser, referred to as *repumper (RP) laser*, is necessary, as the frequencies of the 2nd and 3rd repumper require a larger shift. Lastly, the reference laser itself is employed to generate the frequency for the first repumper frequency.
Besides the requirement for different frequencies and flexibility in locking them, an important specification of the laser setup is the minimum amount of laser power it needs to provide. With DL pros at 812 nm typically providing around 50-80 mW of laser power with an anti-reflection coated diode and around 100-150 mW for Fabry-Perot diodes, this is by far not enough to meet the required laser powers. Therefore, power amplification by tapered amplifier (TA) diodes is employed. These are semiconductor laser diodes with a tapered gain profile (the model used is *Eagleyard EYP-TPA-0808-02000-4006-CMT04-0000*) which achieve an amplification to more than 1 W from a seed power of about 12 mW. To ensure a stable operation, the TA

setups need to very precisely couple the seed light into the chip and the amplified light into the next fiber. The employed setup was designed in this group and is extensively discussed in Nicolai (2017). In total, five TAs are used in the laser setup. One for each laser, except the quench laser, and additionally for the subsequent amplification for the collimator and MOT cooler light.
So far, the discussed components can be found in the left box of figure 4.6, and the underlying laser light and the necessary power have been generated, now the exact frequencies for each component of the ATTA apparatus come into play. As the ATTA method needs frequencies adjusted to the respective atom velocity and thus Doppler shift in each component, acousto-optical modulators (AOMs) are used to shift the laser frequencies by several hundred MHz. The employed AOMs are mostly *Gooch & Housego, 3200-124* and *3080-125*. The middle part of figure 4.6 displays the exact rf-frequencies applied to the AOMs. Recently, the AOM model *Gooch & Housego, 3200-125* has been tested and provides much better efficiencies (up to 90% double pass efficiency vs. formerly about 50%) and will be incorporated in the new setup of the ATTA 2 lab.
The final step the laser setup has to fulfill is the mixing of the different frequencies into optical fibers, directing the light to each component of the apparatus. This can be seen in the right part of figure 4.6. In total eight fibers direct up to 4 frequencies per fiber to the vacuum apparatus[1]. The general principle of the frequency mixing is based on polarizing beam cubes in combination with $\lambda/2$-waveplates. This setup enables the overlapping of two beams per cube with the option of flexibly adjusting the splitting ratio between the two light paths by turning the $\lambda/2$-waveplate. The whole setup is optimized in such a way that only for the spatial overlapping of the ZSL and Booster light, half of the power is lost. There has been an effort to overcome this waste of light power (Winkelvoß, 2021), however, it has not yet been implemented in the ATTA 1 lab.

4.5 Measurement Routine

A routine measurement with the ATTA apparatus takes 20 hours. With the current count rates of 5-6 ^{39}Ar atoms/h this amounts to around 100-120 atoms measured for an atmospheric sample. The underlying Poissonian statistics, thus, yield a statistical error of roughly 10 %.
Reference measurements are conducted before and after each sample measurement to determine the current performance of the apparatus, which is later used to calculate the ^{39}Ar abundance in the sample. A sample with about 10 times the atmospheric ^{39}Ar abundance is used to detect an equal amount of atoms in 2 h measurement time as an atmospheric measurement would detect in 20 h.
Besides the sample and reference measurements, blank measurements (referred to as *dead sample*) are conducted with gas from a sample with an ^{39}Ar abundance

[1]The MOT fiber is later split up into three fibers on a fiber bench 1:3 splitter. The discarded power from the polarization cleaning is used to monitor the frequencies and relative powers on a Fabry-Perot interferometer.

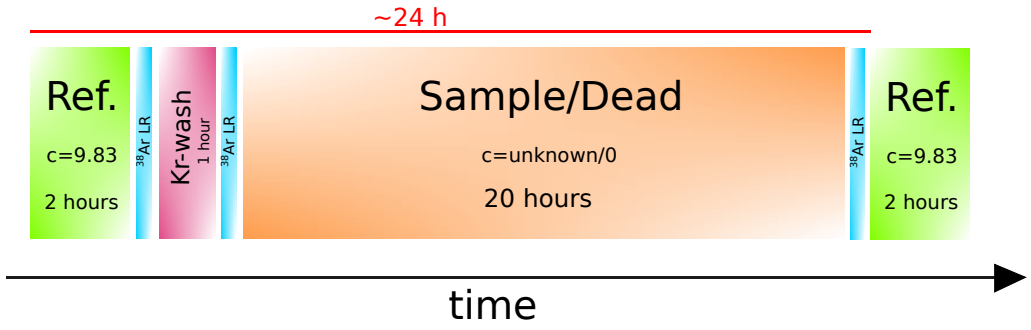

Figure 4.7: The routine measurement cycle over 24 hours. Samples are measured for 20 h. Reference measurements are done with ≈10 times atmospheric ^{39}Ar abundance. In order to prevent any cross-sample contamination (e.g. from gas frozen onto the cold source), the system is flushed by igniting a Kr discharge and warming up the source. ^{38}Ar loading rate measurements are conducted before and after each measurement to monitor the stability of the system. Blank (dead) samples (^{39}Ar abundance $<$ 0.65pmAr, Xu et al., 2015) are measured every other week to monitor the contamination acceleration (compare section 4.6). Figure adapted from Meienburg (2022).

of $<$ 0.65 pmAr (Xu et al., 2015). They are essential, as the sample gas is circling through the apparatus for 20 h in a recycling mode such that any contamination stays in the system and accumulates. The vacuum system is thoroughly leak tested and seeping in atmospheric air does not pose a problem. Furthermore, by Kr flushing the system before each measurement and simultaneously warming up the source to melt off any residues, direct cross-sample contamination does not play a significant role (compare Ebser (2018), who did a detailed analysis of contamination pathways). What plays a major role and requires a thorough characterization through blank measurements is the outgassing of Ar from the walls. Due to ionization and acceleration of the sample gas by the plasma discharge, Ar atoms from each measurement are implanted into the walls and are slowly released during the subsequent measurements. The effect is reduced by the Kr flushing but cannot be completely suppressed. Therefore, a linear build-up of the ^{39}Ar abundance can be observed over time, leading to a quadratic increase of the counted atoms. To quantify this contamination pathway and to incorporate it into the analysis the blank measurements are essential. In a normal measurement routine, the background is stable, and therefore blank measurements can be averaged over longer periods.
Another effect of the increasing contamination over time is the limited sample measurement time. After about 20 h, the counts of outgassed ^{39}Ar atoms are in the order of the counts of the sample gas, so that a longer measurement of the sample does not significantly reduce the error of the measurement. Therefore, if the sample size allows, repeated measurements of a sample are more beneficial to increase precision than extended measurement times.

4.5.1 Loading Rate Measurements

The optimization of the ATTA apparatus and the monitoring of its performance are crucial steps for a high-quality, stable long-term measurement operation. However, the sparseness of the ^{39}Ar isotope poses a fundamental problem. In order to check if all lasers work correctly and if all components are aligned optimally, the best way would be to quickly check the count rate of ^{39}Ar and optimize it. However, with currently about 6 ^{39}Ar atoms/h, the signal is too low for a direct optimization. Furthermore, enriched samples, which would provide a direct measurable ^{39}Ar trapping rate in the MOT, and thus an overall performance check of the apparatus, would immediately contaminate the vacuum system due to the ionization and implantation in the source. Therefore, as the next best solution other isotopes can be continuously trapped in the MOT and thus provide a direct signal, which can be used for optimization. While ^{40}Ar is far too abundant and immediately saturates the MOT, the two less abundant isotopes ^{36}Ar and ^{38}Ar can be employed. There is, however, a fundamental reason why they behave differently than ^{39}Ar and therefore should still be considered with caution. As ^{36}Ar and ^{38}Ar do not exhibit a nuclear spin, they do not undergo hyperfine splitting. This reduces the forces acting on ^{39}Ar in the MOL and MOT compared to ^{36}Ar and ^{38}Ar. Furthermore, as the repumper (RP) frequencies are necessary only for the repumping of the different hyperfine levels, they do not impact the even-numbered isotopes. Thus, the functioning of the RPs can not be checked by trapping them. In lack of a better tool, the loading rate of ^{38}Ar (being even less abundant than ^{36}Ar) is nevertheless employed for the optimization of the different components as well as for frequent stability checks of the system.
The loading rate in the context of the Heidelberg ATTA lab has been discussed before in Ritterbusch (2013), Ringena (2021), and Robertz (2023) and will only briefly be introduced here. It has, however, only recently been incorporated into the daily routine as the main tool for final optimization and stability monitoring. Before, the ^{40}Ar beam imaging served the same purpose, but recent tests have shown that the high abundance of ^{40}Ar leads to light absorption in the collimator and thus biasing its alignment (Robertz, 2023).
The underlying idea of a loading rate measurement is the loading time-resolved monitoring of the number of trapped atoms in a MOT. First, all MOT lasers are shuttered to empty the trap. Then, the lasers are switched on and atoms are loaded into the trap for a certain time, before a fluorescence image is taken of the atom cloud, yielding a signal proportional to the total atom number in the trap. Then the process starts over again. By varying the trapping time, the slope of trapped atoms per time can be swept, ranging from a first linear dependence to saturation. The optimization of certain components then aims at steepening the linear part of the slope of the total trapped atom number vs. loading time.
The loading rate is measured daily for a defined set of components. First, only the flux from the source into the MOT is measured. Second, each collimator axis is switched on individually and its enhancement of the loading rate is measured. Third, both collimator axes are switched on simultaneously and the resulting loading rate is measured. Finally, both axes of the MOL are switched on to give the final loading

rate measurement. While it is desirable to sweep the whole loading rate slope for each measurement and obtain its slope by a fit, as of yet a loading time well in the linear loading regime is taken and only one point of the slope is measured to determine its slope. The set of five loading rate values (source flux, Col1, Col2, Col, Col+MOL) is noted down before and after each measurement and serves as a performance check of the whole apparatus (also compare the measurement cycle in figure 4.7).
Beam imaging which was used for the same purpose in earlier years, is now only employed to optimize the pointing of the whole collimator cage with the external actuators and the two MOL axes, which is only part of larger optimization efforts after a longer standstill.

4.6 Analysis of Measurement Data

A first approach to the analysis of the sample measurements was done by Ebser (2018) and implemented as analysis software by Schmidt (2021). This approach will in the following be called the *old analysis*. It uses the model for the concentration of the sample over time of

$$c(t_s) = c_{\text{sample}} + c_{\text{cross}} \frac{V_{\text{cross}}}{V_{\text{sample}}} + \frac{a}{V_{\text{sample}}} \cdot t_s, \tag{4.4}$$

where c_{sample} is the original ^{39}Ar concentration in the sample gas, c_{cross} the concentration in any gas remaining in the system, V_{cross}, V_{sample} the volumes of the remaining gas of the previous sample in the system and the sample, respectively, and t_s the time since the ignition of the discharge source. a is the contamination acceleration due to outgassing of the walls in $[\mu\text{L STP c}_0\,\text{h}^{-1}]$[2], which is a measure of the accumulation rate of non-sample ^{39}Ar in the system. Integrating this over time gives the total number of atoms after measurement time T as:

$$N(T) = \left[\left(c_{\text{sample}} + \underbrace{c_{\text{cross}} \cdot \frac{V_{\text{cross}}}{V_{\text{sample}}}}_{\approx 0} \right) \cdot \underbrace{(t_s - t_0)}_{:=T} + \frac{1}{2} \cdot \frac{a}{V_{\text{sample}}} \cdot \underbrace{(t_s^2 - t_0^2)}_{:=T^2} \right] \cdot \nu_0, \tag{4.5}$$

where t_0 is the time offset between the start of the source and the start of the measurement, and ν_0 the reference countrate in [^{39}Ar atoms/h]. This means that with a contamination acceleration a determined from blank measurements and a reference countrate ν_0 from reference measurements, the ^{39}Ar concentration in the sample c_{sample} can be obtained. In the analysis proposed by Ebser (2018), because of the Poisson distribution of the number of detected atoms in all measurements, by using Monte Carlo methods, also a, ν_0, and c are distributions from which the median μ and the uncertainties $\pm1\sigma$, $\pm2\sigma$, and $\pm3\sigma$ are calculated.

[2]STP stand for *standard temperature and pressure*, c_0 denotes a reference concentration, usually the atmospheric concentration c_{atm} is used.

The combination of two or more measurements in this analysis is done with point-wise multiplication of the respective probability density functions (PDFs). Kindermann (2024) did a detailed analysis of the general approach of this old analysis and in particular of the way measurements were combined. He was able to show that a general problem arises as the resulting PDF of any combination will always be narrower i.e. better constrained than a single measurement. In a perfect world, this would be true, however, the analysis should not only incorporate statistical uncertainties but also the possible performance drifts of the apparatus. In this old analysis approach, this is entirely neglected.

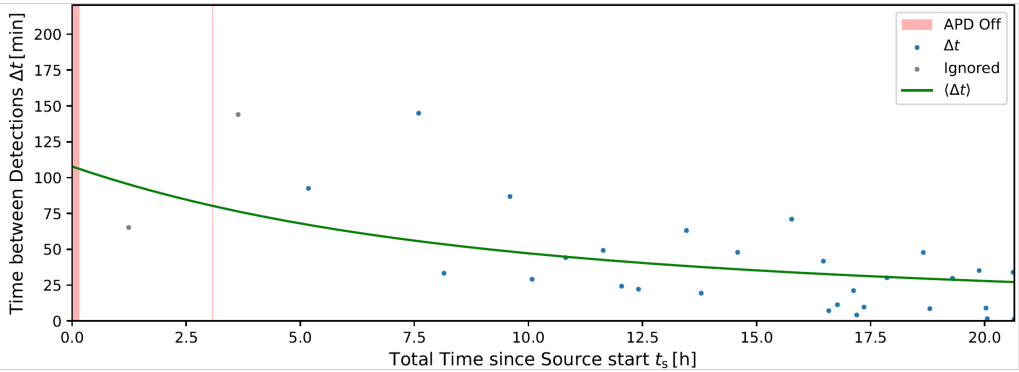

Figure 4.8: New analysis approach: the time between atom events Δt is fitted by a model, thus determining the desired parameters. Figure from Kindermann (2024).

Kindermann (2024) therefore developed a new analysis approach (in the following referred to as *new analysis*). In contrast to the old approach, it is not based on the total number of atoms after time T, but on the time intervals Δt between atom events. The underlying process is Poissonian and therefore the probability distribution for the times between events given by

$$p(\Delta t) = \exp\left(r \cdot \Delta t\right) \tag{4.6}$$

where r denotes the mean frequency of events. It becomes complicated with r not being constant but depending non-linearly on the contamination acceleration. Kindermann (2024) derived a new model, incorporating all these factors (see sections 4.1 and 4.2 of Kindermann, 2024). A function was derived that can be fitted to the Δt values of a measurement over time as displayed in figure 4.8. Due to the complexity of the derivation and the resulting model, please refer to the original work for details.
The new approach comes with several improvements. The times between atoms are independent of each other and can be described by the underlying statistics (see equation 4.6). Furthermore, the combination of several measurements is now possible by shifting the Δt from any measurement to a standard count rate, standard volume, and standard contamination acceleration thus directly combining and fitting the data together. By simulating perfectly statistically distributed Δt for a measurement and comparing them with the measured data, it can also be evaluated if the measurement

ran smoothly and the data sits within a statistically explainable regime, or if indications for performance drifts or jumps during a measurement are present.
One shortcoming so far, however, is that due to the additive combination of the probability distributions of the reference measurements, the uncertainties do not automatically decrease anymore. This might be good for a drifting performance, but in contrast to the old method, uncertainties can only ever increase. Even with a perfectly stable performance over several measurements, the uncertainties of the combined measurements will never decrease below the uncertainties of a single measurement. This means that errors are overestimated, which is certainly better than underestimating them but not yet fully satisfactory.
After the development of the new approach, a user-friendly interface for the routine analysis of measurement data is on the way. All measured data in this thesis is evaluated with the beta version of the new analysis approach.

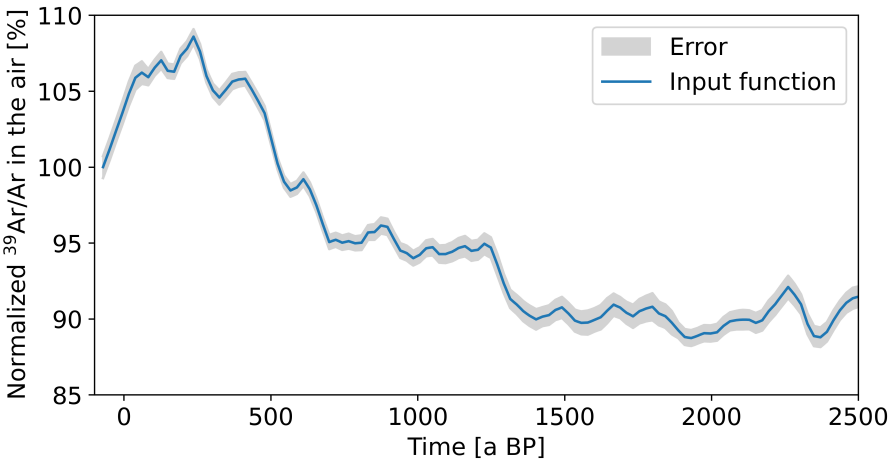

Figure 4.9: ^{39}Ar/Ar ratio in atmospheric air over time normalized to its modern value. Time in years before present (BP), where present refers to the year 1950 CE. The input curve displayed was calculated by Happel (2024), the error is based on the first principle component of the analysis.

Atmospheric Input Function of ^{39}Ar

So far in most analyses of ^{39}Ar samples, the input function of ^{39}Ar in the atmosphere was assumed to be constant. Because the half-life of ^{39}Ar is long enough compared to the time scale of atmospheric mixing processes, a uniform global atmospheric ^{39}Ar concentration can be expected (Lal and Peters, 1967; Loosli, 1983). However, the production rate of ^{39}Ar in the atmosphere is expected to depend on the flux of cosmic rays. First estimates stated a possible variation of up to 7 % of ^{39}Ar abundance in the atmosphere over time (Oeschger et al., 1974; Loosli, 1983) and attempts for the experimental determination of the ^{39}Ar/Ar input history were made via low-level counting (LLC) by Loosli and Oeschger (1968) and Loosli (1983). However, due to the advances in the ATTA method, a more detailed reevaluation was conducted

by Gu et al. (2021) and Happel (2024). Figure 4.9 shows the $^{39}Ar/Ar$ ratio in atmospheric air normalized to its modern value as it was calculated by Happel (2024). The calculation is based on data from Steinhilber et al. (2012) on cosmic radiation and solar activity (see Happel (2024) for details). In this thesis, all ages are corrected for the varying input history.

5 Technical Developments in the ATTA Lab

ATTA has to bridge the gap between two very different challenges. On the one hand, it is established well enough to be routinely applied to environmental samples. With the ATTA lab in Heidelberg currently being one of two labs globally that can measure ^{39}Ar from small samples, large interest from different communities of ocean science, groundwater science, and glaciology leads to a continuous inflow of new samples to be measured. On the other hand, the method still needs substantial development to improve precision, stability, and sample throughput. The demands each of these challenges introduces are quite different, however. For a stable measurement run the vacuum and laser system is best brought into an equilibrium by continuous operation with as little readjustments as possible. For example, the laser system becomes more stable when only small re-optimizations are done over time and the thermal equilibrium is least disturbed by e.g. opening the laser table. Also, the collimators must reach thermal equilibrium with a constantly running plasma discharge. Furthermore, reference and blank measurements are only applicable within a time interval of an unchanged system. In contrast, when focussing on technical improvements, the system often has to undergo larger modifications. This can be anything from testing different source designs (Robertz, 2023; Zehenter, 2024; Junkermann, in progress), to optimizations of the vacuum system (Moraw, 2024; Kindermann, 2024), new designs for the collimator (Winkelvoß, 2024) and readjustments and tests with alternative laser setups (Kundy, 2023), to name a few aspects which were tackled during the time interval of this thesis. Therefore, the priorities of sample measurements always have to be weighed against ideas for technical improvements. The experience of the last years has shown that a quick-shifting between *measurement mode* and more technical tests is rarely as straightforward as it sounds. With these ambiguous demands in mind, the construction of a second ATTA lab was started in 2017 by Feng (2019) and continued by Ringena (2021) and Robertz (2023), however, never reaching reasonable count rates. In 2023, the lab was moved from the initial shipping container into a room adjacent to the original ATTA lab to facilitate the joined work as well as improving the spatial circumstances in the lab (Meienburg, in progress; Junkermann, in progress). The original ATTA lab is in the following referred to as ATTA 1, the new one as ATTA 2.

The work done during this thesis was focussed on the ATTA 1 lab. While in the ATTA 2 lab, mostly general tests e.g. characterizing velocity distributions, different source designs, etc. were conducted, the work in the ATTA 1 lab, led by the author, was focussed on the improvement of the count rate and environmental measurements.

When starting to work on this project, count rates were initially as low as 1.5 ^{39}Ar atoms/h. In 2019, the crash of both turbo-molecular pumps connected to the source chamber destroyed parts of the collimator and source and caused a redesign of the chamber. Afterward, the apparatus had not reached former count rates. Furthermore, the immediately preceding focus had been set on the demonstration of dual-ATTA with ^{85}Kr and ^{39}Ar (Ringena, 2021) including alterations of the laser table so that the ^{39}Ar system was not in optimal condition. Within the first half year, count rates of 3-4 ^{39}Ar atoms/h were reached by aligning the experiment and optimizing the optical components. However, the 6-7 ^{39}Ar atoms/h reported in Ebser (2018) were not yet reached. With a large queue of environmental samples, longer periods of sample measurements were nevertheless conducted (see table A.5), while whenever possible technical improvements and tests were done to enhance the count rate. Only after much invested time into the understanding and optimization of the apparatus, count rates could be increased back up to 6-7 ^{39}Ar atoms/h, and large sample throughputs were reached.

In section 5.1, an overview of the main technical improvements is given. A special focus is set on the adjustments of the collimator, which was the key to reaching higher count rates. Section 5.2 gives an overview of the main technical parameters of the apparatus, which were found to ensure a stable measurement mode with count rates of 6-7 ^{39}Ar atoms/h. In section 5.3, an ongoing project, the setup of an online database for all ATTA measurements is summarized.
Over the several years of supervising the work in the ATTA 1 lab, a multitude of further tests and small technical improvements have been made. As many of them were already discussed in several master and bachelor theses which were supervised in the scope of this work, the thesis at hand will concentrate on the major improvements only. Details on many technical characterization steps of the system and parameter scans of various parts of the apparatus can be found in Meienburg (2022). In Kundy (2023), the effort is reported to check the repumper laser frequencies and to test a first precollimation stage. Schwenzer (2022) reports on the implementation of the updated absolute metastable ^{40}Ar flux measurement in the ATTA 1 lab, based on Robertz (2023). A new collimator design was implemented by Winkelvoß (2024), which is still being tested in the ATTA 2 lab but should soon be implemented for the measurements in ATTA 1 lab as well. Finally, Kindermann (2024) and Moraw (2024) tested a new design for differential pumping stages which would minimize pressure peaks in the system.

5.1 Improvements of the Transversal Cooling

The collimator is one of the crucial elements of the ATTA apparatus. Its collimation of the atom trajectories enhances the flux of Ar atoms to the MOT by a factor of around 100. As introduced in section 4.3, the atoms are diffusively exiting the source and need to be collimated within the radius of the subsequent tubes between the

vacuum chambers to find their way to the MOT. A photo of the ignited plasma source and the mirrors of the collimator is shown in figure 5.1.
When starting in the ATTA lab in 2021, a gap of about 4 cm was present between the end of the source tube and the start of the collimator mirrors, measured along the axis of the apparatus (compare figure 4.5). It is hard to reconstruct the exact reason for the gap, but Ritterbusch (2013) states that in the early 2010s, the optimal source coil design was found to protrude beyond the source tube by 3 cm. Therefore, the gap between the source tube and the collimator mirrors was introduced. In a later effort to enhance the collimation efficiency in the source chamber, Feng et al. (2017) tested a precollimation setup based on bichromatic cooling in the gap between the source tube and collimator. However, presumably due to its proximity to the strong electric fields of the rf-source, the effort did not succeed. The redesign of the source chamber by Schmidt (2021) after the crash in 2019 potentially changed the source-collimator distance again.
Howsoever, the gap of 4 cm between the source tube and collimator was present when this project commenced. In the current design, however, the antenna does not protrude beyond the source tube and the gap is unnecessary.

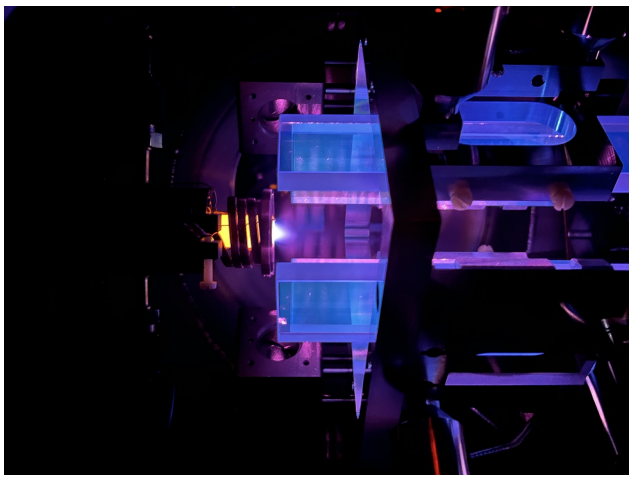

Figure 5.1: Photo of the plasma source and its antenna (left-hand side) and the collimator setup (right-hand side). The mirrors are glowing blueish. The stripes between the mirrors are caused by the atom fluorescence from the laser reflections between the two collimator mirrors. The photo is taken in the current setup with $z_1 = 4\,\mathrm{mm}$. Photo by N. Mandaric.

In section 4.3, the underlying equations for the collimator have been introduced. It is intuitively understood but can also be seen in equation 4.2 that the longer the atoms travel without transversal cooling after exiting the source, the smaller the critical radial velocity can be, which can still be collimated within the radius of the subsequent tubes r_t.
The maximum acceleration of an atom in a light field can be calculated from equation 2.30 and the scattering rate of $\gamma = 5.87\,\mathrm{MHz}$ (Metcalf and van der Straten, 2012) as

$$a_{\mathrm{max}} = \frac{F_{\mathrm{max}}}{m} \approx 2.3 \cdot 10^5\ \mathrm{m/s^2}. \tag{5.1}$$

Figure 5.4 visualizes the solution for the maximum radial velocity v_{rmax} in dependence of the longitudinal velocity v_{z}, given by equation 4.3, with a_{max} as stated and $r_t = 9\,\mathrm{mm}$. It can be seen that for no distance between source and collimator

($z_1 = 0$), all $v_r \leq v_{rc}$ up to the critical longitudinal velocity v_{zc} can be captured by the collimator. With a non-zero distance z_1, atoms with very low v_z spend so much time in the gap that even small radial velocities v_r bring them too far off-axis to be collimated within r_t distance from the center axis. This effect increases for increasing z_1 resulting in less collimated atoms reaching the MOT.
The critical radial velocity, given by equation 4.2, for $z_1 = 40\,\text{mm}$ amounts to about $52\,\text{m/s}$, for $z_1 = 4\,\text{mm}$ it increases to about $63\,\text{m/s}$.

5.1.1 Additional Transverse Cooling Behind the Source

In a first effort to improve the transversal cooling behind the source and to lessen the effect of losing atoms due to the cooling gap before the collimator, a one-dimensional molasses was set up between the source tube and collimator. The work was done together with a master student who conducted a detailed analysis of the precollimation in Kundy (2023).
A supplementary laser system was set up, which allowed free tuning of the laser frequency. From this, a laser beam was widened to about 7 mm beam radius, polarization cleaned, and directed at a 90° angle through a vacuum viewport, crossing the atom beam directly behind the plasma source. Behind the vacuum chamber, it was retro-reflected and directed back through the atom beam, see figure 5.2 for the setup. The power of the setup was controlled by its tapered amplifier.
The characterization of the precollimator was done with ^{38}Ar by looking at its

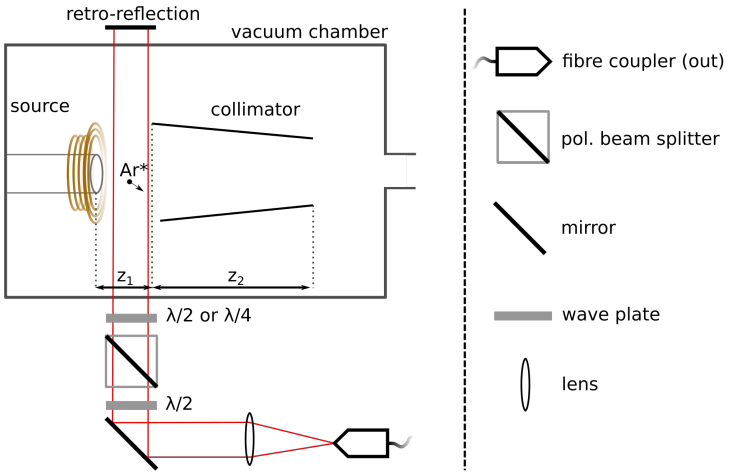

Figure 5.2: Setup of the precollimator optical molasses between source and collimator. A laser beam of about 7 mm beam radius crosses the atom beam and is back-reflected and acts as a one-dimensional optical molasses.

loading rate (LR) in the MOT (compare section 4.5.1). The low isotopic abundance and its complex hyperfine splitting requiring additional laser frequencies make ^{39}Ar not ideal for such a first analysis.

Results

To evaluate the impact of the one-dimensional optical molasses behind the source, the effects of the laser detuning as well as its power on the ^{38}Ar loading rate (LR) are analyzed. Figure 5.3 shows the measurements of the loading rate as a function of the

laser detuning δ_L. The detuning is given with respect to the ^{38}Ar cooling transition, which lies 208.1 MHz away from the ^{40}Ar transition. The two curves show results for two different saturation parameters of $s_0 \approx 114$ and 23, respectively, which were calculated from the laser powers of $P \approx 250$ and 50 mW, the beam radius $r = 7$ mm and the saturation intensity of the transition of $I_s = 14.3\,\mathrm{W/m^2}$ from equation 2.26. The equation applies to circular polarized light only. For linear polarized light, the saturation parameters decrease roughly by a factor of two (Ritterbusch, 2013). The optimal laser detuning δ_L^{opt} was extracted from the data by fitting a Gaussian distribution to it. The results are shown in table 5.1. While the theory does not predict a Gaussian-like dependence it fits well enough to extract the approximate peak value and width from the data. Concerning the optimal laser power, a saturation of the enhancement of the LR was found above a power of 250 mW ($s_0 \approx 114$) (see Kundy, 2023).
An analysis of the polarization dependence was also conducted. The results are shown in figure A.6 and show no significant dependence.
Altogether, with high power and a detuning of -28 MHz a maximal enhancement of the LR by $\approx 35\%$ was measured (compare figure 5.3).

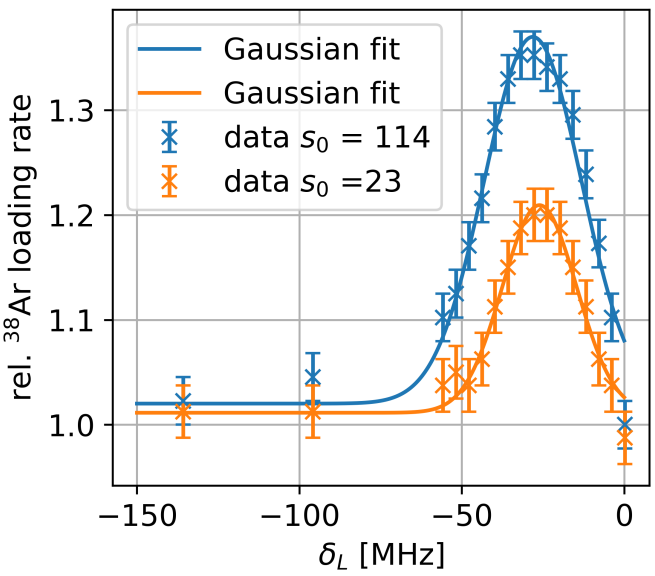

Figure 5.3: The effect of the precollimator: the relative ^{38}Ar LR is measured against the laser detuning δ_L. The saturation parameters $s_0 \approx 114$ and 23 correspond to laser powers of $P \approx 250$ and 50 mW. The fit results of the Gaussian fit can be found in table 5.1. Relative LR errors are estimated to ±0.02. Figure adapted from Kundy (2023).

Table 5.1: Fit results from the Gaussian fits to the data shown in figure 5.3.

fit parameter	for $s_0 = 114$	for $s_0 = 23$
δ_L^{opt} [MHz]	-28.1±0.6	-26.1±0.9
σ [MHz]	15.0±0.8	11.4±1.1

Discussion

The loading rate increase of about 35% is a significant enhancement of the metastable atom flux to the MOT. However, as it has only been tested with ^{38}Ar the question

remains how to transfer this increase to the more challenging ^{39}Ar isotope. First, the effect of the additional optical molasses can be understood when looking at figure 5.4. In the discussed setting, the blue line for $v_{\mathrm{rmax}}(v_{\mathrm{z}})$ is valid with $z_1 = 40\,\mathrm{mm}$. It is apparent that atoms with low longitudinal velocities v_{z} and higher radial velocities v_{r} cannot be collimated by the collimator.
With a saturation parameter of $s_0 = 114$ in the optical molasses, the resulting power broadening of the line width is $\gamma' = \gamma\sqrt{1+s_0} = 63\,\mathrm{MHz}$ (Metcalf and van der Straten, 1999). Therefore, in a simple approach, with a detuning of -28 MHz and such a large linewidth the laser can be assumed to be in resonance with all atoms with a Doppler detuning between -59 and 3 MHz, corresponding to 48 to -2 m/s transversal velocity, with the velocity being positive in the direction towards the laser beam. In a simplified calculation, neglecting the Gaussian intensity profile of the precollimator laser and assuming that all atoms are in resonance with the laser at all times, a beam diameter of $d_{\mathrm{beam}} = 14\,\mathrm{mm}$ would thus increase the length of the transversal cooling stage by 14 mm, however still leaving 26 mm of the initial gap. The red dash-dotted line in figure 5.4 shows $v_{\mathrm{rmax}}(v_{\mathrm{z}})$ for $z_1 = 0.26\,\mathrm{mm}$ and $z_2 = 174\,\mathrm{mm}$.
If this setup was to be introduced as a permanent feature, it would certainly involve a second axis. While the enhancement factors of the two dimensions could be expected to multiply and therefore lead to a loading rate increase by a factor of $1.35^2 \approx 1.8$, the implementation would be more difficult. The implemented axis simply used existing viewports of the vacuum chamber for the feed through of the laser light, while the additional axis at 90° to the other one is blocked by the two attached turbo-molecular pumps. This could of course be achieved with an appropriate optical setup. However, a second requirement for the proper enhancement also of the ^{39}Ar collimation would be the addition of repumper frequencies to the optical molasses. As discussed in section 2.2, ^{39}Ar has a non-zero nuclear spin leading to a hyperfine splitting of its energy levels and for two reasons additional repumper frequencies are needed. First, the atoms can be assumed to be evenly distributed over the hyperfine levels of the metastable state after exiting the source, thus, in order to maximize the number of ^{39}Ar atoms in the correct hyperfine state for transversal and longitudinal cooling, the atoms in the 'wrong' hyperfine states have to be pumped to the 'correct' one. Second, to counteract off-resonant excitation by the cooling transition to other hyperfine states of the excited state and a subsequent loss to the wrong hyperfine state of the metastable state, these repumper frequencies are required throughout the transversal cooling stages of the apparatus. For both reasons, the optical molasses would need three additional repumper frequencies as indicated in figure 2.2 (the fourth one is omitted in the experiment as it contributes only very weakly).

5.1.2 Decreasing the Source-Collimator Distance

In an effort to implement the obvious benefits from transversal cooling directly behind the source but minimizing the addition of further optical components (which increases the maintenance workload and decreases stability) another approach was taken. By

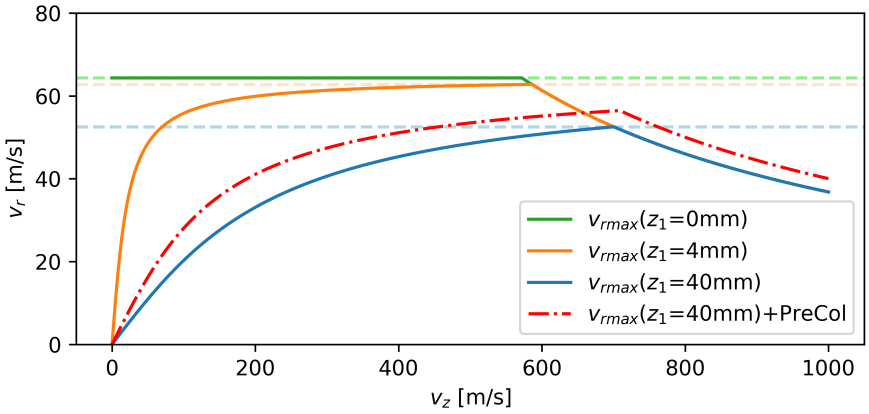

Figure 5.4: Visualization of $v_{\mathrm{rmax}}(v_{\mathrm{z}})$ given by equation 4.3 for $a_{\mathrm{max}} = 2.3 \cdot 10^5\,\mathrm{m/s^2}$ and $r_t = 9\,\mathrm{mm}$. Solid lines show $v_{\mathrm{rmax}}(v_{\mathrm{z}})$ for different z_1. Dashed lines indicate the corresponding critical radial velocity v_{rc} (see equation 4.2). The red dash-dotted line shows the radial velocity capture range with the additional precollimator with a power-broadened line width and assuming perfect cooling in the optical molasses, see main text. The increasing behavior in the left part of the functions stems from $z_1 \neq 0$ and the resulting drift of the atoms too far off axis for too low v_z in the gap (therefore not seen for $v_{\mathrm{rmax}}(z_1 = 0)$). The decreasing behavior on the right can be understood as a too short time the atoms spend in the collimator due to high v_z and, thus, a reduced collimation effect with increasing v_z.

moving the collimator closer to the source, the length of the transversal cooling region is not increased, however, the effect of the spread of the atom trajectories in the gap behind the source is decreased. In figure 5.4 the green line shows v_{rmax} for a collimator located directly behind the source (i.e. $z_1 = 0$). The increase of this maximal radial velocity which is captured by the collimator is apparent. Especially, the longitudinally slow atoms are collimated to a much greater extent. In the lab, a source-collimator distance of $\approx$4 mm was achieved, limited by the clipping of the collimator laser on the source antenna. The orange line in figure 5.4 shows $v_{\mathrm{rmax}}(v_{\mathrm{z}})$ for this distance.
So far in the compilation of figure 5.4 the maximum force and thus deceleration as given by 5.1 was considered. It implies an ideal collimator, which assumes perfect and continuous laser cooling throughout its entire length. Ritterbusch (2013) did a more detailed analysis of the collimation process in a realistic collimator and found that the relation of $v_{\mathrm{rmax}}(v_{\mathrm{z}})$ depicts a realistic scenario when estimating $a = a_{\mathrm{max}}/2$. Furthermore, the real velocity distributions of the atoms have to be incorporated into the calculation. In figure 5.5, the velocity distributions from Feng (2012) are overlaid by $v_{\mathrm{rmax}}(v_{\mathrm{z}})$ from equation 4.3. The velocity distributions were measured with a similar source design to the current one. The longitudinal velocity distribution is given by the 3D-Boltzmann distribution

$$f_{\mathrm{z}}(v_{\mathrm{z}}) = \frac{4}{\sqrt{\pi}} \frac{v_{\mathrm{z}}^2}{\hat{v}^3} \mathrm{e}^{-\frac{v_{\mathrm{z}}^2}{\hat{v}^2}} \tag{5.2}$$

with a most probable velocity of $\hat{v} = 243\,\mathrm{m/s}$. The transversal velocity distribution is given by a Gaussian distribution

$$f_\mathrm{r}(v_\mathrm{r}) = \frac{1}{\sqrt{2\pi}\sigma} \mathrm{e}^{-\frac{(v_\mathrm{r}-\mu)^2}{2\sigma^2}} \tag{5.3}$$

with $\mu = 0$ and $\sigma = 85\,\mathrm{m/s}$ (compare Feng, 2012 and Ritterbusch, 2013). By assuming that the velocity distributions for the transversal and the longitudinal velocity are independent of each other, the total velocity distribution is given by

$$f(v_\mathrm{r}, v_\mathrm{z}) = f_\mathrm{r}(v_\mathrm{r}) \cdot f_\mathrm{z}(v_\mathrm{z}) \tag{5.4}$$

In figure 5.5, it can be seen that a significantly larger part of the velocity distribution can be collimated with a shorter z_1. To calculate the fraction of atoms that can be collimated for each z_1, the integral

$$\int_0^\infty \int_0^{v_\mathrm{rmax}(v_\mathrm{z})} f(v_\mathrm{r}, v_\mathrm{z}) v_\mathrm{r} dv_\mathrm{r} dv_\mathrm{z} \tag{5.5}$$

is calculated numerically (note that the integral is carried out in cylindrical coordinates and therefore requires the factor v_r in the integral). For $z_1 = 40\,\mathrm{mm}$, a value of 6.4% is calculated, for $z_1 = 4\,\mathrm{mm}$ the integral results in 12.2%. This means that by decreasing the source-collimator distance from 40 mm to 4 mm the amount of atoms which should, in theory, be collimated and therefore reach the MOT is increased by a factor of almost 2.

Table 5.2: Values indicating the performance of the ATTA apparatus for $z_1 = 40\,\mathrm{mm}$ and $z_1 = 4\,\mathrm{mm}$. The numbers were averaged over a few measurements prior to and after the decrease of the source-collimator distance and should be viewed qualitatively. A quantitative comparison is complex as many other parameters that probably changed over the 1/2 year gap between the measurements influence the performance. The LR value is measured with an exposure time of 1 ms and a MOT-loading time of 10 ms.

measurement type	$z_1 = 40\,\mathrm{mm}$	$z_1 = 4\,\mathrm{mm}$
^{40}Ar BI [a.u.]	7.5	20.1
^{38}Ar LR [a.u.]	7.6	16.9
^{39}Ar countrate [^{39}Ar atoms/h]	2.8	6.3

The reduction of the source-collimator distance was implemented in April 2023 as a part of larger alterations. The effect was immediately visible in the ^{38}Ar LR, the beam imaging (BI) values, and most importantly, in the ^{39}Ar countrates. Table 5.2 lists values from before and after the reduction of the source-collimator distance. As the gap reduction was implemented towards the end of a longer hardware test sequence in April 2023, there is a time gap of half a year between the last proper sample measurement with $z_1 = 40\,\mathrm{mm}$ and the first with $z_1 = 4\,\mathrm{mm}$. This hampers a direct and quantitative comparison, however, qualitatively spoken, the values of the beam imaging, the loading rate, and the count rate after the alteration were far above

any values measured before. The values shown in table 5.2 are averaged over several (3-5) measurements before and after the distance reduction and are representative of the values obtained for longer periods before and after. It can be seen that the numbers uniformly show an increase of about a factor two (for BI almost a factor three). This corresponds well to the factor predicted by the collimation calculations above.

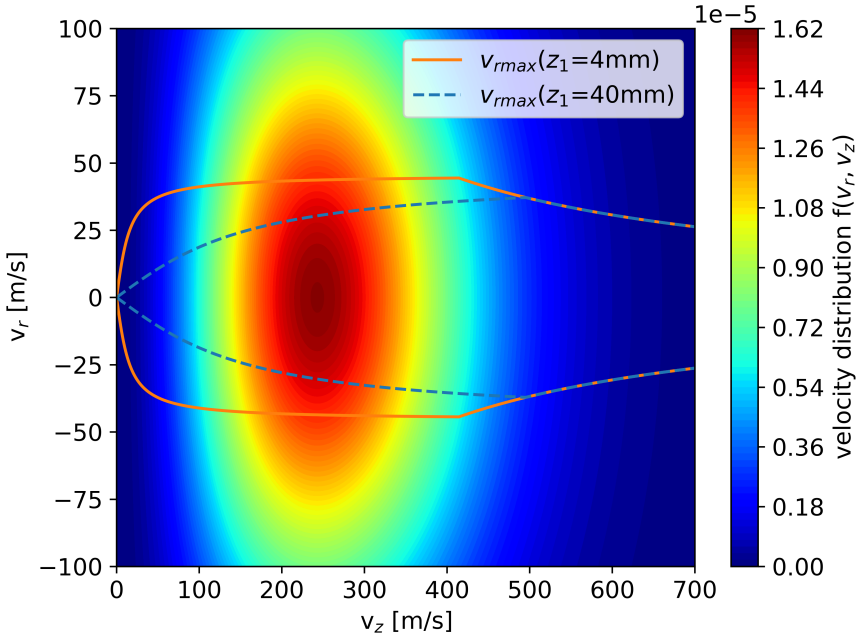

Figure 5.5: $v_{\mathrm{rmax}}(v_{\mathrm{z}})$ for $z_1 = 40\,\mathrm{mm}$ and $z_1 = 4\,\mathrm{mm}$ with $a = a_{\mathrm{max}}/2$ overlaying the velocity distribution $f(v_{\mathrm{r}}, v_{\mathrm{z}})$ (equations 5.2, 5.3, and 5.4 and parameters from Feng, 2012) of the atoms exiting the source (see main text).

By moving the collimator closer to the source, it seems that about the same increase could be achieved as the precollimation with an optical molasses would have promised. However, this way the required repumper frequencies are already implemented and also no additional laser amplifier (TA) is needed. The one drawback that results from the repositioning of the collimator is its greater susceptibility to the temperature fluctuations induced by the rf-source. This problem has always been present and is described in Ebser (2018) already. When first starting the plasma discharge, it takes up to one day for the collimator to reach thermal equilibrium. Due to its cage design and the multiple reflections on its mirrors, it is very susceptible to changes in its geometry in the order of μm. With the reduced source-collimator distance, therefore, the off time of the source has to be minimized between samples as this induces changing temperatures in the collimator. As a result of this increased instability, Winkelvoß (2024) added a screen between the source and collimator to shield any off-axis ions and rf-radiation. Furthermore, a new and less temperature-sensitive design of the collimator was designed and tested in the ATTA 2 apparatus which should soon also be incorporated in the ATTA 1 apparatus (Winkelvoß, 2024). Nev-

ertheless, by paying attention to the thermal equilibrium in the source chamber, a stable measurement operation of the apparatus has so far been running for over a year.

5.2 Key Parameters for Stable Measurements

The ATTA apparatus as a whole is a very complex and delicate setup. While it is therefore always only a matter of time until some part of the large setup does not work up to specifications anymore, for running sample measurements it is crucial to ensure a stable performance of the apparatus. Furthermore, as atom count rates are still the limiting factor of the method, the whole system has to be operated at its limits and therefore every small fault is immediately seen in the count rates. Much time has been invested during this project to better understand and improve the instabilities of the collimator, mainly caused by the thermal gradients induced by the plasma source. Also, the limited laser power has been increased by adding a laser amplifier (TA) for the MOT cooler, thus, leaving more power to other components such as ZSL and Booster. Better temperature stabilization in the laboratory has been implemented with an Arduino-driven PID controller, controlling fan heaters in the lab. Furthermore, the old monitoring system was replaced by a new version, originally constructed by Robertz (2023) and equipped with a new Arduino-driven analog-signal-read-out-box, designed by the author.
One of the large challenges upon entering the lab at the onset of this PhD project was, however, to find the optimal parameters for all the electric, optical, and vacuum parts of the apparatus. Over the course of the last years, for the first time in the Heidelberg ATTA effort, the focus of lab work could, for extended periods of time, be set on conducting measurements of environmental samples instead of mainly working on technical issues. This resulted in long-term measurement campaigns conducted in the lab and thus much experience was gained in which parameters are crucial for good count rates. While the ATTA method is still at a point in its development where only a specifically trained and experienced person can operate it, it is still of great help to have the key parameters written down, which ensure count rates of currently $\sim$6 ^{39}Ar atoms/h over longer periods. In the appendix, several tables list the key parameter values that were aimed for when optimizing the laser setup and other parts before measurements. These values should be treated as an archive for the values used between roughly spring 2023 and summer 2024 when for over a year count rates of about 6 ^{39}Ar atoms/h were reached and more than 100 samples were measured. They are, most likely, not the last word on the subject and should be replaced once better performance is reached. However, with the current setup, they have proven to ensure stable operation. Table A.1 lists all AOM frequencies of the setup, table A.2 the voltage and current of all coils, and table A.3 the power required behind the fibers of each tapered amplifier (TA). Finally, table A.4 lists the lasers powers of all components of the ATTA apparatus.

5.3 Data Base DabATTA

With the progress of recent years, the ATTA method reached a status where it can routinely be applied to many environmental samples. While it is still a large technical effort and requires specifically trained operators, the interest it has sparked in fields such as oceanography, groundwater-hydrology, and glaciology has led to an increasing sample throughput. For a single sample, this means keeping track of the information from sampling, from the gas extraction and Ar purification to the data obtained during the measurement and the subsequent analysis, including reference measurements and blanks. With the two institutes as well as external partners involved and a growing sample number and, thus, the growing number of involved people, the Excel and lab book-based records have proven to become a problem. The last person in the chain doing the analysis needs all previous information and thus needs to sort through all kinds of data sources. This problem has become even more evident when e.g. a reanalysis after considerable time with new data analysis methods was undertaken. To provide a long-term, clear, and well-sorted database for all relevant information a project was started together with the computing division of the KIP (www.dabatta.kip.uni-heidelberg.de). The project in its early stages is portrayed also in Meienburg (2022) but is still in progress and already includes all information up to the measurement of the samples in the ATTA lab. The rewriting of existing code to communicate with the database via APIs (Application Programming Interface) is in the making and soon all data will automatically be uploaded to the database after a measurement. The entire analysis including the selection of reference measurements and blank measurements will also be implemented into the database. The database also includes user management, which enables the administrator to give certain rights to specific users, so that they can only access or write the information relevant for them.

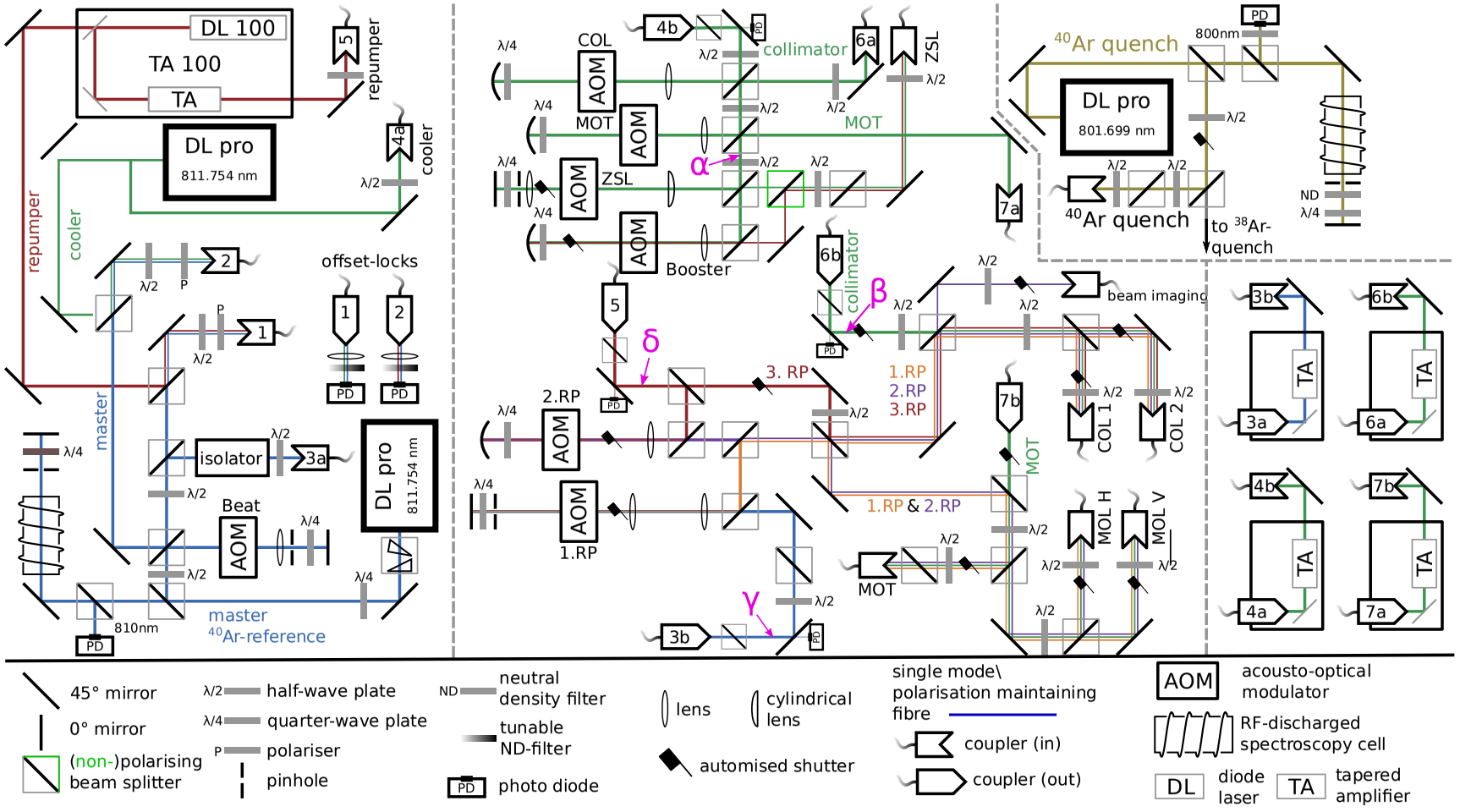

Figure 5.6: Schematic of the current optical setup of the laser table in the ATTA 1 laboratory. In pink, the laser power measurement points relevant for table A.3 are indicated. The position of the TAs is not the actual one on the laser table, due to space constraints. Figure updated to the current setup from Ebser (2018).

6 Diffusion of Argon in Ice

The constraints on the diffusion coefficient of Ar in ice are quite vague and especially experimental evidence is limited to the work by Satoh et al. (1996), who state in their publication to have had difficulties resolving the low value for Ar. Therefore, and to obtain a better understanding of the possibilities of atmospheric contamination by diffusion in long-stored ice samples, in the following an attempt is made to experimentally tie down the diffusivity of Ar in ice based on ^{39}Ar measurements.

6.1 Results of the Diffusion Model

In the following, based on the solution of the diffusion into a cylinder given by equation 3.20, the resulting general concentration profile and its dependence on time (or similarly the diffusion coefficient) is discussed. Hereby, the dimensionless variable $\frac{Dt}{a^2}$ (with D the diffusion coefficient and a the radius) is employed, combining the effects of the time and the diffusion coefficient in a single variable. The work presented here continues the work done in the bachelor thesis of von Reventlow (2022), which was supervised in the scope of this thesis.
In figure 6.1, the concentration profiles of a diffusion process for different times (or diffusion coefficients) are plotted against the dimensionless radius r/a. Each colored curve represents a different Dt/a^2. The resulting mean concentrations which would be measured in such an ice core are indicated in the legend. In the following, as the diffusion coefficient of a particular gas (like Ar) is constant, different values for Dt/a^2 are discussed as different diffusion times. In the plot, it is easily seen that for the low diffusion times only the outermost layers of the ice core exhibit increased concentrations. For larger times, the diffusion process has penetrated the inner core already. When taking the diffusion coefficient of Ar in pure ice (without bubbles) as $3.0 \cdot 10^{-11}\,\frac{\mathrm{m}^2}{\mathrm{s}}$, as was calculated in section 3.5.2, and taking $a = 3.9\,\mathrm{cm}$, only about 28 h have to pass to reach 10 pmAr of integrated contamination in the ice core ($Dt/a^2 = 0.002$, compare figure 6.1). However, in practice in the cold room about 2 mm of the outermost ice is cut off to prevent any contamination by possible melt and refreeze events on the surface. This cut-off is shown in figure 6.1 by the black dashed vertical line. The resulting mean concentrations after cut-off are indicated in the plot. With such a cut-off, the time to reach about 10 pmAr of contamination by diffusion amounts to 99 h ($Dt/a^2 = 0.007$). These times are, however, very short compared to the average storage times of ice cores, which are more in the order of years.
What has been ignored so far is the effect of bubbles in the ice which was introduced in section 3.5.2. With the ratio of gas in bubbles to gas in the ice matrix in the order

of 10^4, the effective diffusivity introduced in equation 3.26 is slowed down by that order. Thus, with a $D_{\text{eff}} \approx 3 \cdot 10^{-15} \frac{\text{m}^2}{\text{s}}$ and considering the cut-off, the time to reach 10 pmAr inside the ice core by diffusion amounts to ≈ 112 a.

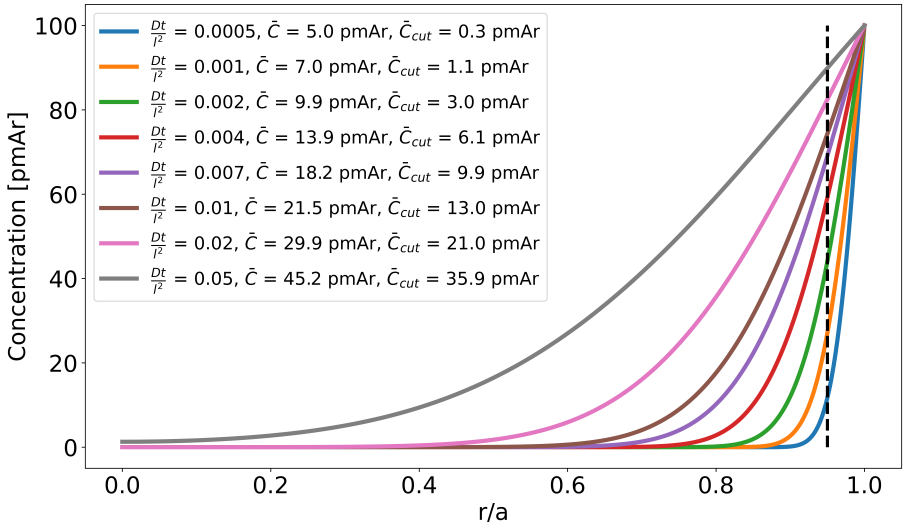

Figure 6.1: Concentration profiles in a cylindrical ice core due to diffusion. Equation 3.20 was used. As initial conditions, $C_1 = 0$ pmAr and $C_0 = 100$ pmAr were used. The different curves represent different values of $\frac{Dt}{a^2}$ and thus different diffusion times (considering constant D and a). The black, vertical line indicates a typical cut-off thickness of about 5% (2 mm of a $a = 3.9$ cm core). The mean concentrations with ($\bar{C}_{cut}$) and without cut-off ($\bar{C}$) are calculated with equation 3.23.

6.2 Samples

As part of a measurement campaign in 2023, samples of an ice core from the Dome du Gouter (DDG, French Alps, 4304 m above sea level) were measured. Parts of the ice core had also been ^{14}C dated (Legrand et al., submitted) and based on this data it was possible to show that the lower parts of the ice core were old enough to expect ^{39}Ar concentrations below the detection limit. The ice core was drilled with a 3" drill in September 1999 and was stored until 2023 in cold storage at -20°. The cutting plan of the sample is shown in figure 6.2. In October 2003, part 1 (1 cm thick) was cut off. In November 2021 the remaining core was cut into three parts, of which parts 3 and 4 were transported to Heidelberg. Several samples were measured, but for the diffusion analysis only sample DDG-41 is considered. Additionally, in 2022, as a first attempt for the diffusion analysis the sample DDG-Test from the lower part of the ice core was measured. An earlier version of the diffusion analysis on DDG-41- was done by Marks (2024) and of sample DDG-Test by von Reventlow (2022). However, since then several parameters have been updated and a new and more thorough analysis of the ^{39}Ar measurements based on Kindermann (2024) (shortly discussed in section 4.6) was conducted.

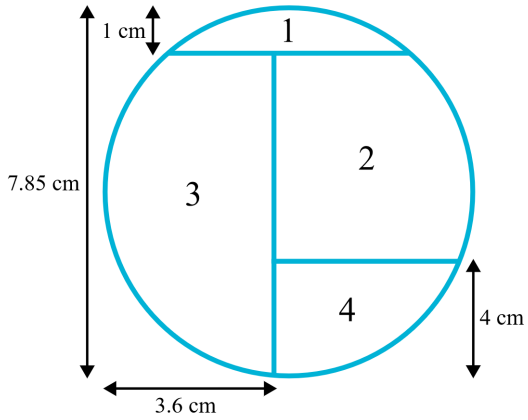

Figure 6.2: Cut plan sketch of the cross-section of the DDG core. Part 1 was cut in October 2003 with a thickness of 1 cm. In November 2021, the remaining ice core was cut into three parts of which part 2 was measured for ^{14}C. Parts 3 and 4 were measured for ^{39}Ar in Heidelberg. Figure analog to Marks (2024).

In table 6.1 the ^{14}C age from Legrand et al. (submitted) for the DDG-41 is given. From this value, the initial ^{39}Ar concentrations is calculated (table 6.2), which is the ^{39}Ar concentration corresponding to the measured mean ^{14}C age. This is the ^{39}Ar concentrations expected in the ice sample at the time of drilling. For DDG-Test, as it stems from the lower part of the ice core an initial ^{39}Ar concentration of 0 pmAr can be assumed.

Table 6.1: ^{14}C concentration and calibrated age for sample of DDG-41 (Legrand et al., submitted). The calibrated date range is shown at 1 σ probability

Sample	DDG-41
Depth [mwe]	22.15-22.42
corrected ^{14}C [F ^{14}C]	0.785±0.034
Cal. ^{14}C-age range [a cal before 1997]	2372 - 1579
Cal. ^{14}C-age mean [a cal before 1997]	1999

6.3 Deriving Diffusion Coefficients

In order to obtain an estimate of the diffusion coefficient of Ar in ice with the results of an ^{39}Ar measurement, samples from the lower part of the DDG ice core were reevaluated with the recently introduced evaluation method by Kindermann (2024), shortly discussed in section 4.6. This method provides a more sound analysis for samples that have an ^{39}Ar concentration close to zero and can provide sensible

Table 6.2: Data of the ^{39}Ar samples. The estimated initial ^{39}Ar concentration (at the time of sampling) was calculated from the ^{14}C data of table 6.1 and refers to the Ar concentration which corresponds to the calibrated ^{14}C mean ages. DDG-Test was from a lower part of the ice core and, therefore, the initial ^{39}Ar concentration can be approximated to 0 pmAr. The calculation of D_{eff}, Z, and D is discussed in section 6.3.

Sample	DDG-41	DDG-Test
Extraction date	09.10.23	20.06.22
Ice mass [g]	1256	2560
Gas content [ml STP]	94.3	58.4
Ar content [ml STP]	0.7	1.43
Est. init. ^{39}Ar conc. [pmAr]	$0.6^{+1.1}_{-0.4}$	0
Measured ^{39}Ar conc. [pmAr]	$4.5^{+7.0}_{-4.0}$	$9.5^{+15.0}_{-9.0}$
Mean effective diffusivity D_{eff} $\left[\frac{\text{m}^2}{\text{s}}\right]$	$5.36 \cdot 10^{-15}$	$1.44 \cdot 10^{-14}$
Upper 1σ limit D_{eff} $\left[\frac{\text{m}^2}{\text{s}}\right]$	$1.62 \cdot 10^{-14}$	$5.57 \cdot 10^{-14}$
Z	75699	22900
Mean diffusivity D $\left[\frac{\text{m}^2}{\text{s}}\right]$	$4.06 \cdot 10^{-10}$	$3.29 \cdot 10^{-10}$
Upper 1σ limit of D $\left[\frac{\text{m}^2}{\text{s}}\right]$	$1.23 \cdot 10^{-9}$	$1.27 \cdot 10^{-9}$

confidence intervals for these cases, something where the old method failed. In the following, the median values of the resulting concentration distributions will be reported as the measurement results, as they are more robust against the skewness of the distributions of low-concentration measurements. Mean and median results did not deviate from each other within their errors.
The analysis towards obtaining the diffusion coefficient estimates is described in the following. First, the time between drilling the ice core and extracting the gas, the radius of the ice core (7.85 cm, internal documentation), the estimated initial ^{39}Ar concentration as discussed in the previous section, and the thickness of the cut-off layer on the outside of the sample are taken into account. The ice core is treated as a perfect cylinder, despite the first thin cut from 2003 and the later cuts from 2021. Without this approximation, the calculations would become much more complex and the goal is to obtain an upper estimate of the diffusivity. Due to the cutting geometry, the measured parts 3 and 4 should obtain more diffused gas after being cut into smaller pieces and thus only lead to an overestimation of D. The same goes for their exterior position in the cut plan, which only leads to a further overestimation of D. Furthermore, the thickness of the cut-off from the outside was approximated to 2 mm.

With these parameters, the mean concentration was calculated with the integral 3.23 for an interval of diffusion coefficients. Then, with the measured ^{39}Ar concentration, the corresponding effective diffusivity is read off. The graph for DDG-41 is shown in figure 6.3. The same process was done for the DDG-Test sample (compare figure A.4). The effective diffusivities obtained from the calculations are listed in table 6.2. The upper 1σ values are calculated with the upper measurement errors. The mean effective diffusivity values are in the order of 10^{-15} and low 10^{-14} for DDG-41 and DDG-Test, respectively. Calculating Z with equation 3.33 and deriving the diffusion coefficient for pure ice with equation 3.26 results in $D_{\text{mean}} = 4.06 \cdot 10^{-10} \frac{\text{m}^2}{\text{s}}$ for DDG-41 and $D_{\text{mean}} = 3.29 \cdot 10^{-10} \frac{\text{m}^2}{\text{s}}$ for DDG-Test. The upper 1σ values are at $D_{\text{max}} = 1.23 \cdot 10^{-9} \frac{\text{m}^2}{\text{s}}$ for DDG-41 and $D_{\text{max}} = 1.27 \cdot 10^{-9} \frac{\text{m}^2}{\text{s}}$ for DDG-Test.

6.4 Discussion

Several points have to be discussed about the derived diffusion coefficients for Ar in pure ice. Important to note is that while the derived diffusion coefficients are very similar for both samples, D_{eff} of DDG-Test is still considerably larger than that of DDG-41. This is due to the fact that in the extraction of DDG-Test, only a comparably small amount of total gas was extracted (compare table 6.2). This was presented in the work of von Reventlow (2022) who stated that this contradicts the final amount of Ar from the sample. As the ^{39}Ar measurement was not distinguishable from 0 pmAr, this does not seem to have come from any kind of contamination during the extraction process. Much more likely is some kind of error in the measurement of the total gas volume. For 1.43 ml of Ar with a stated Ar content of 1.3% (von Reventlow, 2022) the total gas volume should have amounted to about 110 ml, which would result in $Z_{\text{DDG-Test}} \approx 43000$ and with that in a diffusion coefficient of $D \approx 6 \cdot 10^{-10} \frac{\text{m}^2}{\text{s}}$.
In general, it has to be said that in the calculations a rather conservative approach was taken, therefore resulting in rather an overestimation of the diffusivities. One such point is the mentioned assumption of a perfect cylindrical ice core and ignoring the cuts made before the final extraction and the fact that only parts of the ice core were measured (parts 3 and 4 only, compare figure 6.2). Still, the result is about one order of magnitude larger than the theoretical value of $3.0 \cdot 10^{-11} \frac{\text{m}^2}{\text{s}}$ based on the models of Ikeda-Fukazawa et al. (2005) and Kobashi et al. (2015). However, both measurements taken into account are also not significantly deviating from 0 pmAr. Therefore, it is clear that with higher ^{39}Ar countrates and a more thorough flushing procedure of the ArTTA experiment, this value can probably be pushed significantly. It is thus clear that the estimation of D is currently limited by the ATTA-detection limit and therefore all values here can be seen as upper-limit approximations.
What can immediately be said from the measurement results, however, is that for ice cores that have been stored for about 20 a, no significant atmospheric contamination could be detected. Furthermore, taking the diffusion coefficient from DDG-41 and calculating the time to reach a mean of 10 pmAr by diffusion in the ice core under

consideration of a 2 mm cut-off on the outside, it results in a possible storage time of approximately 65 a. 5 pmAr across the ice core are reached after 37 a. When using the upper boundary of D in the order of $2 \cdot 10^{-9}\ \frac{m^2}{s}$, then a storage time of 12 a results in a contamination by 10 pmAr across the ice core, 5 pmAr are reached after about 8 a. In comparison, when using the modeled value of $3.0 \cdot 10^{-11}\ \frac{m^2}{s}$, then 5 pmAr would be reached after 370 a.

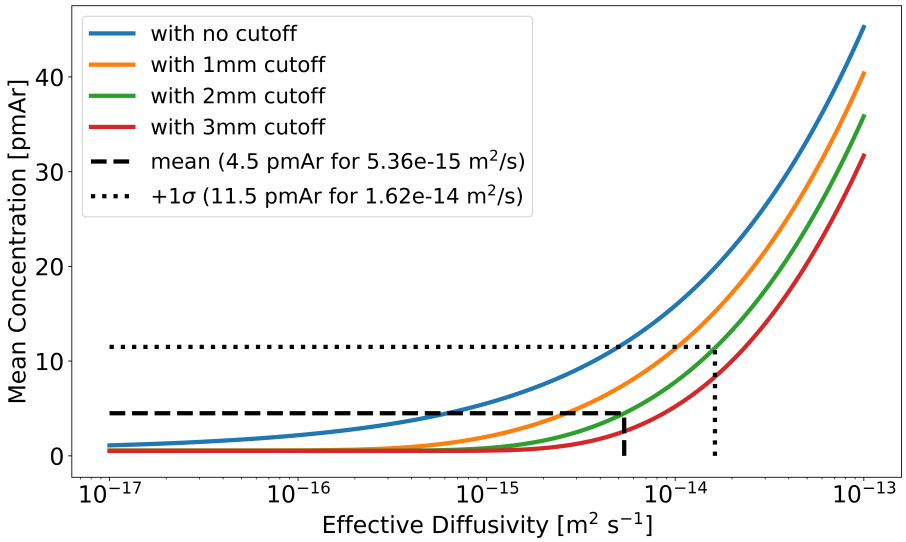

Figure 6.3: Calculated mean ^{39}Ar concentrations for different diffusion coefficients shown for sample DDG-41. A cut-off of 2 mm is considered and a fully cylindrical ice core is assumed. The initial conditions are the estimated initial ^{39}Ar concentrations from section 6.2, $C_0 = 100$ pmAr, and an approximate storage time of 8790 days. The black dashed lines indicate the mean measured ^{39}Ar concentration and the corresponding effective diffusivity. The dotted lines indicate the $+1\sigma$ value and its corresponding effective diffusivity.

In figure 6.3, differently colored lines show the resulting mean concentrations in the ice core for different diffusion coefficients with different thicknesses of the removed layer. Removal of the outermost ice layers is highly effective in suppressing the effects of contamination by diffusion. This comes in addition to the effect it has on the removal of possible melt-and-refreeze type contamination which could affect outside layers.
The overall takeaway of the results is that Ar diffusion into ice cores during storage times of up to several decades cannot yet be completely ruled out. However, there is strong evidence that diffusion does not significantly alter the concentration in ice cores for usual storage times.

7 Age-Depth-Relationship for Weissseespitze Summit Glacier

7.1 Sampling Site and Glaciological Setting

The Weissseespitze (WSS) summit glacier (3499 m a.s.l.) marks the highest point of the Gepatschferner glacier. Its dome-shaped geometry makes it particularly interesting as it offers conditions of very slow ice flow and therefore good preservation conditions for old ice. Figure 7.1 shows an overview of the study site as well as photos depicting the summit glacier. Measurements of borehole temperatures between 2017 CE and 2020 CE showed sub-zero temperatures in the whole ice column, implying that the ice is still frozen to the bedrock (Bohleber et al., 2020; Fischer et al., 2022). The thickness of the summit glacier was measured to 12 m at the ice divide by Bohleber et al. (2020) and is rapidly declining due to melting (Fischer et al., 2022). Extensive historical data is available for the WSS summit glacier e.g. with the gridded *Historical Instrumental climatological Surface Temperature and precipitation time series of the Greater Alpine Region* (HISTALP) dating back to 1800 CE and federal mapping campaigns of Tyrol in 1870-1887 CE. Fischer et al. (2022) provides a detailed discussion of historical sources and states a maximum elevation of the ice cap at the end of the 19th century at about 3534 m a.s.l., translating to an ice cap thickness of about 47 m. The authors also state that extrapolating current average surface mass loss rates results in a complete loss of the ice cap within the next 30 a. Furthermore, the oldest ice remains at the bottom of the ice sheet frozen to bedrock, offering an alternative climate signal for periods of low ice cover in the Alps (Bohleber et al., 2018). This archive will also soon be lost due to the warming of the basal layers above 0° C.

The urgency, which applies to all alpine glaciers below 4000 m, has sparked a new effort of retrieving ice from the WSS and led to the drilling of two parallel 10 m ice cores in March 2019 CE. Analysis for aerosol-based micro-radiocarbon ice dating was performed at Paul Scherrer Institue (PSI) and stable water isotopes analysis was performed at the IUP. Furthermore, ^{3}H was measured on three additional shallow cores from the same location at Seibersdorf Laboratories (Bohleber et al., 2020). The ^{3}H analysis showed no sign of the elevated levels after the 1960s, indicating surface ages above 60 a. The radiocarbon analysis, which was performed for the six meters above bedrock showed an increasing age profile with depth with a maximum age of about 6000 a calibrated ^{14}C age at the bottom and reaching below 1000 a $>$ 7 m above bedrock.

In March 2021 CE, an additional parallel core at the same location (using DGPS)

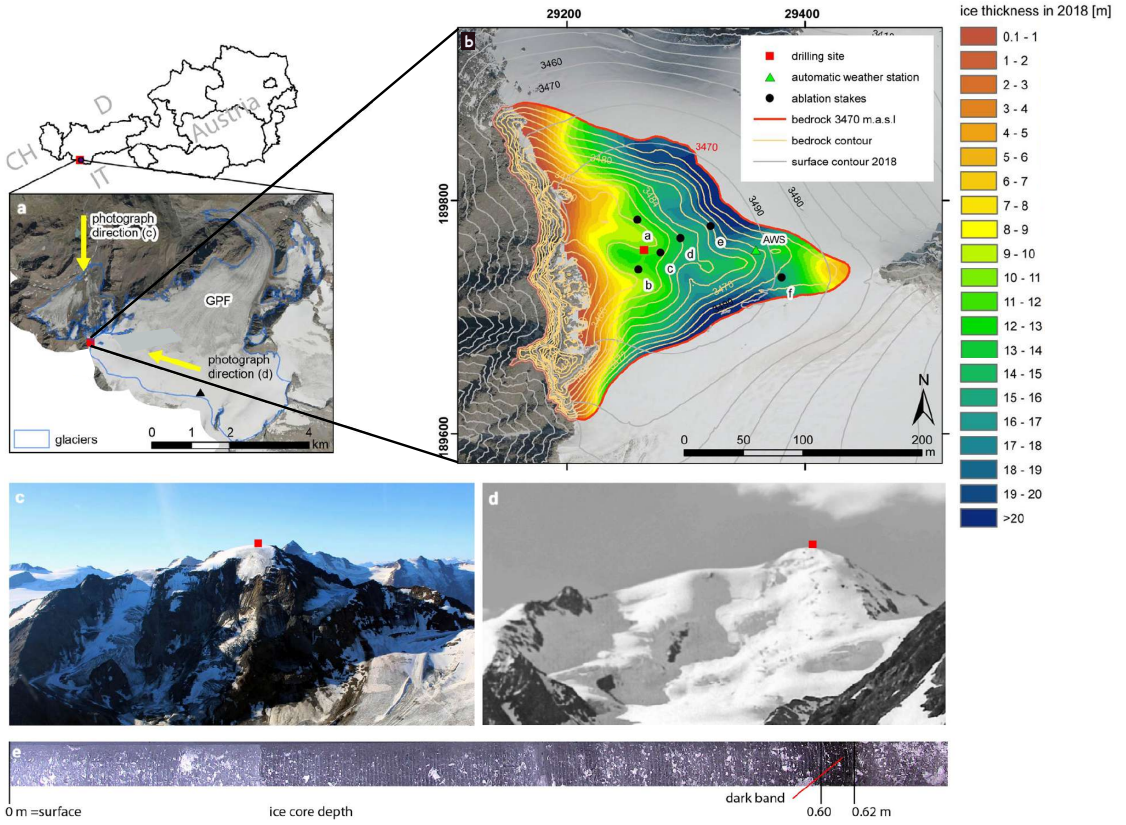

Figure 7.1: **(a)** The ice core drilling site at the summit of WSS ice cap; **(b)** bedrock topography from GPR measurements and calculated ice thickness in 2018; **(c)** and **(d)** Panoramic view of the WSS ice cap in 2019 CE and 1930 CE, respectively; **(e)** One of the ice cores taken in 2019 CE. Figure adapted from Fischer et al. (2022) and Spagnesi et al. (2023a).

was drilled, measuring 8.7 m to bedrock. In the work by Spagnesi et al. (2023a), for one of the 2019 CE ice cores stable water isotopes, major ions, and levoglucosan were measured by CFA analysis, while the 2021 CE core was analyzed for microfossils including microcharcoal. The results show distinct peaks which indicate a good preservation of the ice and can be interpreted as phases of fire activity in the region. As part of the FWF- and DFG-funded project 'Novel Dating of Alpine Glaciers by ^{39}Ar-TTA' which enabled this thesis (under the D-A-CH collaborative), the establishing of a better age-depth profile for the upper part of the ice column at WSS was approached with the use of ^{39}Ar dating, as radiocarbon fails to resolve ages below 1000 a. For this purpose, several sampling campaigns have been conducted in recent years. In June 2023 CE, a first attempt to retrieve a new core at the summit of WSS for ^{39}Ar dating was conducted. However, due to the failure of the winch for the 3" drill, only 2 m were retrieved with the mechanical 2" drill.
A second attempt was conducted in May 2024 CE, which again experienced a failure of the drilling equipment of the 3" drill. Still, different samples were retrieved: four

surface samples cut by chain saw, 86 cm of 3" thermally drilled core, 60 cm of 3" mechanically drilled core and 4 m of 2" core drilled with a hand-held mechanical drill (Langenbacher, 2024). This was done because an additional objective of the project was the comparison of different ice drilling techniques and their robustness for further ^{39}Ar analysis.

7.2 Results

In the following section, the new measurement results for the WSS samples are presented and put into context with the calculated radiocarbon ages from 2019 CE and newly acquired radiocarbon data. Furthermore, a common depth scale for samples from different years is established and discussed. Subsequently, the age-depth relationship is analyzed by fitting the three discussed models to the combined data. For the best-fitting model, the derived parameters are discussed.

In the following, the measurement data for ^{39}Ar abundances are presented. In the context of this thesis, the master thesis by Marks (2024) and the bachelor thesis by Langenbacher (2024) were supervised which both already dealt with parts of the measured data from the WSS and therefore already presented some of the following data as part of smaller projects. Here, a more thorough analysis of the data is conducted, based on the methods and models which Marks (2024) and especially Langenbacher (2024) introduced. The main differences in the measurement data compared to the former theses consist of corrected depths, an additional ^{14}C data point, and a new evaluation method of the ^{39}Ar measurements (compare section 4.6), resulting in slightly changed ^{39}Ar ages.
Table 7.1 gives an overview of the samples taken in 2023 CE and 2024 CE, which were analyzed for ^{39}Ar. The ages are already corrected for the varying atmospheric input function as described in 4.6. Two samples, indicated with an *, did not provide enough gas and had to be diluted with ^{39}Ar-free Ar. The presented abundance and age are already corrected for this mixing. In table 7.2 an overview of the ^{14}C data is given. The samples were measured on an ice core from 2019 CE and all except one are presented in the work by Bohleber et al. (2020). The additional data point of the same core, WSS_Run15, was measured in 2024 CE and added to the data. The lowermost sample, WSS_Run17-2, is not used for the following analysis as it is probably biased due to the likely inclusions of radiocarbon-dead material through ice-bed interaction, as stated in the publication.
Figure 7.2 shows a depth profile of all ^{39}Ar and ^{14}C ages. The colors indicate the different years and types of samples. Furthermore, data points not taken into account in the following are indicated in red. This selection was due to several quality checks. First of all a good decontamination of the ice as described in section 4.2 is necessary. As stated in Langenbacher (2024) this was not done for the samples WSS24_SurfaceA and WSS24_SurfaceB as not enough ice was cut off from the firn-ice-transition. This presumably led to significantly increased ^{39}Ar abundances.
Furthermore, sample WSS24_Core3_Sample3 was deselected from further analysis

Table 7.1: Overview of all samples from 2023 CE and 2024 CE which were analyzed for ^{39}Ar. Depth is given as the mean depth of the sample in reference to the surface in the year of sampling. Age is given as corrected values with the input-correction by Happel (2024) and the analysis following Kindermann (2024) as described in section 4.6 in years before 2024 CE. ^{39}Ar abundances and ages marked with an * indicate samples that had to be diluted with ^{39}Ar-free gas to obtain enough gas for a measurement. The values given here are already corrected for the dilution. The year of sampling can be inferred from the sample name. Italicized samples are not regarded in the analysis for reasons discussed in the main text.

Sample	Depth [m]	Length [m]	Weight [kg]	^{39}Ar [pmAr]	^{39}Ar Age [a b. 2024]
WSS23_Run12upper3	0.33	0.66	2.85	38^{+11}_{-10}	397^{+121}_{-85}
WSS23_Runlower34	1.00	0.66	3.09	34^{+11}_{-10}	444^{+124}_{-106}
WSS23_Run5	1.67	0.66	2.63	32^{+12}_{-10}	469^{+128}_{-122}
WSS24_SurfaceA	0.05	0.10	2.50	78^{+26}_{-22}*	118^{+133}_{-124}*
WSS24_SurfaceB	0.08	0.15	4.56	76^{+20}_{-15}	127^{+86}_{-109}
WSS24_SurfaceC	0.07	0.13	3.76	36^{+12}_{-10}	408^{+123}_{-97}
WSS24_Core1_Sample1 (mechanical)	0.32	0.61	2.55	48^{+13}_{-11}	318^{+90}_{-100}
WSS24_Core2_Sample1 (thermal)	0.32	0.61	2.47	43^{+22}_{-17}*	346^{+190}_{-153}*
WSS24_Core3_Sample3 (handheld mechanical)	3.12	2.11	4.40	36^{+11}_{-10}	420^{+124}_{-95}

as it showed very low ice quality. During sampling, only small pieces could be retrieved at a time and therefore the sample was made up of 34 individual pieces, each about 10 cm long. As this greatly increases the risk of atmospheric contamination by entrapped air, this sample is not considered in further analysis.
Lastly, the WSS24_SurfaceC sample did not pass the quality check built into the new analysis program. As described briefly in section 4.6 and more thoroughly in Kindermann (2024), the new analysis routine evaluates the statistical temporal distribution of the atoms over the measurement. In the case of WSS24_SurfaceC, the atom times showed a significantly non-statistical distribution which hints towards an unstable operation of the experiment. Therefore, the measurement is discarded as well.
However, in contrast to the work by Langenbacher (2024), the sample WSS24_Core2_Sample1 which was drilled with the thermal drill is not omitted from the data. In Langenbacher (2024) it was evaluated with the old evaluation method and the sample showed a significantly younger age than the other samples. During sample retrieval, the control box started to overheat and therefore the sample was drilled very slowly. Hence, it showed clear signs of strong melting on the outer core surface

even causing varying diameters. With this in mind, the younger age was interpreted as a consequence of the imperfect sampling and thus atmospheric contamination by refreezing. With the new analysis routine, however, the sample's age does not differ significantly anymore from the other samples and was therefore not omitted from the dataset. The reason for the shift in concentration for few samples is a different ensemble of reference measurements. The new analysis allows a statistically sound combination of reference measurements over longer periods, which was not possible with the old method. With the old evaluation method, only the references directly before and after a measurement were considered, making it more susceptible to statistical fluctuations.

Table 7.2: Overview of samples from the 2019 CE ice core which were analyzed for ^{14}C. Data taken from Bohleber et al. (2020) and drilling logs. Depth is given as the mean depth of the sample referenced to the surface in the year of sampling. The sample of run 15 was analyzed in 2024 and was therefore not part of the publication. Ages are given as calibrated ages before present (cal BP).

Sample	Depth [m]	Length [m]	Weight [kg]	^{14}C [pmC]	^{14}C Age [a cal BP]
WSS19_Run7	5.11	0.70	0.40	93.0±4.6	623±350
WSS19_Run9	6.20	0.55	0.25	91.0±1.9	735±145
WSS19_Run12	8.04	0.59	0.44	84.7±4.6	1347±456
WSS19_Run15	9.77	0.65	0.83	76.1±0.8	2190±104
WSS19_Run16	10.33	0.48	0.30	65.7±1.3	3661±200
WSS19_Run17-1	10.85	0.56	0.17	52.9±4.1	5884±739
WSS19_Run17-2	basal	ice	0.15	22.3±0.6	14020±332

Δage

The data sets at hand combine two fundamentally different types of ice dating. ^{39}Ar is a gaseous species and is therefore incorporated in the bubbles of the ice. ^{14}C on the other hand is measured on precipitated carbonaceous aerosols, thus on the ice matrix. As discussed in section 3.1.1, the time interval between snowfall and the pore close-off further down in the firn column causes an age difference between tracers in the ice matrix and the gas. To correct for this difference, 30 a of Δage were added to the ^{39}Ar ages, an estimate based on the findings at nearby glaciers by Festi et al. (2021) and Gabrielli et al. (2016).

Establishing a Common Depth Scale

Combining the data sets of ^{39}Ar and ^{14}C allows a complete coverage of the profile of the ice sheet on WSS by measured ages. However, attention has to be paid, as the

Table 7.3: Surface mass balance values taken from Fischer et al. (2022) and from personal communication with the authors. The values are given in meters of ice equivalent.

Year [CE]	2018	2019	2020	2021	2022	2023
Surface Mass Balance [m i.e./a]	-0.63	-0.35	-0.04	-0.6	-0.7	-0.8

samples are from different years, and as shown by Fischer et al. (2022), the surface of the ice sheet suffers from prolonged mass loss. As the cores taken in 2023 CE and 2024 CE were not drilled to bedrock and no common horizon was visible in the ice, the depth scale has to be established from annual surface offsets. For this and analogous to the work presented in Langenbacher (2024), the annual surface mass balance has to be taken into account. Table 7.3 shows the surface mass balance (SMB) in the years since 2018 CE, based on data from Fischer et al. (2022) and personal communication with Andrea Fischer and Martin Stocker-Waldhuber from the Institute for Interdisciplinary Mountain Research, Innsbruck. Important to note is that the values are average values for the entire peak region. Spatially, they can vary strongly as shown in Fischer et al. (2022), where differences between ablation stakes of up to 75 cm are seen. Furthermore, despite using a precise differential GPS to find the drilling location from former years, spatial deviations of up to 10 m are possible (M. Stocker-Waldhuber, personal communication). Figure 7.1 shows that this can lead to depth topography changes of up to about 2 m. However, the effect is probably significantly smoothed out by the snow and ice build-up and effects like wind erosion. A well-visible dust layer that melted out quite homogeneously across the summit region in 2022, as seen in figure A.2, rather points towards spatial layer height variation around 10-20 cm. All in all, depth values of years other than 2019 CE are shifted according to the values in table 7.3, and a conservative error of 1 m is estimated.

Furthermore, as depth always refers to a reference surface and this is changing over time, in the following everything is presented in terms of height over bedrock, instead of depth below some annual surface. The conversion was done with the 2018 CE thickness of the ice sheet of 12.1 m and the surface mass balance as reported in Fischer et al. (2022), listed in table 7.3. With this measure, a more constant metric is established, which can more easily be applied to potential future ice cores that are drilled to bedrock. Nonetheless, because the wording is otherwise uncommon, the profile of ages throughout the ice column is still referred to as *age-depth profile*, the term *age-height profile* is simply not very intuitive.

For the models introduced in section 3.4, the parameter conversion from depth to height above bedrock was done by setting $h = H_{\max} - z$, where h is the height above bedrock coordinate, z is the depth coordinate and $H_{\max}$ is the maximum thickness of the ice sheet of 47 m (see next section).

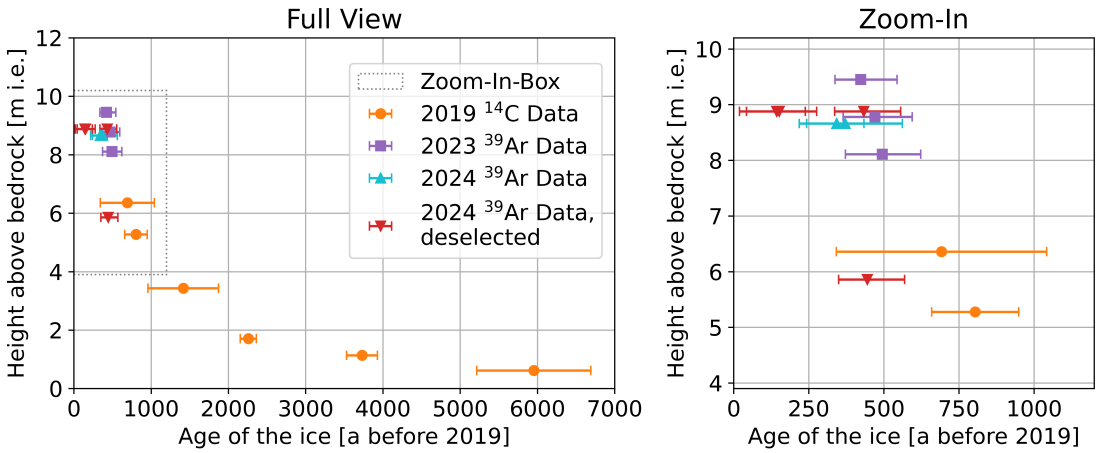

Figure 7.2: All ^{39}Ar and ^{14}C data points from WSS plotted as age vs. height above bedrock (in meters ice equivalent (m i.e.)). On the left, the full profile can be seen, on the right a close-up view of the upper (younger) part is displayed. Data from different years is indicated in different colors. The red data points did not pass the quality checks as discussed in the main text and will be omitted from the further analysis.

Monte-Carlo Fitting of the Data

In order to establish an age-depth relationship for the full ice profile at the WSS summit drilling location, the models introduced in 3.4 are fitted to the data.
Important to note is that the models all describe glaciers in a steady state. This means that the *last steady state* (LSS) at WSS has to be estimated and the models have to be fitted accordingly. The basic Sorge's law of glaciology then states that the age-depth profile of an ice sheet remains constant under steady-state conditions. From Fischer et al. (2022) and following the analysis by Langenbacher (2024) the LSS is estimated to have happened around the year (1914 ± 50) CE at an ice thickness of (47 ± 10) m. The timing of the LSS was chosen as the last time interval which showed no significant ice loss. However, accounting for the low accuracy of the early data stemming mostly from old maps and aerial photos, a conservative error of 50 a is chosen. This way, the LSS is estimated to lie between the LIA maximum around 1855 and the beginning of in-situ SMB measurements in 1969. With these estimates, the measured ages can then be shifted to the time of the last steady state, and the models are fitted before translating it back to the present.
The approach for data fitting taken in this thesis is based on Monte-Carlo (MC) sampling. For ^{14}C as well as ^{39}Ar measurements the ultimate obtained abundance and age data comes in the shape of distributions. When looking at the age data, among other reasons due to the internal statistics as well as the non-linear relationship of abundance and age, the distributions are non-symmetrical. As normal fit algorithms (like the Python library scipy.optimize.curve_fit) cannot deal with non-symmetrical errors, a different approach has to be taken. By MC sampling the distributions,

for each iteration fitting the samples with the model and finally averaging the fit parameters, the full complexity of the distributions for each data point can be accounted for in the fitting procedure. This was done for the data at hand with a sampling number of 10^5. For the ^{39}Ar ages the full (input curve corrected) age distributions were used. For the ^{14}C ages, unfortunately, the distributions from the OxCal software were not available. Therefore, Gaussian distributions with the values for mean and standard deviation from table 7.2 were used. Additionally, the depth for all ^{39}Ar values were sampled from Gaussian distributions with mean values as indicated in table 7.1 and standard deviations of 1 m, as previously discussed. Furthermore, also the timing and thickness uncertainties of the glacier at the LSS are incorporated into the fitting by taking them as Gaussian distributions around their mean value and the discussed uncertainty and sampling from it in the MC fitting procedure.
With this approach, the non-linear interplay of the different parameters and their uncertainties are considered in the final fit parameters and their errors by simply fitting a large data set which in itself contains all uncertainties.
Table 7.4 summarizes the fitted parameters and figure 7.3 shows the models and data points graphically. The values in table 7.4 were converted from meter ice equivalent (m i.e.) obtained from the fit to the more general meter water equivalent (m w.e.) using an ice density of 900 kg/m^3 (Festi et al., 2021).

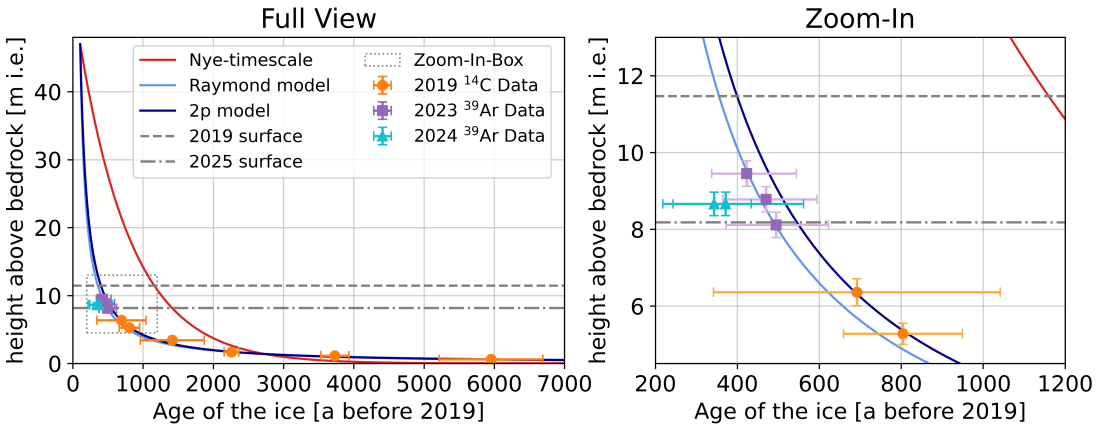

Figure 7.3: Plot of age data points vs. their height above bedrock (in meters ice equivalent) of the last steady state (LSS) from 1914 CE (47 m thickness). The left side shows the full profile, right side shows a close-up view of the younger section. The depth error bars indicate the length of the sample, not the depth uncertainty. Also shown is the average fit function from the MC fitting procedure for the different models. The respective parameters can be found in table 7.4.

Table 7.4: Average fit parameters of the MC fitting procedure. Accumulation rate values are converted to meter water equivalent (m w.e.) by multiplying with an ice density of 900 kg/m^3 (Festi et al., 2021).

Model	Accum. Rate A [m w.e./a]	Thinning Param. p	χ^2_{red}
Nye-timescale	0.0566±0.0044		48
Raymond model	0.523±0.051		0.58
2p model	0.412±0.129	0.91±0.11	1.08

7.3 Discussion

In the preceding section, the age data obtained from the WSS summit glacier was presented and the models and fitting process were introduced. In the following, the results will be discussed.
From the last column of table 7.4 displaying the reduced chi-squared (χ^2_{red}) value, it is apparent that the Nye model is not able to capture the age profile of this ice sheet. The rate of change from a slowly increasing age with depth to a very steep age gradient cannot be captured by this model as is also apparent from the visualization in figure 7.3. As described in section 3.4, this is not very surprising as the Nye model describes ice sheets with non-zero flow velocities and therefore is not well suited for the setting at the WSS summit glacier. The two other models, conceptualized for an ice divide setting, are much more suited to describe the age-depth relationship. The χ^2_{red} are close to 1 and thus show the good applicability of the models. Even though the 2p model adds a parameter to the Raymond model it does not perform significantly better than the latter. The Raymond model shows a smaller χ^2_{red} of 0.58, which on the one hand indicates a better fitting of the data than the 2p model with a χ^2_{red} of 1.08. However, on the other hand, χ^2_{red} values of less than 1 are usually interpreted as a sign of overfitting of the data. This contradicts the fact that the Raymond model has fewer parameters than the 2p model and is otherwise the same function. It seems that the additional parameter of the 2p model does not significantly enhance the fitting of the data and that the Raymond model is sufficient to capture the data. It will therefore be the focus of further analysis in the following.

Depth of Samples

As already indicated in the previous sections and tables 7.1 and 7.2, the analysis for ^{14}C and especially for ^{39}Ar requires ice amounts of several 100 g and even several kilograms, respectively. For that reason, several tens of centimeters of ice cores have to be analyzed together. In the analysis at hand, the depth of such a sample was taken as the average depth of the ice section. This, however, implies a linear distribution of ages in this section as well as a homogeneous distribution, in the case of ^{14}C, of the water-insoluble organic carbon (WIOC), in the case of ^{39}Ar of the

bubbles within the ice. The resulting age-depth relationship does not show obvious hiatuses, which corroborates the first point to some degree. Even though, the mixing of sample ice of different depths smoothes out such jumps. Nevertheless, such an effect should be visible in the goodness of the fit of the model. For the second point and regarding the here measured ^{39}Ar data, no visually obvious bubble-free or particularly bubble-rich layers were identified in the ice cores.

Accumulation Rate

The parameter that is fitted by the Raymond model is the accumulation rate. However, the interpretation of the result is not trivial, as data from 6000 a is fitted to obtain one parameter. Due to the changing climatic history of the region and probably also changing weather patterns it cannot be expected that this parameter remained constant over time. Therefore, the result should be understood as an accumulation rate type parameter that gives a rough estimate of the average accumulation rate over the last 6 millennia. The Raymond model results in a value of $A = 0.523 \pm 0.051$ m w.e./a. This lies very close to the value of 0.59 m w.e. which Fischer et al. (2022) gives for the total precipitation in months of snow accumulation for the years 1800 CE to 2024 CE. It is also expected to obtain accumulation rates smaller than this value, as wind erosion and melt events will always have negative impacts on the accumulation of precipitation at summits.
A comparable study at a glacier in the region of WSS was conducted at Mt. Ortles by Gabrielli et al. (2016). While they found evidence of a not yet understood strong thinning towards the lower part of the ice sheet preventing a fitting by the Raymond or 2p model, they observed accumulation rates of around 0.8 m w.e./a. Also, other studies in the area showed values around 0.8 to 0.9 m w.e./a, e.g. Festi et al. (2021) 0.85 m w.e./a for Adamello glacier and 0.9 m w.e./a for Silvretta glacier by Pavlova et al. (2015). The lower value for the WSS can be interpreted as an effect of stronger wind erosion, due to its exposed position with no other high mountains around.
The other result can be drawn from the good fit of the Raymond model and the fit result for the thinning parameter $p = 0.91 \pm 0.11$ of the 2p model which is not significantly different from $p = 1$. This means that a thinning parameter of $p = 1$ is sufficient to describe the conditions of the ice sheet, indicating isothermal conditions throughout the ice profile. The 2p model was proposed by Bolzan (1985) for the setting at Dome C with an ice sheet thickness of several thousand meters. For such thick ice sheets, it may be required to account for different temperatures and thus viscosities in the ice column. For the < 50 m thick ice sheet at WSS, it can be expected that the additional parameter is not needed.

Last Steady State - Sensitivity Analysis

With the implemented MC sampling, the uncertainties of the LSS ice thickness (47 ± 10 m) and its timing (1914 ± 50 CE) are already taken into account in the fit parameters and their uncertainties. Even though both parameters were estimated very conservatively and exhibit large errors, their impact on the total error of the

fit parameter is negligible. The additional MC sampling for these two parameters did not change the accumulation rate parameter until the third significant digit and increased the error of the parameter by about 13%.

7.3.1 Age-Depth Profile

With the ^{39}Ar data points completing the coverage of the whole depth column with measured ages and a suitable model to fit the data, the age-depth profile of the WSS summit glacier can now be well constrained. In figure 7.4 the resulting best fit of the Raymond model and its uncertainties are displayed in an overview plot as well as a residual plot. The uncertainty ranges (for 1σ, 2σ, and 3σ shaded in different shades of blue) are computed from the distribution of the fit parameter following the MC analysis and therefore incorporate all measurement uncertainties.

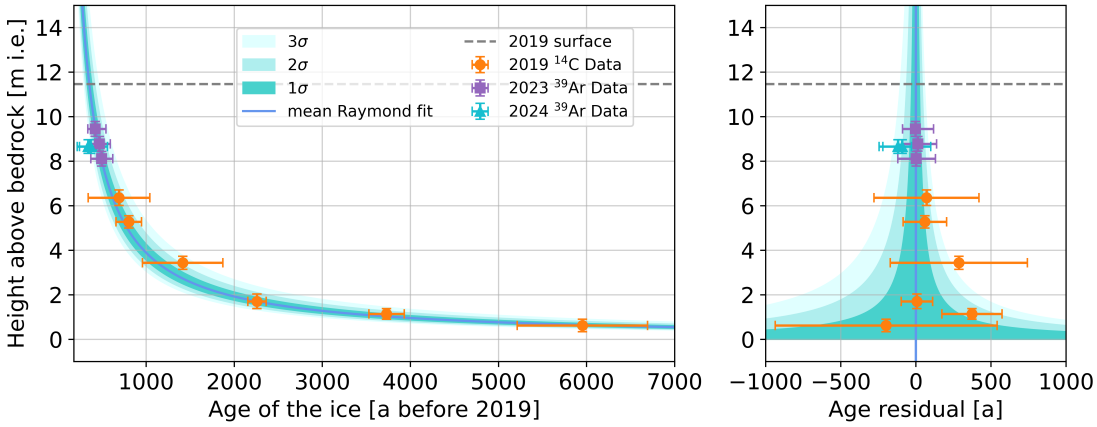

Figure 7.4: Plot of age-depth relationship from the Raymond model on the left. On the right a residual plot of the model and data points for better visualization. The shaded areas indicate the age uncertainties obtained from the 1σ, 2σ, and 3σ values from the MC fitting. The depth error bars indicate the length of the sample, not the depth uncertainty.

From the ^{39}Ar ages, it can be seen that the 2023 CE and 2024 CE surface consists of around 400 a old ice. This shows how much ice has already melted in the past decades and points towards the need for the ^{39}Ar tracer for the dating of the upper part of ice cores. While for younger surface ages tracers like ^{3}H or ^{210}Pb can determine the ages of the upper layers and thus complement ^{14}C ages from lower layers, this is not possible anymore with the progressing melting of glaciers in the Alps. Without reliable surface ages, however, also layer counting can only provide a very limited floating age-depth relationship.

Considering the large amount of ice loss observed at WSS over the past decades, the question arises if the WSS summit has experienced similar periods of strong mass

loss during the 6000 a recorded in the ice sheet. At least for the past 2000 a, a hiatus in the order of 400 annual layers seems to be quite unlikely given the good fit of the model to the data with errors of measurements and fit well below 400 a. Further below, this is harder to constrain as the absolute errors of the ^{14}C measurements increase. However, the model shows errors below 200 a down to 2 m above bedrock. All in all, melt events erasing several hundred years cannot be excluded for times > 2000 a BP, however indications for such events are also absent in the dataset.
As a further analysis of the applicability of the model, it was fitted separately to the ^{39}Ar and the ^{14}C data only. The results for the accumulation rate parameter did not change significantly: $A_{^{14}\mathrm{C\,only}} = 0.523 \pm 0.051$ [m w.e./a] and $A_{^{39}\mathrm{Ar\,only}} = 0.529 \pm 0.132$ [m w.e./a] (compare table 7.4). This corroborates the Ansatz of a model with an assumed constant accumulation rate over time. Thus, there seems to be no evidence for major changes in the average snow accumulation rate at the WSS summit over the last 6000 a which hints towards stable seasonal temperatures and precipitation (compare Fischer et al., 2022).

All in all, this study shows the great value that ^{39}Ar dating has for alpine ice core dating. On the one hand, surface ages become increasingly old thereby surpassing the range of traditional dating tracers. It can, on the other hand, also complete age-depth profiles where surface ages might still be acquired, but an obvious data gap is present between the young age tracer results and the old ones as seen for example in the work of Jenk et al. (2009) and Gabrielli et al. (2016). For the study at hand, the ^{39}Ar tracer was the only way to obtain age constraints for the upper half of the ice core and in combination with ^{14}C ages results in a well-covered age-depth relationship.

7.3.2 Applying the Age-Depth Profile to Other Tracers

The age-depth relationship in itself already contains a lot of information on past climatic conditions at the study site and in the surrounding region. However, age-depth profiles are also important as they give a timescale to other depth resolved tracers measured on such ice cores. In this case, Spagnesi et al. (2023a) presented data for the stable water isotopes as well as major ion chemistry, levoglucosan, and microcharcoal in another WSS ice core from 2019 CE and one from 2021 CE. They found four distinct depths showing increased signals in the microcharcoal concentration in the 2021 CE core and matching signals for increased levoglucosan in the 2019 CE ice core. From this, four phases of increased fire activities were inferred. However, the study was not yet able to put well-constrained ages to the signals. With the work presented here, it is now possible to give age estimations with reasonable uncertainties.
In figure 7.5 the levoglucosan data from Spagnesi et al. (2023a) (downloaded from their indicated publicly available repository, 04.12.2024) is presented with the depth axis at the bottom. By applying the presented age-depth relationship, a corresponding age axis was added on the top. Please note that this axis is not linear, as the layers

thin out towards the bottom of the ice core. Spagnesi et al. (2023a) indicated four areas of increased levoglucosan and microcharcoal concentrations which point towards enhanced wildfire activities in the surrounding area, however, not ruling out post-depositional effects enhancing such signals. Figure 7.5 shows the same shaded areas now with age information on their onset and end. Uncertainties are calculated with the standard deviations of the fit parameter. For the large peak found at 6.44 m depth (below 2019 CE surface) a separate age of 779^{+71}_{-59} a is given. This indicates potential large wildfire activities in the region around the year 1240^{+59}_{-71} CE. This should of course be checked with local records or other climate data to see if an event like this fits into the history.

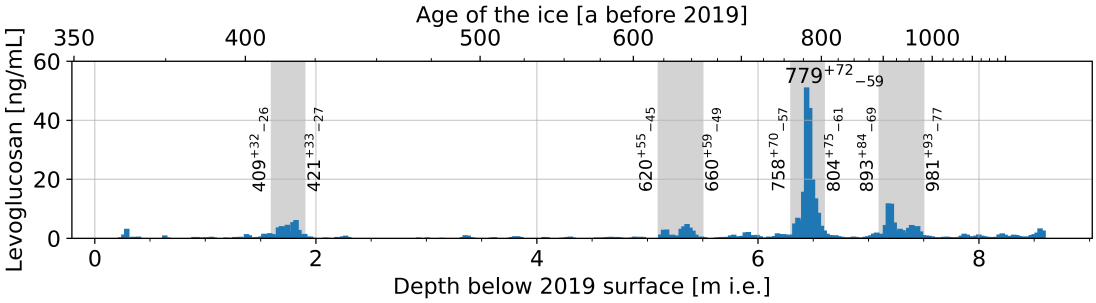

Figure 7.5: Levoglucosan data from Spagnesi et al. (2023a) with an added age axis on the top. Please note that the age axis is not linear due to the thinning of the layers in the ice core. The shaded areas indicate times of peaking levoglucosan concentrations (as done in the original work). Vertical numbers indicate the age of the onset and end of the periods of increased signal. The age of the main peak at 6.44 m depth is given separately.

7.3.3 Comparing Different Sampling Methods

Lastly, a comment on the different sampling methods is made. During the two attempts to drill ice cores to bedrock at WSS in 2023 CE and 2024 CE, different approaches to extracting the sample ice from the glacier were made. The main focus was the drilling with a 3" mechanical and thermal drill. Furthermore, a 2" handheld mechanical drill was used upon the failure of the larger drill's control box. Additionally, samples were cut from the surface with a chain saw. All in all, an intricate quantitative analysis cannot yet be conducted. However, certain takeaways can already be summarized. First of all, ice blocks cut from the surface seem like the least critical sampling method as their small surface-to-volume ratio makes them less prone to contamination. However, as these blocks are typically cut right from the surface, great care has to be taken for their decontamination. As was the case for two surface samples from the 2024 sampling, a too sparing cut can result in significantly younger ages. This is especially true for the upper surface of the blocks, which was exposed to the elements and thus often exhibits larger cracks and connecting bubbles. The second type of samples analyzed here were the mechanically drilled cores. As

long as the ice quality is good, these samples do not show proneness to contamination by atmospheric air as can be seen for the samples from 2023 and sample WSS24_Core1_Sample1. However, samples consisting of brittle ice and therefore many pieces should be avoided. Mechanically drilled samples have also been analyzed in other studies like Ritterbusch et al. (2022) and Legrand et al. (submitted) (see chapter 10) and showed no problem with contamination.
Lastly, a thermal drill was employed for sample retrieval, however, as mentioned, under non-ideal circumstances due to technical failure. Nevertheless, the result presented in this thesis, following the new data analysis method, shows no significant age difference from the mechanically drilled samples from the same location. A more thorough analysis is yet to be conducted, preferably adding a ^{85}Kr analysis as done by Ritterbusch et al. (2022) to precisely quantify the contamination. The reason is that the thermal drill melts through the ice, thus increasing the chances of the trapping of atmospheric air by melt and refreeze occurring along the outer surface of the ice core.

7.4 Summary and Outlook

The age dating results of the WSS summit glacier with the tracers ^{39}Ar and ^{14}C reveal a continuous age gradient with depth reaching a maximum age of 6000 a just above bedrock. An age-depth model was fitted to the data and now enables the calculation of a continuous age profile of the ice sheet at this position. By composing a fit algorithm based on MC sampling of the distributions of the measured values as well as including the uncertainties of other parameters such as the common depth scale, the thickness, and the timing of the last steady state, the uncertainty of the model parameter was determined incorporating the full complexity of the setting. This result enables the application of the age-depth profile to other depth-resolved tracers and to assign ages with reasonable uncertainties to their signals.
Furthermore, to investigate past conditions at the WSS summit glacier the age gradient was analyzed for potential hiatus due to periods of mass loss in the past, and the agreement of the model fit for the upper and the lower part of the data set was evaluated. For the former, at least for the last 2000 a, a hiatus on the order of 400 a seems very unlikely given the uncertainty ranges of the measured ages. This would indicate that the current loss of surface layers is unprecedented at least in the past two millennia. Concerning the latter, the fits for only the upper (^{39}Ar) data points and only the lower (^{14}C) data points do not result in a significantly different model parameter, i.e. accumulation rate. This means that in the data set no evidence is found for major changes in the average snow accumulation rate at the WSS summit over the past 6000 a, until the current surface age of about 400 a.
More measurements are envisaged to create an overlap of ^{39}Ar and ^{14}C data points and thus tie down the age profile even more accurately. Furthermore, the actual probability distributions of the ^{14}C age data could not be obtained from the colleagues within the time period of this thesis. As these distributions can be very non-symmetric and even multi-modal, incorporating the actual distributions into

the MC fitting routine instead of their Gaussian placeholders could result in slightly shifted parameters.

8 Jamtalferner - A Transient Glacier

While summit glaciers like the WSS summit glacier discussed in chapter 7 can provide a continuous ice record over several millennia, a glacier like the Jamtalferner reaches low altitudes and into a side valley that has seen a long history of human activity (Reitmaier et al., 2013). Therefore, studying this glacier system provides insight not only into the climate history of the region but also into its interplay with human activities around it. Furthermore, due to its low altitude, changes in the climate over time have a profound influence on the size of the glacier. They are recorded in the ice extent and the moraines left behind from former glacial advances. To tap into this archive, in September 2021 CE a sampling campaign was conducted with colleagues from the Institute of Interdisciplinary Mountain Research, Innsbruck at Jamtalferner, retrieving surface blocks from six locations on the glacier. A photo of the campaign made it onto the cover page of the Physik Journal, in November 2021 CE (see picture A.1). In November 2021 CE, a second sampling campaign was conducted to retrieve ice cores from the same locations. In September 2023 CE, a large piece of human-processed wood and surrounding ice was retrieved from the Urezzajoch mountain saddle at the top of the glacier by the same colleagues.
In the following section, the glaciological setting will be discussed briefly. Afterward, a brief summary of other studies of the glacier concerning its past extent is given before novel data is presented on the ages of the ice along the glacier tongue. Finally, a new use case of the ^{39}Ar isotope is presented, which enables the dating of moraines. Applying this to the LIA moraines adds to the comprehensive picture of the glacier system.
All in all, the understanding of a transient glacier system is developed. A valley, which over time and with climate fluctuations turns from a green valley with alpine agriculture such as cattle husbandry and trade routes across the passes into a large ice sheet, pushing farming activities to lower altitudes. And with recent continuous warming, experiencing again a rapid retreat of the ice to high altitudes.

8.1 Sampling Site and its Glacial History

The Jamtalferner, located in the Silvretta mountain range in south-western Tyrol in Austria at the border to Switzerland, is a glacier extending in the northern direction from the peaks of the Jamspitze at 3160 m a.s.l. down into the Jamtal valley (compare figure 8.1). Its glacier tongue is quickly retreating, in 2021 CE still reaching down to about 2430 m a.s.l. Fischer et al. (2016) reports that the glacier covered an area of

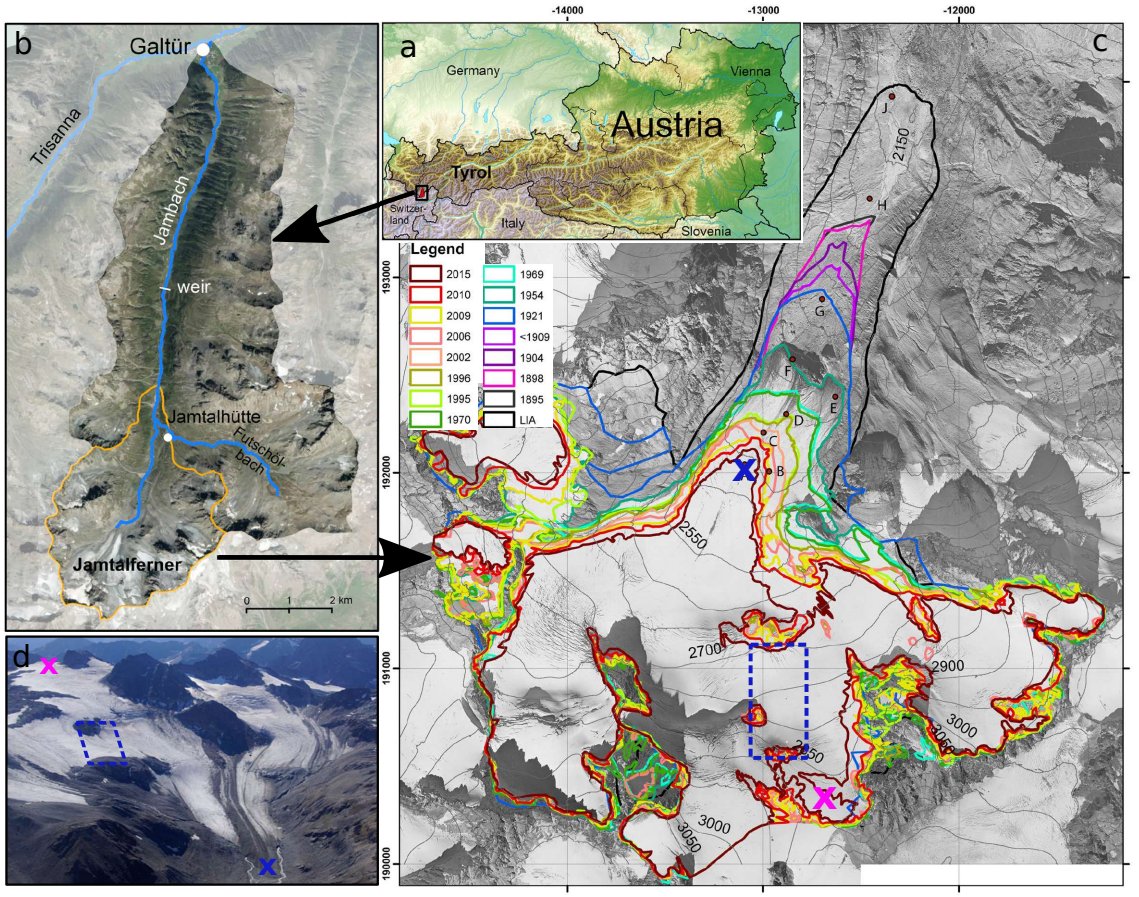

Figure 8.1: Overview of the Jamtalferner site. **a, b:** Overview of the location and the setting in the Jamtal valley (adapted from Hohensinner et al., 2021). **c:** Jamtalferner outlines over time, figure adapted from Fischer et al. (2019). The blue dashed rectangle indicates the area of interest shown in figure 8.2, the blue cross on the glacier tongue indicates, the approximate location of the lowermost sample, and the pink cross indicates the position of the Urezzajoch sample and wood finding (see main text). **d:** photo of the glacier valley from Hartl et al. (2020), with the same approximate location indications as in c.

2.07 km^2 in 2023 CE, having lost about 50 % of its area since 1969 CE and originally spanning about 6 km^2 at the local LIA maximum in 1864 (Fischer et al., 2019).
Historic data on the glacier can be found in several sources. Military surveys covering the area go back to 1820 CE (Hohensinner et al., 2021), while first length change monitoring commenced in 1892 CE. Orthophotos of the area were first taken in 1970 CE and since 1988 CE, the glacier mass balance has been monitored. This enables the contextualization of new results with many different historical sources and feeding them into the already existing understanding of the glacier system.
Several studies have been performed in the Jamtal in recent years and shed light on the glacial dynamics, and the resulting vegetation dynamics, and moraine record. Fischer et al. (2016) provides a time series of mass balance measurements since

1988 CE, Fischer et al. (2019) analyzed the changing vegetation in response to the glacier retreat in the valley from satellite data, and Hohensinner et al. (2021) shows an analysis of the land use and land cover change from 1820 CE to 2015 CE. A study on the reflectance of ice in the ablation zone of the glacier was conducted by Hartl et al. (2020). Other work, focussing more on the whole Silvretta area than only the Jamtal, was done by Fischer et al. (2021) who show the rapid retreat of glacier ice in the whole region. And, important for the ^{39}Ar moraine dating results in section 8.4, Braumann et al. (2021) conducted a moraine dating campaign in the Jamtal and a neighboring valley based on exposure dating with ^{10}Be.
The history of human activities in the Silvretta region and in particular in the Jamtal valley was studied by Huhn (1997), Dietre et al. (2014), and Reitmaier et al. (2013) who found archeological evidence from encampments dating back up to 6000-9000 a BCE. They argue that about 3000-4000 a BCE the original hunters and gatherers gave way to the first alpine farmers and shepherds. Human activity then increased in the region also in high altitudes until its peak around the mid-1800s (Hohensinner et al., 2021). Since then, human activities in higher altitudes are declining. Also, the century-old, close contact between the Engadin region in the south of the Silvretta mountains and the Paznaun region to the north has been documented by Huhn (1997). The mountain passes would frequently be crossed in the summer months to reach the summer Alps for the cattle, showcasing the direct impact of glaciation in the region on human activities.

8.2 Samples

In the 2021 CE sampling effort for ^{39}Ar dating, a section of the glacier was chosen that exhibits a very well-preserved layer structure at the surface, see the close-up section in figure 8.2. Different than in many other parts of the glacier, the summer (dark) and winter (bright) layers are well visible and not disturbed by any turbulence in the flow. The site was chosen, as the visible layers offer an opportunity to validate the ^{39}Ar age data with simple layer counting. On the other hand, as the age of the uppermost layer is not known, the ^{39}Ar data is necessary to determine the absolute age of the ice and to check for discontinuities (hiatus) in the ice records (e.g. due to larger melt events in the past).
An additional sample from the bottom of the 2021 CE glacier tongue was retrieved, as this location should provide older remaining ice of the ice flow.
The sampling was conducted by cutting large ice blocks from the glacier surface using an electric chainsaw. For each location, a large square was cut into the ice and divided into four quadrants, each of which was levered out with the help of an ice ax. This way, for each location four samples were cut from the glacier. In the end, one was left at each location, two were taken to Heidelberg for the ^{39}Ar analysis and the fourth one was taken to Innsbruck for further analyses for ^{3}H or ^{14}C. Thus, the samples of one location originate right next to each other. With the well-layered stratigraphy in this part of the glacier and the thickness of winter layers in the order of 2-3 m, there is no reason to doubt that samples from the same locations should

Table 8.1: Samples for ^{39}Ar analysis taken in 2021 and 2023. Samples kept in Innsbruck and designated for different analyses are italicized, measured samples are written in bold letters. The sample nomenclature is not intuitive due to a misunderstanding in the field. Altitude is given in orthometric height.

Location	Sample	GPS	Altitude [m a.s.l.]
JamA	**Jam58**, **Jam59**, *Jam60*, **CoreP3**	46°51'18"N 10°09'50"E	2790
JamB	Jam54, *Jam55*, Jam57	46°51'21"N 10°09'51"E	2769
JamC	Jam51, **Jam52**, *Jam53*, **CoreP2**	46°51'24"N 10°09'49"E	2742
JamD	*Jam2A*, **Jam2B**, Jam2D	46°51'26"N 10°09'48"E	2727
JamE	*Jam1A*, Jam1B, **Jam1C**, **CoreP1**	46°51'29"N 10°09'48"E	2708
JamF	Jam3A, **Jam3B**, *Jam3D*	46°51'52"N 10°09'38"E	2460
Urezzajoch	**Block A**	46°51'7"N 10°10'2"E	2864

have equal abundances for all tracers. They can therefore be treated as duplicates. Due to a misunderstanding in the field, the nomenclature of the samples turned out inconsistent, spanning the numbers 51 to 60 for the upper part, and the terms 1A to 3D for the lower part. Afterward, to clear things up, the locations were assigned the names JamA to JamF (from top to bottom) and the samples can thus be named with a combination of the location and the sample name, e.g. JamA_58. During the 2021 CE sampling, the weather was rainy and warm, which rendered ice core drilling impossible. It was therefore postponed to November 2021 CE, when ice cores from locations JamA, JamC, and JamE were retrieved. The purpose is to compare sampling methods and their potential bias of measured ages. The core samples were named CoreP1 to CoreP3 as listed in table 8.1 (P# referring to the number of the ablation stake ('Pegel') installed at this location).
In September 2023 CE, a large piece of human-processed wood was found on the Urezzajoch at the top of Jamtalferner. As this indicates human activities at this altitude and might therefore be evidence of the possible use of the mountain pass by humans, this piece was retrieved for a more detailed analysis and ^{14}C dating. To get an understanding of the ice cover at the time of deposition of the piece of wood, an ice sample close to the location was also taken for ^{39}Ar analysis.

8.3 Results

In the following, the measurement results of the samples from Jamtalferner are presented. Earlier versions of the ^{39}Ar data were already presented in the theses of Krastel (2022) and Marks (2024), which were supervised in the context of this thesis. In contrast to these earlier works, the measurements were now analyzed with the new data analysis method introduced in section 4.6, and the resulting ages corrected with the input curve introduced in section 4.6. This results in slightly different ages, however, not changing the key findings of the campaign. After showing the ^{39}Ar results, several other dating results on ice and other materials are presented.

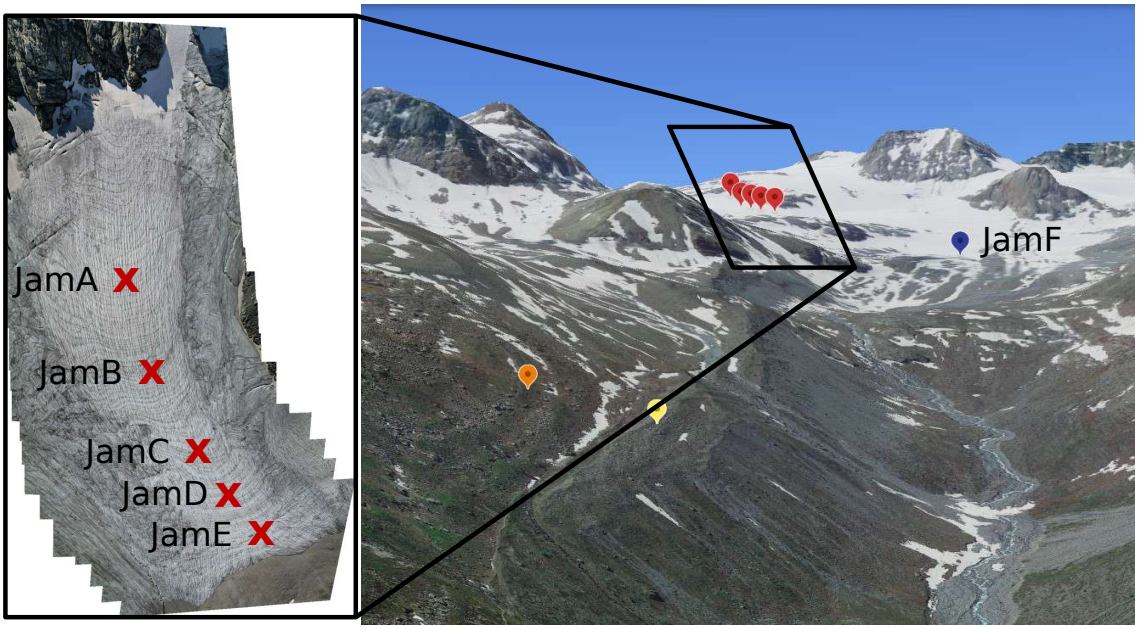

Figure 8.2: right: Overview of the glacier valley and the locations of the ^{39}Ar samples (red and blue markers), and the rock samples (yellow and orange markers). Note the well-visible edge of the LIA moraine just below the yellow marker. Figure adapted from GoogleEarth. **left:** close-up view of the layered section of the glacier, where the names of the ice sampling locations are given and their locations indicated by red crosses. Their locations are indicated only approximately, their exact GPS location can be found in table 8.1. On both sides of the layered part of the ice, the usual chaotic layer structure is visible. For the layered part, about 140 layers could be visually counted. The photo is stitched together from multiple drone photos taken during the 2021 sampling effort (courtesy A. Fischer and M. Stocker-Waldhuber).

8.3.1 ^{39}Ar Data

In table 8.2, the measured ^{39}Ar abundance and the resulting corrected ^{39}Ar ages are listed. Furthermore, the weight of each sample block or core, the resulted air-to-weight ratio, and the extracted amount of pure Ar are given. It is apparent that the sampling by cutting ice blocks from the surface of the glacier enabled the retrieval of large samples resulting in Ar contents per sample of sometimes several milliliters. Thus, several samples could be measured multiple times. Furthermore, as two samples were taken to Heidelberg from each sampling location, even if the amount of extracted Ar did not suffice for multiple measurements, these could be conducted with the duplicate sample.
In total, samples from 4 locations of the upper part plus the sample from the lower tongue were measured. Several of them 2 to 3 times. Furthermore, the ice block from the Urezzajoch was dated with ^{39}Ar.

Table 8.2: Overview of the ^{39}Ar measurement results. The sample names are combinations of the location and the sample name as stated in table 8.1. Age is given as input-curve corrected values following Happel (2024) as years before 2024. The weight of the ice samples, the ratio of extracted air to weight (air content), and the amount of extracted Ar are given.

Name	Weight [kg]	Air cont. [ml STP/kg]	Ar [ml STP]	^{39}Ar [pmAr]	^{39}Ar Age [a b. 2023]
JamA_58	5.0	27	1.2	86^{+19}_{-17}	70^{+95}_{-75}
JamA_59	4.5	30	1.4	76^{+24}_{-20}	127^{+118}_{-129}
JamA_comb58_59				82^{+15}_{-13}	99^{+71}_{-83}
JamA_CoreP3	2.4	35	0.7	80^{+16}_{-14}	104^{+79}_{-88}
JamC_52	4.8	68	3.0	74^{+19}_{-15}	142^{+89}_{-105}
JamC_52	4.8	68	3.0	78^{+18}_{-15}	121^{+86}_{-99}
JamC_comb52				76^{+12}_{-11}	132^{+64}_{-67}
JamC_CoreP2	1.8	45	0.7	74^{+15}_{-12}	137^{+70}_{-83}
JamD_2B	6.0	77	4.4	70^{+15}_{-14}	158^{+87}_{-81}
JamD_2B	6.0	77	4.4	86^{+19}_{-17}	76^{+95}_{-82}
JamD_2B	6.0	77	4.4	84^{+17}_{-15}	81^{+83}_{-87}
JamD_comb2B				78^{+10}_{-9}	116^{+48}_{-58}
JamE_1C	6.3	67	3.8	62^{+16}_{-13}	213^{+99}_{-92}
JamE_1C	6.3	67	3.8	78^{+19}_{-16}	121^{+92}_{-103}
JamE_comb_1C				70^{+12}_{-10}	164^{+61}_{-65}
JamE_CoreP1	2.1	53	1.1	86^{+17}_{-14}	76^{+76}_{-82}
JamF_3B	4.3	29	1.0	48^{+15}_{-14}	312^{+120}_{-110}
Urezzajoch_BlockA	4.5	11	0.5	46^{+12}_{-11}	333^{+99}_{-96}

8.3.2 Other Data

To complement the ^{39}Ar age measurements, parts of the ice blocks from the 2021 sampling campaign that remained in Innsbruck were sent to Seibersdorf Laboratories for ^{3}H analysis. The results are displayed in table 8.3. As indicated, the detection limit was at 0.5 tritium units (TU) and two of the three samples did not show concentrations above the limit. Only for sample JamA_60, the value was significantly above the detection limit, indicating the influence of past 1960s ice in the sample. Furthermore, the piece of human-processed wood (see photo 8.3) was ^{14}C dated at

the Vienna Environmental Research Accelerator, showing 97.66 ± 0.34 pmC which translates to an age range of 375 to 213 a cal BP with 76% certainty (see figure A.3, calibrated with OxCal v4.4.4).

Table 8.3: ^{3}H data measured at Seibersdorf Laboratories by liquid scintillation counting.

Sample	^{3}H [TU]	det. lim.
JamA_60	7.4±0.5	0.5
JamC_53	<d.l.	0.5
JamE_1A	<d.l.	0.5

Figure 8.3: Photo taken from the piece of wood and the neighboring ice patch in September 2023. The human-made grooves in the left piece of wood are visible. Photo by A. Fischer.

8.4 Surface Exposure Moraine Dating

Parallel to the work on the optimization and stabilization of the ATTA lab, the measurement of a variety of environmental samples (see table A.5), and the application of the ^{39}Ar dating tracer to glacier systems, many other projects were co-supervised during this thesis. One such topic was the growing idea of using ^{39}Ar as an exposure (or burial) dating tracer for rocks. It was kicked off by the very first samples measured during the author's time running the ATTA lab, which were permafrost samples from Svalbard. Initially very surprising, these samples showed ^{39}Ar abundances of up to 16 times atmospheric values. From these findings, the thesis by Hieronimus (2022) was motivated to calculate the first estimates of ^{39}Ar subsurface production. In the following, a master project was initialized to develop a gas extraction routine from rocks as well as a framework for the calculation of production rates and the analysis of the measured abundances. This project was conducted by Neumann (2024) and included rock samples taken from the same moraine locations which were exposure dated already by ^{10}Be in the work of Braumann et al. (2021) from the Jamtal. As

the topic of surface exposure dating was only peripherally supervised during this thesis and the focus was set on conducting the actual ^{39}Ar measurements of the rock samples, the principle and its results will only briefly be summarized here. For further details, please refer to Neumann (2024).

8.4.1 The Principle of Surface Exposure Dating

The principle of surface exposure dating with cosmogenic nuclides is based on their production by cosmic radiation. Cosmic radiation refers to highly energetic, electrically charged particles that enter the earth's atmosphere from space and cause showers of secondary particles onto the earth's surface after colliding with atoms in the atmosphere (for more details see Schaefer et al., 2022). Thus created cosmic neutrons can in turn produce isotopes like ^{39}Ar when hitting e.g. ^{39}K or ^{42}Ca in the ground or via another pathway, cosmic muons are captured by ^{40}Ca, ^{39}K or ^{44}K in the ground. Surface exposure dating exploits the fact that the production via these pathways declines with depth as the cosmic radiation only penetrates to a certain depth. In this case, the dominating production via cosmogenic neutrons only takes place in the uppermost few meters of the soil (or ice) (see also Musy and Purtschert, 2023). Therefore, a rock only starts accumulating high ^{39}Ar concentration once it is brought to the surface, either by geomorphological processes or e.g. a retreating glacier.
With this simple principle in mind, it is clear that it can be applied to the rocks that are transported by a glacier (during transport still covered from cosmic radiation by the ice) to its periphery and left there, exposed to cosmic radiation, as a moraine. Exposure dating can then put a date on the formation of such a moraine and thus on the maximum advance of a glacier.

8.4.2 Results for Moraine Ages in Jamtal Valley

Recently, a larger exposure dating study in Jamtal valley was conducted by Braumann et al. (2021), see figure 8.4. Different moraine formations were identified and dated with ^{10}Be. Along a well-visible inner moraine, ages of around 260 ± 20 a were measured. This indicates the formation of the moraine in the second half of the 18th century. Some boulders exhibit exposure ages of 1000 to 1500 a and were interpreted as moraine remnants of the neoglacial advance. On the outside of the LIA moraines, larger moraine structures showed exposure ages of around 11 ka, thus stemming from glacial retreat in the early Holocene. Also see figure 8.2, where the LIA moraine is well visible (location of JAM-18-18 indicated in yellow).
As a follow-up of their campaign, in 2023 CE, samples were collected from a subset of the same boulders as done by Braumann et al. (2021). With the precise ^{10}Be data at hand, this was a good setting for a first test of the discriminability of rocks that are expected to be at the ^{39}Ar secular equilibrium concentration and rocks that have been exposed to cosmic radiation for a shorter time. The boulders of the ^{10}Be samples JAM-19-21 and JAM-18-18 were resampled, providing the ^{39}Ar rock

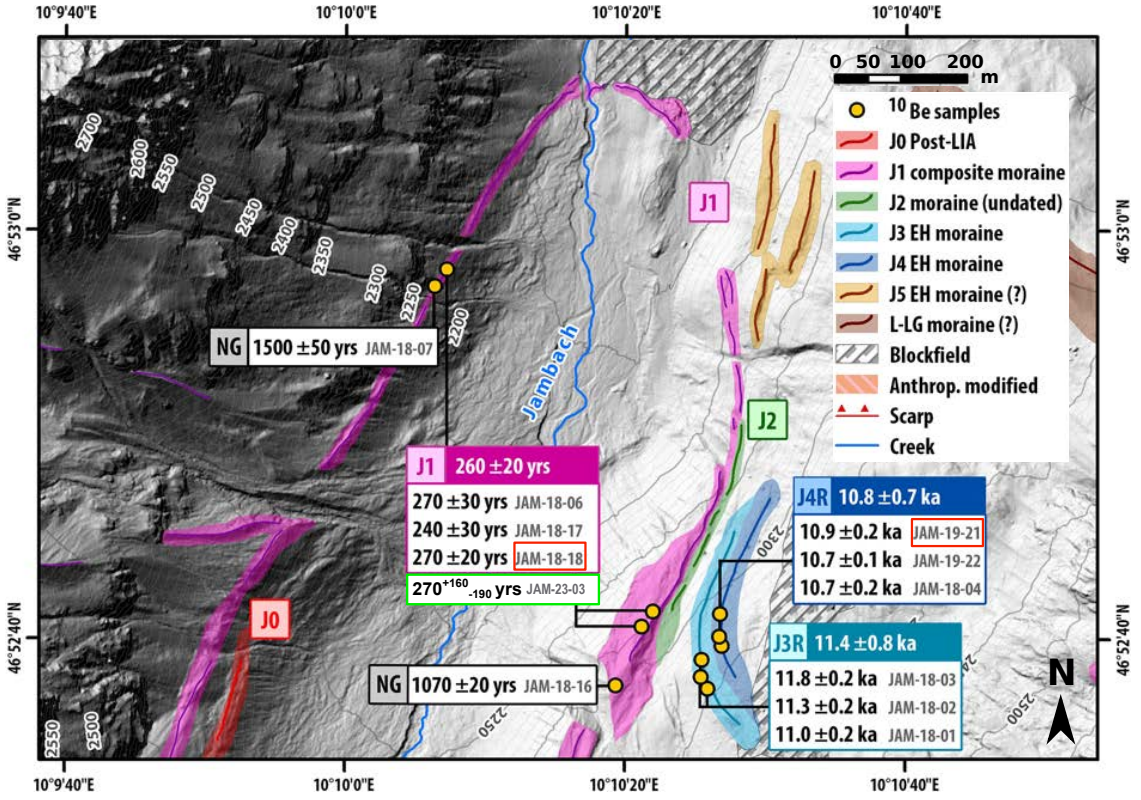

Figure 8.4: Overview map of moraine age data adapted from Braumann et al. (2021). The samples in red rectangles were resampled in Neumann (2024) for ^{39}Ar exposure dating. The sample from the same boulder as JAM-19-21 was used to calibrate the local production rate. Due to its long exposure derived from the ^{10}Be measurement, it can be assumed to be in secular equilibrium for its ^{39}Ar concentration, from which the production rate can be inferred. The result from the sample from the same boulder as JAM-18-18, referred to as JAM-23-03, was then calculated to an age of 270^{+160}_{-190} a, as indicated in the green rectangle. The location of samples JAM-19-21 and JAM-18-18 are also depicted in figure 8.2 as the orange and yellow markers, respectively.

samples JAM-23-05 and JAM-23-03 (location also indicated in figure 8.2 in orange and yellow, respectively). The results are shown in table 8.4. The exposure age for JAM-23-03, 270^{+160}_{-190} a does not significantly differ from its ^{10}Be equivalent with 270 ± 20 a, however, it exhibits very large uncertainties. The large ^{39}Ar errors are mainly caused by uncertainties in the production rate calculation, mainly attributed to the uncertainties of the interaction cross sections and the not well-determined extraction fraction of the gas from the rocks. For the latter, better methods are already in preparation and will lower the errors significantly.

Table 8.4: Summary of the relevant parameters for the ^{39}Ar exposure dating from Neumann (2024). Mass gives the mass of rock which was degassed for the measurement; $N_{^{39}Ar}$ the number of ^{39}Ar atoms in the sample, calculated from the measurement results. From this the concentration C^m of ^{39}Ar per gram of rock was calculated. Finally, by taking into account the local production rate and the extraction fraction of gas from the rock sample an exposure age for the non-equilibrium sample was calculated (for details see Neumann, 2024).

Sample	Jam-23-03	Jam-23-05
Mass [g]	155.45	139.86
$N_{^{39}Ar}$ [10^3 ^{39}Ar atoms]	211^{+25}_{-23}	1080^{+140}_{-120}
C^m [^{39}Ar atoms/g]	1360^{+160}_{-150}	7740^{+970}_{-890}
^{39}Ar age [a]	270^{+160}_{-190}	

8.5 Discussion

The Jamtalferner in the Silvretta mountain range in the Alps shows many signs of a glacier which in large parts is a transient phenomenon, highly affected by the climate conditions in the region. Here, different datasets will be discussed to better understand this history and to underline the variability of glacier extent in the Alps over time.

8.5.1 Consistency of ^{39}Ar Ages

The main dataset focussed on are the ^{39}Ar ages which cover parts of the glacier. For four out of the six locations that were eventually measured, several measurements could be conducted and their results combined. Therefore, as a first point, the agreement of the single measurements is discussed.
The results are displayed in table 8.2 and for better visual impression are plotted against the sample's altitude in figure 8.6. First looking at the agreement of the single block measurements, it is evident that they are all consistent within their 1σ errors. The combination of the single measurements to the combined result for each location was done within the analysis routine by combining the respective probability distributions and not by simply averaging the results given in table 8.2.
In figure 8.6, also the results for the core samples are displayed (in green). For locations JamA and JamC, the results from the ice blocks and the cores agree well within their errors. However, for location JamE, the core sample resulted in a slightly lower age just outside the 1σ range of the averaged ice block result. It is hard to judge, given the errors only being the 1σ range, this deviation could be a sign of a slight contamination during retrieval storage or extraction, or simply a statistical outlier.
The only location of which no sample was measured is JamB. It was omitted, as

measurement time is limited, and as the data from the other locations showed that the ages are so closely grouped that an additional sample would not have added much information.

Ice Blocks vs. Ice Cores

With the data at hand, no clear result can be presented for the consistency between ice block and ice core samples. The original reason for going back and taking ice core samples was to compare both sampling methods concerning their proneness to atmospheric contamination. However, with the young ages obtained from this part of the glacier, atmospheric contamination is hardly visible in the data, as it would shift the abundance further towards 100 pmAr, and most samples already lie within 2σ of 100 pmAr.
Another parameter to take into consideration is the yield of extracted gas per kg of ice. The values for each sample are given in the third column in table 8.2. While for the samples from JamC and JamE a slightly lower value for the core samples is evident, for JamA the core sample had a slightly higher Ar yield. Considering the large spread of Ar yield from sample to sample, the data does not provide evidence for any significant deviation in the Ar yield between ice blocks and ice cores.

8.5.2 Ice and Moraine Ages

Age Gradient in the Upper Section

All in all, from the ^{39}Ar data alone and with the given errors, no age trend can be detected for the upper samples. From the drone image (figure 8.2 left) approximately 140 layers were counted. This can be interpreted as a minimum age difference which should be expected between the uppermost and lowermost part of this section, as layers have potentially melted in the past in warmer time intervals. With errors of around 60-70 a, even for the combined results such a trend is hard to make out. Subtracting the combined results for the uppermost sample JamA_com58_59 and the lowermost sample of the upper section JamE_comb_1C results in 65 ± 96 a, again showing the non-significant difference between the two measured ages. This means that ^{39}Ar with its current precision is not able to resolve an age gradient here. However, one purpose of the ^{39}Ar dating of this upper section was to test if possible melt events in the past caused significant age jumps between layers, which were visually not evident. This in turn can be ruled out with the data at hand. A loss of more than 100 layers would increase the expected age difference between the uppermost and lowermost layer to approximately 240 a, which should then translate into a significant gradient also in the ^{39}Ar data.
The data becomes more insightful when adding the information gained from the ^{3}H measurements. Here, the data shows a clear difference between the location of JamA at the top and JamC and JamE further down. In figure 8.5, the ^{3}H measurement result for JamA from August 2022 CE is back-extrapolated with the radioactive decay law and the half-life of ^{3}H of 12.32 a (IAEA, a). Additionally, the long ^{3}H record

in precipitation from the Hohe Warte station in Vienna is shown for comparison (from IAEA, b). The decay curve intersects the data in the early 1960s and for longer periods in the 1970s and 2010s. Because the well-preserved annual layers from Jamtalferner justify the assumption of no considerable mixing, a straightforward interpretation can be made that the ice has precipitated as snow during these periods. With the strong mass loss in recent years, it is highly unlikely that ice formed in the 2010s, but much more probable in the early 1960s or 1970s, when the glacier still had mostly positive annual mass balances (Fischer et al., 2016). The two other samples, however, clearly consist of pre-1960 ice with ^{3}H concentrations below the detection level. These findings generally agree with the ^{39}Ar data, which is, however, not able to resolve the difference.

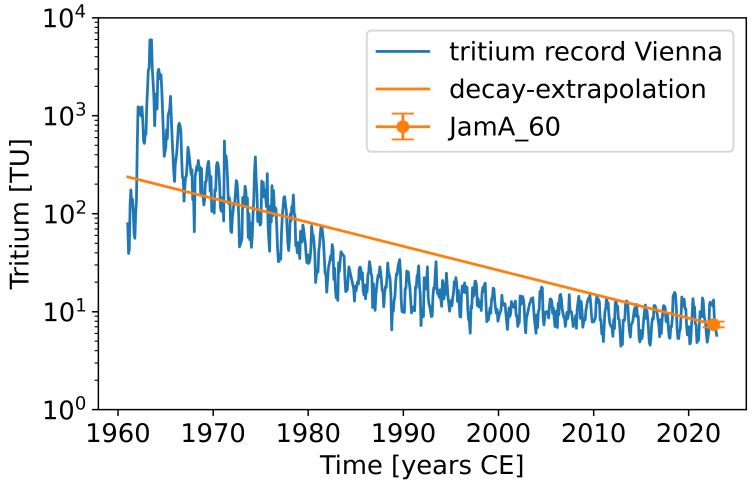

Figure 8.5: Decay extrapolation of the JamA_60 ^{3}H measurement in time (logarithmic plot). 7.4 ± 0.5 TU was measured in August 2022 CE. For comparison, the GNIP ^{3}H record from measurements station Hohe Warte, Vienna, Austria (IAEA, b). The extrapolated decay curve coincides with values in precipitation for the early 1960s and longer periods in the 1970s and 2010s.

In summary, the upper section in its entirety consists of ice which is less than roughly 200 a old. It does not exhibit any large age hiatus which means that no considerable melt event has taken place in this period. Furthermore, with ^{3}H clearly above the detection limit for the uppermost layers, it can be shown that the ablation situation across the whole extent of the glacier is only a recent phenomenon, as there has been ice formation after 1960 CE. This is corroborated by the Jamtalferner mass balance time series of Fischer et al. (2016) for which between the start of the measurements in 1988 CE until 2003 CE, only four years showed an equilibrium line altitude above the high point of the glacier, indicating throughout mass loss over the whole altitude profile of the glacier in these years. On the contrary, this means that in other years net mass gain occurred above the equilibrium line. Since 2003 CE, mass loss over the whole altitude profile of the glacier has been the case in 16 years.

Age of the Glacier Tongue

Primarily undertaken as a lucky guess as to where to find the oldest remaining surface ice, a sample was cut from the glacier surface at the lowest point of the glacier tongue present in September 2021 CE. The sample is displayed in figure 8.6 as the blue datapoint. With its ^{39}Ar age of 312^{+120}_{-110} a, it is significantly older than the ice in the upper section. With this age, it originates roughly from sometime between 1600 CE and 1800 CE, which coincides with the timing of the LIA and thus with the last large glacier advance. A single data point can of course not provide a full picture of a glacier system, however, it underlines the large advance the Jamtalferner has experienced during the LIA.

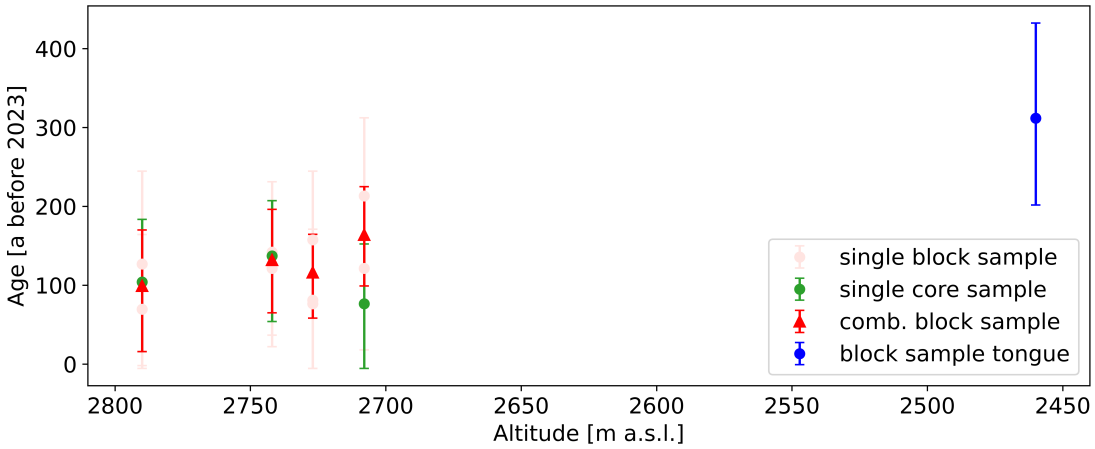

Figure 8.6: The ^{39}Ar age data plotted against the sample's altitude. The results from single ice block measurements are displayed in light red and their combined result in red. Green data points give the results from ice core samples. Finally, the blue data point is a single measurement from a block sample collected from the lower remaining part of the glacier (compare the map in figures 8.1 and 8.2).

Moraine Ages

The exposure ages for the innermost moraine in the Jamtal valley show ages around 270 a (Braumann et al., 2021). This means that the maximum extent of the glacier and with this the final formation of the moraine happened around 1750 CE. Again, this is consistent with the dynamics during the LIA, even though other publications mention a local LIA maximum in 1864 CE (Fischer et al., 2019). With the possibility of exposure during the transport, e.g. at the surface of the glacier, however, this bias should not be overinterpreted.
Aside from a few boulders which were part of the LIA moraine but dated to 1000-1500 a, according to Braumann et al. (2021) there is only a small visually noticeable moraine structure (J2 in figure 8.4) between the LIA moraine (J1) and the moraine from the early Holocene (J3, compare figure 8.4). The moraine in between could not

be dated due to the lack of suitable boulders. However, the lack of further and more obvious moraine structures shows how unprecedented the glacial advance during the LIA was compared to the entire rest of the Holocene, as it seems to have overwritten them.
Thus, the moraine data corroborates the ice data in the sense that a comprehensive image is drawn of a glacier that experienced a large advance around the end-1700s to mid-1800s, after a time when it covered a probably significantly smaller area. Thus, most of the surface ice in the lower sections of the glacier and the obvious innermost moraine structure originate from this period.

8.5.3 Impact of Glaciers on Human Activities

In the following, a short comment will be made on the interplay of the Jamtalferner and the human activities that have been evident in this region for many millennia. However, as this aspect is not the focus of this thesis nor the expertise of the author, this will be very qualitative and only for the sake of some social geographical context.
During the monitoring of the Jamtalferner, in September 2023 CE, a large piece of human-processed wood was found at the Urezzajoch, at the top of the Jamtalferner. With only the peaks of the surrounding mountains towering above, this piece of wood can only have reached this place by human activity. With archeological studies as done by Reitmaier et al. (2013) and Dietre et al. (2014) as a background, it is likely that the passes in the Silvretta have a long history as trade routes between the different valleys. Finding direct proof of human activity at this location shows the effect of the extent of the Jamtalferner on such activities. The piece of wood was ^{14}C-dated to an age range of most likely 375 a to 213 a (compare figure A.3), which corresponds to about 1650-1810 CE. Furthermore, to not repeat the mistakes made during the retrieval of the Tyrolian Iceman, where none of the surrounding ice was sampled, an ice block from a directly neighboring small ice field remaining in a depression was retrieved as well (compare figure 8.3). The ice sample, labeled 'Urezzajoch_BlockA', was ^{39}Ar dated to an age of 333^{+99}_{-96} a. The ice thus shows a very similar age as the wood itself.

The paper by Hohensinner et al. (2021) claims that 'until the early 18th century, the Jamtalferner could still be crossed with horses' (based on Böhm, 1970). Following this information, there was so sparse ice at the mountain pass until the early 1700s that it was still crossed by humans. This would fit the picture of a much smaller ice extent prior to the LIA and a subsequent glacial advance at the mountain pass archived in the piece of basal ice from 1690 CE (1σ range: 1591-1786 CE).
Altogether, the data is very sparse, and exact details can only be speculated. However, all data seem to suggest a much smaller glacial extent in the Jamtal valley before the LIA, after which a strong advance of the glacier took place until the mid-19th century before a strong retreat of the glacier commenced which is ongoing and accelerating today.

8.6 Summary and Outlook

The presented data gives evidence of a glacier system at low altitudes which is highly affected by the varying climate. Thus, over time it has experienced strong advances and retreats. With only a handful of data points to cover the large expanse of the glacier, a comprehensive picture can hardly be drawn. Nevertheless, the different tracer datasets agree in describing a glacier with mostly young ice, which is very quickly retreating, after experiencing a strong advance during the LIA. The moraine ages from ^{10}Be data from Braumann et al. (2021) as well as first results of ^{39}Ar exposure dating corroborate this. So far, the latter does not provide much new information, however, in a scenario like in the Jamtal, the ^{39}Ar tracer for surface exposure or burial dating can play a unique role. In contrast to most other commonly used cosmogenic nuclides which have half-lives of $> 10^5$ a (compare Schaefer et al., 2022), ^{39}Ar has a half-life of only 268 ± 3 a. Therefore, it can be used as a burial tracer on the timescale of centuries. A future effort could e.g. sample rock from locations, where the glacier tongue has just retreated. By measuring the abundance, the burial time can be calculated and thus possibly provide important information on the extent of the glacier before the LIA.
Another interesting path to pursue to gain a better understanding of the glacier system is the drilling of ice cores to bedrock to understand the vertical age distribution. This has already been done at the top of the Jamspitze and ^{39}Ar measurements at the surface and bottom of the ice core are planned. A first ^{14}C measurement by the Paul-Scherrer Institute from a depth of 15.60-16.25 m showed ages of 511-711 a. This would indicate higher ages at the top than those found at the bottom of the glacier, agreeing with a possible glacial retreat to higher altitudes before the LIA. However, it could also be interpreted as stagnant ice at the summit, like the old ice found at the WSS summit (discussed in chapter 7). Such ice would not be expected to make its way down to the glacier tongue. Measuring more ^{39}Ar and ^{14}C samples of this ice core would give a better understanding of the upper part of the glacier and the question if the Jamspitze was entirely ice-free at some point during the Holocene.
The relentlessness with which the Alpine world is changing due to a warming climate, especially at such lower altitudes, was emphasized by a massive landslide in June 2023 CE which happened at Fluchthorn, another peak on the outskirts of the Jamtal valley, and just 4 km away from the Jamtalferner. Probably due to the destabilization of the mountain by melting of the permafrost or retreating glaciers, 1 million cubic meters of rocks broke off the peak of the mountain, lowering its peak by 19 m.

9 Gas Extraction from Continuous Flow Analysis

The preceding chapters have shown that ^{39}Ar-dating of ice can contribute valuable age information to various glacial settings. Furthermore, the two radioactive Kr isotopes ^{81}Kr ($T_{1/2} = 229\,\text{ka}$) and ^{85}Kr ($T_{1/2} = 10.7\,\text{a}$), which are also measured with ATTA, cover very different age ranges (see figure 2.1) and are valuable tracers for ice dating (Buizert et al., 2014; Tian et al., 2019; Ritterbusch et al., 2022). While the required amount of gas for measurements has been drastically reduced for all three tracers, it still amounts to about 100 ml for ^{39}Ar and ^{81}Kr. Depending on the air content in the ice, this can require several kilograms of ice (compare tables 7.1, 8.2). However, such amounts are sometimes problematic to dedicate solely to a single dating measurement. In the current routine (see section 4.2) the whole ice sample is melted and, thus, lost for most other analyses. This becomes especially critical for valuable ice obtained from locations where the amount is limited but ideally, multiple analyses are performed, e.g. Antarctic ice cores.

To overcome this high ice demand for a single ATTA measurement which has to compete with other analyses, as part of this thesis, a project was started to test the extraction of gas from the routinely conducted *continuous flow analysis* (CFA) for offline ATTA measurements. CFA is a method in which a longitudinal subsection of an ice core stick (usually quadratic, $\sim 32 \times 32\,\text{mm}$) is continuously melted along its axis and the resulting water flow is in through-flow analyzed for a variety of tracers. By staying at low melt speeds (a few cm per minute) and ensuring small volumes and small tubing ($< 1\,\text{mm}$ inner diameter), any mixing due to dispersion in the tubes is kept low and thus high spatial resolution is achieved. Over time, the measurements connected to a CFA melting system have been extended including measurements of major ions, trace metals, stable water isotopes, dust particles etc. (Röthlisberger et al., 2000; McConnell et al., 2002; Kaufmann et al., 2008; Bigler et al., 2011; Dallmayr et al., 2016). Also, gas species like methane have been measured online with CFA systems (Schüpbach et al., 2009; Stowasser et al., 2012; Rhodes et al., 2013) by connecting a gas chromatograph (GC) or a laser spectrometer. However, it has not been established as a routine capability. Thus, for most CFA systems the gas from an ice core is discarded.

Establishing a method of sampling the gas from CFA for a later ATTA measurement would thus achieve a symbiosis of a routinely applied analysis with a measurement that would otherwise often be abstained from due to its large consumption of sample ice. The challenges are mainly related to the gas tightness of the system. As the CFA systems have usually not been designed for gas analysis, possible contamination

by atmospheric air either at the melting unit or in the different components of the tubes and the debubbler have to be checked.
In the following, the technical setup of a CFA system and the gas extraction unit, designed as part of this thesis, are discussed. Subsequently, the different tests to determine the gas tightness of the system and its gas extraction capabilities are presented. First results, obtained from the CFA-coupled gas extraction of an Antarctic ice core are presented and their implications for atmospheric air contamination as well as interpretations towards gas age-ice age differences are discussed. Finally, an outlook is given to optimizations of the gas extraction unit and possible applications.

9.1 Setup of a CFA and the Gas Extraction Unit

In figure 9.1, the simplified technical setup of a CFA system and the gas extraction unit, designed as part of this thesis, are depicted. On the left, the melting system with the ice core section on the melt head is shown. The meltwater flow is divided into an outer (potentially contaminated), and an inner (not in contact with atmospheric air) part. With the constant melting of the outer part, a liquid water film should always be present between the melt head and ice such that the inner part is sealed from any atmospheric air in the lab.

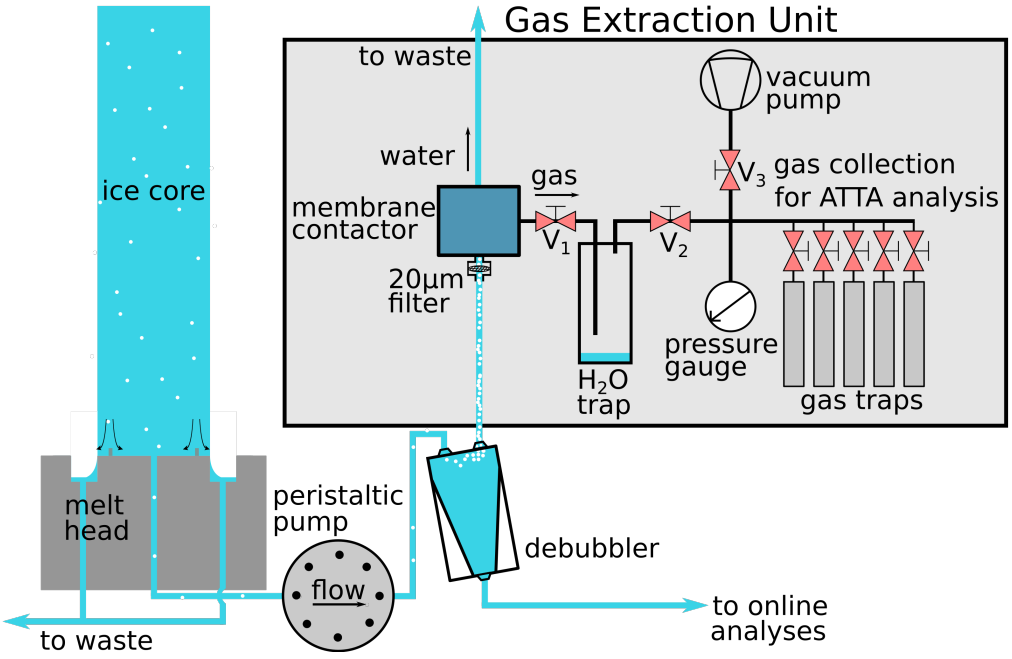

Figure 9.1: Schematic of the CFA setup and the connected gas extraction unit. The water trap consists of a stainless steel cup filled with steel wool and is cooled to $\sim -89^\circ$ C by a liquid nitrogen-isopropanol mixture. The gas traps are filled with activated charcoal and are cooled with liquid nitrogen to $\sim -196^\circ$ C. For details see main text in section 9.1.

A peristaltic pump controls the flow speed, while the temperature regulation of the

melt head controls the melt speed. Subsequently, a so-called *debubbler* is integrated into the flow. It removes the bubbles from the main flow that goes to the online analyses of the CFA system where bubbles would compromise the measurements. Due to their buoyancy, the bubbles enter the upper line that was originally directed to the waste. With the gas extraction unit, the gas from the bubbles is extracted with a membrane contactor (3M™ Liqui-Cel™ MM-0.5x1 Series), the same membrane contactor as employed by Stowasser et al. (2012) and Rhodes et al. (2013), with the former name *G591*.
Because the extracted gas still consists to a large fraction of water vapor, the humidity in the gas is frozen in a water trap (stainless steel cup with steel wool, cooled to $\sim -89^\circ$ C). The remaining gas is eventually transferred to liquid nitrogen-cooled activated charcoal traps. These sample holders can be connected to the usual purification setup introduced in section 4.2 to purify Ar and Kr.
The connections to the 1/4" straight tube connectors of the membrane contactor are implemented with Swagelok® Ultra-Torr vacuum fittings. On the water side, the Ultra-Torr vacuum fittings are connected to 1/16" metal tubes onto which the silicone tubing of the CFA can be squeezed. On the gas side, the two arms of the membrane contactor are joined and connected to traps, as shown in figure 9.1 and 9.2b),c).
The gas extraction unit includes several valves, indicated as V_1, V_2, and V_3 in figure 9.1. V_1 enables the disconnection of the gas extraction unit from the membrane to evacuate it before sampling. V_3 is used to connect or disconnect the vacuum pump from the setup, depending on whether the system is being evacuated or sample gas is trapped on the gas traps, respectively. V_2 can be closed for a preliminary check of the gas amount in one of the traps. With a calibrated volume between V_2, V_3, and a gas trap (all but one are closed), the reading on the pressure gauge provides a first estimate of the gas amount on the trap.

9.2 Extraction Procedure

The general mode of operation of the gas extraction unit is summarized in the following. Before the melting of an ice core starts, the gas extraction unit is evacuated. V1 is closed, V2 and V3 are open. The gas traps have been evacuated beforehand and are all closed. When the melting commences, the water trap is cooled to -89° C and V1 is opened once the membrane contactor is filled with meltwater, this way all remaining gas in the membrane contactor is evacuated, typical pressures reach about 0.1 mbar in the gas extraction unit. After about 1-2 minutes, the system is well flushed and the gas can be trapped. For this, V3 is closed and one gas trap is cooled with liquid nitrogen and opened. Thus, all extracted gas is frozen in the trap. Typical pressures during the sampling are ∼1-3 mbar, with a visible increase when bubbles enter the membrane contactor.
The ice core sections are typically 1 m in length but can comprise cracks. Once a transition between ice core sections or cracks reaches the melt head, the liquid film sealing the inner part of the ice core from atmospheric air can be interrupted,

a) b) c)

Figure 9.2: a) Photo of the debubbler. Water and bubbles enter on the upper left, pure water exits at the bottom, and overflow water and bubbles exit at the upper right. **b)** Overview-photo of the gas extraction unit as schematically depicted in figure 9.1. **c)** Membrane contactor 3M™ Liqui-Cel™ MM-0.5x1 Series with the water side connected vertically and the gas side connected horizontally with Swagelok® Ultra-Torr Vacuum Fittings.

potentially enabling surrounding air to be sucked into the inner line. Therefore, attention has to be paid that the gas trap is closed once a transition or crack reaches the melt head or in case the ice core gets stuck in the melting system. By simply closing the valve of the trap and opening V3, the potentially contaminated air can be evacuated. Once the melting is in normal operation again, about 30 s of delay is waited to evacuate all remaining air before V3 is closed and the gas trap opened again.
The CFA system is running in a continuous mode, meaning that during the melting of one ice stick the next one can be put on top without interrupting the melt procedure. Therefore, each gas sample can consist of several ice sections with the corresponding number of transitions.
The gas extraction unit currently includes up to five gas traps. Having these already connected enables the switching to the next trap at predetermined depth intervals of the ice core or when a trap is full.

9.3 First Tests

In order to test the gas extraction unit in a CFA setup, three melting campaigns were conducted. In November 2022 CE, a first test was conducted at the Institute of Polar Sciences (ISP) at the Ca' Foscari University, Venice. The objectives of this first campaign were mainly to test how to connect the gas extraction unit to the existing CFA system and identify possible improvements. Also, a first attempt of the quantification of the potential contamination with atmospheric air by gas

volume measurements was planned. The tests and outcomes are in detail discussed in Urbach (2023) and are only briefly summarized here. To protect the membrane contactor from dust particles in the meltwater, different types of filters were tested. First conclusions were drawn regarding the dimensions of the water side part, the volume of which has to be minimized to ensure a quick through-flow of the sample gas and, thus, no mixing between the sample and subsequent contaminated gas, e.g. from a transition, in stagnant volumes. The through-flow time and mixing between water from consecutive ice core sections were analyzed by installing electrical conductivity sensors before and after the membrane contactor (and its upstream filters). Consecutive melting of ice from tap water and from desalinated, purified water gave a clear and steep change in the signal before the membrane. With the delay of the signal behind the membrane and the decrease in the slope of the conductivity change, the timing of the through-flow and the mixing were evaluated and optimized.
Furthermore, in a first attempt to extract gas from glacier ice, ice sticks from leftover samples from the Jamtalferner campaign (compare chapter 8) were melted and the gas extracted. Urbach (2023) conducts a detailed analysis of the expected and obtained gas amounts. Ongoing problems of the CFA system, due to clogging of the tubes and problems with the melt head, resulted in some of the obtained gas samples presumably consisting of larger fractions of atmospheric air. However, the comparison of expected and obtained gas amounts proved inconclusive for a quantification of the contamination. Also, measurements of CFCs, which would also be a sign for modern air contamination (see the ages for Jamtalferner samples in chapter 8), proved inconclusive, possibly because the water trap freezes all CFCs before they enter the gas trap.

With the knowledge gained in the first campaign and some optimizations to the setup, a second test of the gas extraction unit with the CFA at ISP, Venice was conducted in September 2023 CE. After having shown the general feasibility of the gas extraction, the focus was set on the quantification of atmospheric air contamination. With the noble gas mass spectrometer available in the research group in Heidelberg, the idea was developed to add an inflow of Ar gas from a bottle to the freezer in which the ice core section and melt head are placed. By doing so, the air in the freezer is enriched in Ar and any seeping in air at the melt head could thus be detected with elevated Ar abundances in the gas sample, the measurement of which can very precisely be conducted in the noble gas mass spectrometer lab at the IUP in Heidelberg. Furthermore, also tube connections were wrapped in plastic bags and flooded with Ar to detect any leakage into the tubes. To double-check the functioning of this method, ice sticks with large cracks were prepared, melted, and the gas extracted with the added Ar flow to show that contamination by surrounding air is detectable. Marks (2024) includes a more detailed analysis of the results and the plots of the noble gas concentrations are attached in figure A.5. Unfortunately, even the leaky samples did not show strongly increased Ar concentrations, which puts into question the significance of the test, and further evaluation of the quantification of intruding atmospheric air was not possible. The reason for this failure is probably that the Ar supply at ISP was very limited and therefore the inflow into the freezer was set too

low to produce any detectable signal.
Based on the first tests, an internal report was registered at the Institue of Polar Sciences, Venice (Spagnesi et al., 2023b).

9.4 CFA Analysis and Gas Extraction of an Antarctic Ice Core

In September 2024 CE, the opportunity arose to couple the gas extraction unit to the CFA at the Alfred-Wegener-Institute (AWI) in Bremerhaven to test a real gas extraction with subsequent ATTA analysis. A section of the 204 m long ice core B56 from the East Antarctic Plateau was analyzed with the CFA system. Details on the coring location and data from the ice core can be found in Sagol et al. (2024) and Weinhart et al. (2020). From the mean density of the ice section, the pore close-off depth at the density of 830 kg/m^3 (Cuffey and Paterson, 2010) was determined to a depth of 95.57 ± 3.3 m (Sagol et al., 2024; Baumbusch, in progress).
The objectives for the gas extraction campaign were the following: First, check the gas tightness of the system by melting bubble-free ice (which was obtained from an ice-sculpturing workshop) and checking for any obtained gas. Second, perform the gas extraction during the CFA analysis of the ice core, optimize the setup, and test how much gas is obtained per meter of melted ice. Third, measure the ^{85}Kr content of the gas to quantify the amount of atmospheric air that entered the system. ^{85}Kr is anthropogenic and has a half-life of 10.7 a, its abundance in old ice should therefore be zero. With a known atmospheric abundance any increased amount of ^{85}Kr can then be translated into a relative contamination. Fourth, measure ^{39}Ar abundances and corresponding ages to determine the gas age-ice age difference (Δage) in the ice core.
The pores in the firn above the pore close-off depth are in theory still connected to the atmosphere and therefore should show modern signatures. Thus, to perform the mentioned objectives, only ice from below the pore close-off depth was used for the gas extraction. Figure 9.4 shows in blue the age-depth timescale for the lower (below pore close-off depth) part of the B56 ice core derived in Sagol et al. (2024). It is based on absolute age markers from known volcanic eruptions and ash layers, as well as sea-salt and sulfate measurements. Furthermore, the figure depicts in green the depth intervals that were sampled. In total seven gas samples were taken. In table 9.2, the samples and their respective depth intervals, lengths, and also gas yields are listed.
During the melt campaign in the CFA lab at AWI, melt speeds were typically stabilized to about 3 cm/min. With an area of 26x26 mm of the inner section of the melt head, this amounts to a meltwater flow of about 20 ml/min. To ensure a well-sealed inner section of the melt head, less melt water was pumped from the inner part than was melted by setting the peristaltic pump to a speed of 12-13 ml/min.
The campaign at AWI was conducted together with a bachelor student as part of her bachelor thesis, where more of the details on the different tests and results can

be found (Baumbusch, in progress).

9.4.1 Results

To address the first objective, bubble-free ice was melted with the CFA system and the resulting trapped air on the gas trap was checked. The results are listed in table 9.1 and show gas yields an order of magnitude lower than in the glacier samples.

Table 9.1: Results of the CFA gas extraction from bubble-free ice. The relative gas yield was calculated by comparing the gas yield in the bubble-free sample to a real ice sample, for details see main text.

Sample	Length [cm]	Air [ml STP]	Gas yield [ml STP/m]	Rel. Gas yield [%]
Bubble_Free_1	171.7±1.8	0.51±0.07	0.30±0.04	1.70±0.24
Bubble_Free_2	97.3±1.0	0.14±0.06	0.14±0.06	0.49±0.21

To address the second objective, the amount of extracted gas was checked after each sample section. The first sample which was extracted was sample B56_144_148. During this first run, the pumping speed of the peristaltic pump was set to 9-10 ml/min, which is enough flow for the CFA analysis without gas extraction. With a melt speed of 3 cm/min, this resulted in a larger overflow to the outer section of the melt head (compare figure 9.1) and, thus, an unnecessary loss also of sample air. The significantly lower gas yield per meter of ice can be seen in table 9.2. After noticing this, the pump speed was increased to 12-13 ml/min, resulting in larger gas yield values. With an air extraction of around 30 ml STP/m, about 3 m of ice core are needed to obtain the 100 ml STP of gas needed for ^{85}Kr, ^{81}Kr, and ^{39}Ar analyses.

For an additional and more quantitative analysis of the air contamination of the samples, the third objective of the campaign, the measurement of ^{85}Kr was planned. As the capabilities of an ^{85}Kr analysis, especially with low gas volumes, are still being implemented in the Heidelberg ATTA facility, the analysis was done in cooperation with the ATTA group at the University of Science and Technology of China (USTC) at their laboratory in Hefei, China. From each gas sample, Kr and Ar were extracted and purified such that for each sample ^{85}Kr as well as ^{81}Kr and ^{39}Ar abundances can be measured. The results for ^{85}Kr are given in table 9.2 and are plotted in figure 9.3. The abundances are given in percent relative to the atmospheric reference sample 'Bremerhaven Air', which was taken for this purpose in the CFA laboratory at AWI.

To address the last objective, the ^{39}Ar abundance of a first sample, B56_109_113, has been measured at USTC as well. It resulted in 23 ± 3.2 pmAr which translates to an age of 580^{+58}_{-42} a.

Table 9.2: List of the gas samples taken during the CFA melting campaign of the B56 ice core. The respective depth intervals, lengths, and gas yields are listed as well as the results of the ^{85}Kr analysis. The sample 'Bremerhaven Air' is an air sample from the CFA laboratory at AWI that was taken as the atmospheric reference. Data for length, contained air amount (air), and air per meter of ice (gas yield) are taken from lab notes and their analysis in Baumbusch (in progress). The length was corrected for the times during which the gas trap had to be closed after transitions and cracks (see section 9.2).

Sample Name	Depth [m]	Length [cm]	Air [ml STP]	Gas yield [ml STP/m]	^{85}Kr [dpm/cc]
B56_99_102	99-102	250.4±2.6	77.2±2.3	30.8±1.0	2.94±0.24
B56_102_106	102-106	330.1±3.3	106.6±3.2	32.3±1.0	2.18±0.19
B56_106_109	106-109	279.0±2.8	90.1±2.7	32.3±1.0	1.32±0.29
B56_109_113	109-113	332.4±3.4	90.5±2.7	27.2±0.9	1.07±0.21
B56_113_116	113-116	256.1±2.6	70.3±2.1	27.5±0.9	
B56_116_120	116-120	354.2±3.6	95.4±2.9	26.9±0.9	0.96±0.22
B56_144_148	144-148	346.1±3.5	60.3±1.2	17.4±0.4	
Bremerhaven Air			59.9±1.8		78.12±3.43

9.4.2 Discussion

Gas Yield

A first unknown of the gas extraction from the CFA of glacier ice was the gas yield which would be achieved. A more thorough evaluation taking into account the higher pressures in the bubbles in the ice, their temperature, and the density of the sample ice will be presented in Baumbusch (in progress). Here, a simplified evaluation is presented only to roughly estimate the extraction efficiency of the setup. Cuffey and Paterson (2010) state that for polar ice, the air content in ice can be expected to be about 10% in volume. In a simple calculation with an inner melt-head area of 26x26 mm and an air content of 10%, a ∼1.5 m long section of an ice core is needed to obtain 100 ml STP of air which would be a gas yield of ∼67 ml STP/m. The results in table 9.2 show that during the extraction a bit less than 50% of that value was obtained and with this about 3 m of ice core are required for a sample. Partly, this can be attributed to the fact that not all melt water (and with this all bubbles) is pumped into the inner tube by the peristaltic pump, as the pump speed is kept below the melting speed to ensure a well-sealed inner part of the melt head. In this case, of the melted 20 ml/min only 12 ml/min were pumped into the debubbler. This factor alone decreases the expected gas yield from 67 to ∼40 ml STP/m.
Another factor that could lead to a decreased gas yield is the solubility of gases in water and the extraction efficiency of the membrane contactor. This question was addressed in the bachelor thesis by Urbach (2023), which was supervised in the scope of this thesis. It addresses the extraction efficiency of Ar from air-equilibrated water by the membrane contactor. The results all show efficiencies not significantly

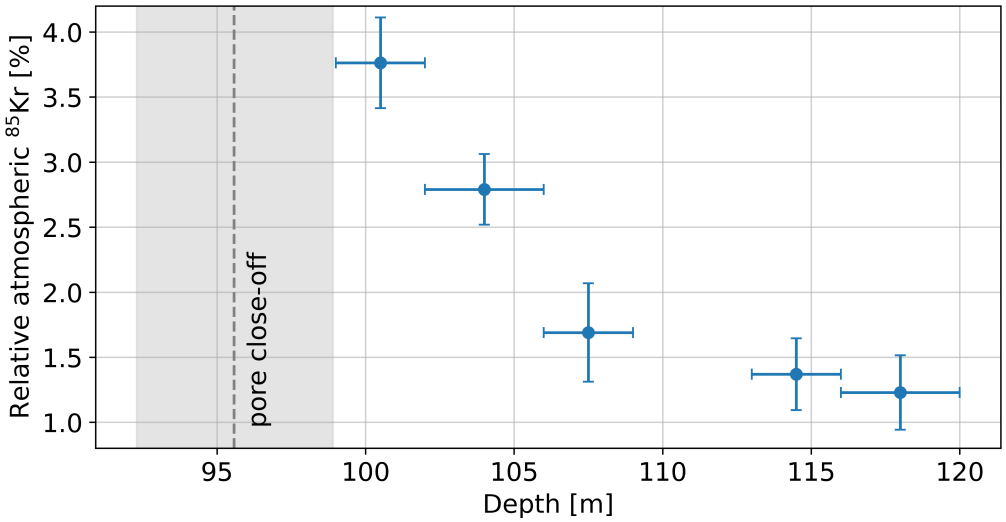

Figure 9.3: ^{85}Kr abundances vs. depth given relative to the atmospheric sample 'Bremerhaven Air' with 78.12 ± 3.43 dpm/cc (see table 9.2).

deviating from 100%, however, parts of the melt water flow towards the online analyses and do not pass the membrane contactor, thus, potentially leading to a small gas loss.
Other potential reasons for a lower gas yield are discussed in Baumbusch (in progress), including the stronger gas loss at lower pump speeds, potentially indicating a preferential loss of gas relative to water through the flow from the inner towards the outer part of the melt head.
All in all, the required 3 m of ice core per sample provides a reasonably good resolution and should not limit the application of this gas extraction method.

Atmospheric Air Contamination

The quantification of potential atmospheric air contamination of the extracted gas was a major objective of this campaign. Two approaches were conducted to obtain data. First, bubble-free ice was melted with the CFA, and the gas extraction was conducted as usual. From the obtained gas, which should not stem from the ice itself, the contamination can be quantified. As a first step, the bubble-free ice was melted in the usual bucket for gas extraction from ice (see section 4.2), and its air content was quantified. It resulted in 0.04 ml STP/kg (ml STP air per kg of ice, which translates to a total of approximately 0.024 ml STP/m, ml STP air per m of CFA ice stick, not considering loss through the channels mentioned above). In the CFA lab at AWI, two sticks of bubble-free ice were melted and their gas was frozen in the gas traps. The first sample, Bubble_Free_1, was melted with the lower pump speed of 9 ml/min and consisted of 8x24 cm pieces, so that the test incorporated transitions and is, thus, very close to the real sample melting scenario. The second sample, Bubble_Free_2, was melted at the higher pump speed of ∼13 ml/min but only consisted of one 1 m piece without transitions or cracks. Table 9.1 summarizes

information on the two samples and the amount of air extracted. It can be noted that the gas yield of ∼0.024 ml STP/m of the bubble-free ice (see above) is an order of magnitude lower than the gas yield obtained from the bubble-free ice when melting with the CFA (see table 9.1). This means that the extracted gas during the CFA melting of the bubble-free samples originates from atmospheric air that entered the CFA system during sampling, e.g. due to tube connections that are not entirely gas-tight, due to an imperfect sealing between the melt head and ice core or due to a too short flushing time of the membrane contactor after transitions between ice sticks.
To quantify the amount of seeped in atmospheric air into the CFA system, the air extracted from bubble-free ice is put in relation to the amount of air extracted from a real sample under similar conditions. To do so, the gas yield of sample Bubble_Free_1 is divided by the gas yield of sample B56_144_148, as both were melted with a lower pump speed. The sample Bubble_Free_2 was evaluated in relation to the mean gas yield of samples B56_99_103 to B56_116_120, as they were all melted with the same higher pump speeds. The resulting relative gas yield is given in the right column of table 9.1 and results in $1.70 \pm 0.24\%$, respectively $0.49 \pm 0.21\%$. Because the different pump speeds are already corrected for in the relative values, the obvious alteration in the melting procedure which can explain the significant difference between the two relative gas yields is the number of transitions in the samples. While Bubble_Free_1 had 7 transitions between 8 short pieces of ice, Bubble_Free_2 only consisted of one large piece, which makes the value from the first sample a more realistic estimation. As described in section 9.2, the potential atmospheric air that enters the inner CFA part at the transitions enters the membrane contactor and is flushed out by closing the gas trap and opening the gas extraction unit to the vacuum pump for a certain time. It seems that this procedure successfully suppresses atmospheric air contamination down to 1-2%, however does not prevent it entirely. For future campaigns, this is an aspect which should be improved. In the outlook in section 9.5, an idea is put forward that could eliminate this issue.

The second approach was to measure the ^{85}Kr abundances in the gas samples. With its low half-life of 10.7 a there should not be any ^{85}Kr in the ice well below the pore close-off depth. Atmospheric values are around 80 dpm/cc (78.12 ± 3.43 measured in Bremerhaven air as part of this campaign). Any increased ^{85}Kr abundances in the gas samples of the lower ice sections can therefore be attributed to atmospheric contamination. The results are listed in table 9.2 and plotted in figure 9.3 and show values of 1.0-1.5% of atmospheric ^{85}Kr for the samples below 110 m and can be interpreted as indicating an atmospheric contamination of this magnitude. This agrees well with the findings of the bubble-free ice tests.
Samples B56_99_102 and B56_102_106 show significantly higher ^{85}Kr abundances. As these samples are from depths close to the pore close-off depth, this is interpreted as an influence of the not yet fully closed pores in the ice, which adds a minor influence of modern air to the gas. For now, this is hard to check, however, the trend

towards higher values closer to the pore close-off depth supports this interpretation. In summary, with contaminations below 2% resulting ^{39}Ar or ^{81}Kr ages can be corrected well with the ^{85}Kr results, as e.g. done in Ritterbusch et al. (2022). Nevertheless, as mentioned, ideas to lower the contamination are being implemented, see the outlook in section 9.5.

Δage and Gas Age at Pore Close-Off

The gas age-ice age difference (in the following referred to as Δage) stems from the formation of glacier ice. Under continuous accumulation at the top, the firn column builds up until the overlying weight compresses the firn to a point where the pores are not interconnected anymore. Above this pore close-off depth, the interstitial air is still in contact with atmospheric air and therefore younger than the surrounding ice matrix. Thus, there is a difference in the age of the glacier ice and the gas bubbles it contains. From this, it is directly understandable that the Δage is therefore a proxy for the thickness of the firn column and the accumulation rate.

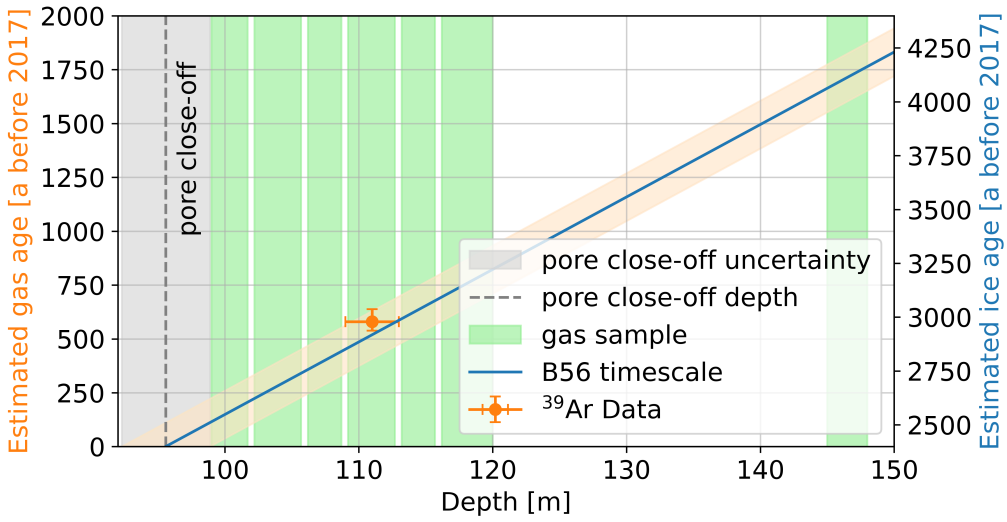

Figure 9.4: Plot of the ice age-depth timescale of the B56 ice core from Sagol et al. (2024) applying to the right ice age-axis. The orange data point depicts the measured ^{39}Ar age where the left age axis applies as gas age. Both y-axes are shifted such that a gas age of 0 a corresponds to the ice age at pore close-off depth (2399 a at 95.57 m). The light-orange shaded area around the timescale indicates the uncertainty range of the pore close-off depth, which translates to an uncertainty of the timescale on the gas age axis. The green areas mark the depth intervals of taken gas samples (listed in table 9.2).

Determining the Δage is especially important when studying atmospheric gas fluctuations and their timing (Schwander and Stauffer, 1984; Bender et al., 2006; Buizert et al., 2015). It can, however, also serve as its own proxy e.g. to determine past surface temperatures as proposed by Buizert (2021). The Δage is usually determined

from firn-densification modeling or ice flow modeling (Buizert et al., 2015), or empirically e.g. from synchronizing abrupt atmospheric methane variations from different datasets (Bender et al., 2006) or with volcanic deposits (Buizert et al., 2021). Δages for polar ice cores can reach up to a few ka while for Alpine regions, they are usually a few decades.
By measuring the ^{39}Ar abundance in an ice core, the gas age can be determined and compared to the ice age derived from other tracers. In the case of the B56 ice core, the sample B56_109_113 was analyzed for ^{39}Ar. In figure 9.4 the B56 timescale is plotted against the ice age (right axis), while the ^{39}Ar result is plotted against the gas age axis on the left. Both y-axis are shifted relative to each other so that a gas age of 0 a corresponds to the ice age of 2399 a of the timescale at the close-off depth (95.57 m). The uncertainty of the pore close-off depth, ±3.3 m, translates to an uncertainty in the timescale on the gas age axis and is indicated by the shaded light-orange area around the timescale. The B56 timescale within its gas-age uncertainty agrees well with the ^{39}Ar age. Thus, the gas age of the sample corroborates the B56 timescale and the value for the pore close-off depth. Furthermore, the slight tendency of the ^{39}Ar age towards older ages could be an indication of non-zero gas ages at the pore close-off depth. This would agree with the trend visible for the ^{85}Kr data in figure 9.3, where extrapolation of the increase of ^{85}Kr abundances towards the pore close-off depth does not seem to reach atmospheric values, although this is hard to quantify.

9.5 Summary and Outlook

The presented endeavor has successfully implemented a gas extraction unit for a conventional CFA system. With this discrete gas sampling system, gas for a subsequent ATTA analysis of ^{39}Ar as well as ^{85}Kr and ^{81}Kr can be sampled without the need for extra ice. This is an important step forward, as the ice amounts needed for an ATTA analysis still amount to several kilograms which have so far been melted entirely and thus lost for any further analysis. The gas extraction system fits into a large suitcase and can therefore readily be taken to any CFA laboratory when there is interest in dating with the mentioned tracers. Furthermore, as it is essentially a discrete gas sampling system the subsequent analysis is not limited to the ATTA tracers but can in theory be applied to any gaseous tracers that can be trapped at liquid nitrogen temperatures and that do not diffuse through the silicone tubing, as it might be the case for the very light species (H, He). Also, highly soluble gases like CO_2 would be problematic, as parts of the dissolved gas would not pass the membrane contactor but exit at the bottom of the debubbler towards the online analyses.
In order to validate the system, several tests have been conducted to quantify the gas extraction efficiency of the system and to evaluate potential contamination of atmospheric air. The gas extraction efficiency is highly influenced by the ratio of pump speed to melt speed, which can routinely be quite low in conventional CFA systems. Increasing the pump speed and thus the fraction of meltwater which is transported through the inner part of the CFA system, directly increases the gas

yield. However, attention has to be paid that the interface between the ice core and melt head never runs dry due to too high pump speeds. As a result, the gas yield from an Antarctic ice core was around 30 ml STP per meter of melted ice. This necessitates about 3 m of ice core for a 100 ml STP gas sample from which all three ATTA tracers can be measured.
The topic of contamination has been approached in two ways. First, bubble-free ice was melted and the extracted air was quantified and interpreted as a direct measure of contamination by atmospheric air. The evaluation resulted in values of around 1-2% of contamination relative to the expected gas yield of a real sample. Two samples with differing amounts of contamination give a hint that the contamination most probably originates from the transitions between the ice samples, which were not sufficiently flushed out.
Second, ^{85}Kr was measured on the extracted gas from an Antarctic ice core. Its abundances of about 1.5% of the atmospheric abundance in the samples away from the firn ice transition are interpreted as intruded atmospheric air and thus result in a very similar estimation of atmospheric air contamination as the test with bubble-free ice.

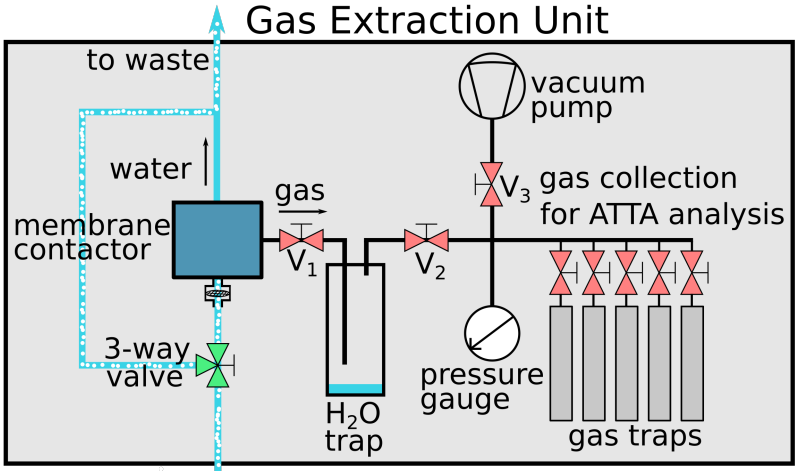

Figure 9.5: Gas extraction unit with an added three-way valve (green) before the membrane contactor. It can help to redirect the flow during each transition of ice samples and thus suppress the influence of atmospheric air in the membrane contactor.

This result is already satisfying and enables precise dating via ^{39}Ar and ^{81}Kr, enhanced by simultaneous measurements of ^{85}Kr to enable a correction for atmospheric contamination. However, a simple addition to the gas extraction unit can in the future help to reduce contamination originating from modern air entrapped in the membrane contactor after a crack/transition has passed through. Adding a three-way valve to the tube connecting the debubbler to the membrane contactor, see the green valve in figure 9.5, can enable the simple redirection of the flow of water and gas during each transition. Thus, the membrane contactor never gets in contact with contaminated air and therefore does not need to be flushed.
Furthermore, a better understanding of the process of the bubble close-off and of the

age distribution in the gas just above and below the firn-ice transition is necessary to interpret the data. Finding and applying models to these processes will be a next step in the analysis.
In summary, the gas extraction method is well quantified and should enable more efficient use of ice cores by enabling e.g. ATTA analysis without additional ice demands. This can potentially be important for projects like Beyond Epica Oldest Ice, where radiometric dating with ^{81}Kr can provide time constraints, especially in the unstratified bottom section, while the ice is so limited that even assigning 1 kg of ice for such an analysis is difficult.

10 Other Projects

While working on this thesis and supervising the ATTA 1 lab a multitude of samples from different projects were measured (compare table A.5). Some of them are part of PhD, master, or bachelor theses from colleagues of the HydroTrap research group and the ATTA collaboration of the IUP and the KIP. Other samples were part of collaborations with external partners who conducted other analyses and combined them with the ^{39}Ar data. Two of these projects are also related to ice dating and have thus been worked on in close collaboration with the author. They will be summarized in the following section. Both projects show the value of ^{39}Ar as an age-dating tracer bridging the gap between ^{14}C ages and modern tracers covering the past century.

10.1 Dôme du Goûter - French Alps

Already in 1999, an ice core was drilled at the Dôme du Goûter (DDG) in the French Alps and was finally analyzed in the past years. The project is led by colleagues from Université Grenoble Alpes, Grenoble, France, and from the Desert Research Institute, Reno, Nevada, USA. The detailed results are in the process of publication (Legrand et al., submitted) and are only shortly portrayed here with a focus on the dating effort.
Chemical analysis was conducted with a CFA system, measuring Na, Mg, P, S, Cl, Ca, Al, Fe, Ce, Pb, and NO_3, NH_4 as well as δ^{18}O. Concerning the dating of the ice core, radiocarbon was measured on the particulate organic carbon in twelve ice samples, and ^{39}Ar in the air bubbles of the ice was measured in five ice samples. Furthermore, distinct changes in heavy metals were used as tie points for age information. In figure 10.1, the age data is plotted against the depth of the ice core. The black line indicates a Bayesian age-depth model based on ^{137}Cs, and Pb data as well as four out of five ^{39}Ar and eleven out of twelve ^{14}C age data points (the oldest ^{39}Ar and ^{14}C data points not considered for the model because of their large age uncertainties. The oldest ^{14}C datapoint is not displayed in figure 10.1, it exhibits an age range of $\sim 4 - 36$ ka cal BP). In the plot, it can be seen how the uncertainties of the ^{14}C measurements become very large for ages < 1000 a. ^{39}Ar data fills this dating gap and shows a good agreement with the trend of the other tracers.
The significance of the dataset is quite high, as it is the first well-preserved ice core record from the European region dating back to the last climatic transition and the Younger Dryas. It provides aerosol records as well as sea-salt and dust deposition from the Younger Dryas through the Holocene, thus comprising information on changes in wind, vegetation, and aerosols in Europe.

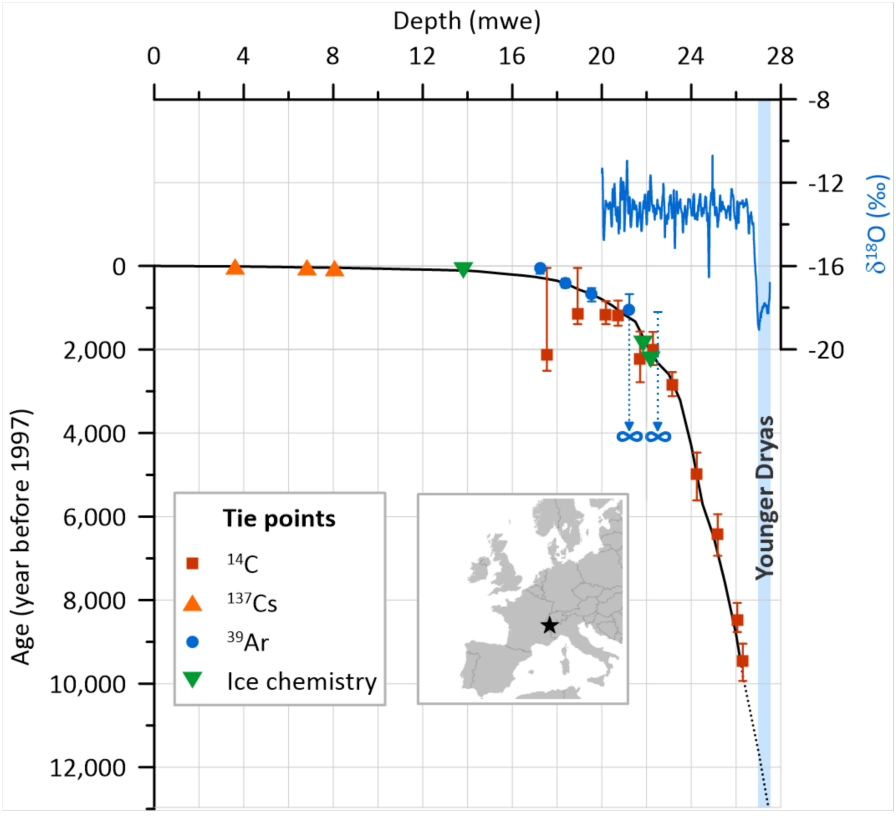

Figure 10.1: Dating of the DDG ice core from the French Alps. **Top:** deeper part of the $\delta^{18}O$ record. **Bottom:** Depth vs. age plot of the ^{14}C and ^{39}Ar measurements as well as other tie points. The solid black line indicates the Bayesian depth-age model. The dashed black line indicates a linear extrapolation of the age model based on $\delta^{18}O$ values. Figure adapted from Legrand et al. (submitted).

10.2 Foxfonna Ice Cap - Svalbard

In an effort to learn more about the glacial history of Svalbard, a horizontal ice core was retrieved from the Foxfonna ice cap, in May 2021. The project is led by colleagues from NILU, Norway, and Paul Scherrer Institute, Switzerland, and aims to extend the ice core records of Svalbard beyond the current 1200 a (Beaudon et al., 2013; Divine et al., 2011).

The Foxfonna ice cap is located close to Longyearbyen at an altitude of around 800 m a.s.l. and therefore offers easy accessibility by snowmobile. Recently, years of negative mass balance revealed concentric circles of isochrones, as seen in the top right of figure 10.2. Starting from the top, ice was taken from eight sampling locations in a line perpendicular to the isochrones. Samples from all locations were analyzed for radiocarbon in their dissolved organic carbon (DOC) and their water-insoluble organic carbon (WIOC) at Paul Scherrer Institute in Switzerland. Additionally, ^{39}Ar was measured for all except the lowermost sample.

In the left part of figure 10.2, the determined ages are plotted against the horizontal

distance from the ice cap summit (P1). The data nicely shows an age gradient downslope from the top, reaching from about 300 a cal BP to almost 2000 a cal BP. In the dataset, the DOC-^{14}C ages agree well with the ^{39}Ar data, while the ^{14}C-WIOC ages are overestimating the age. At the ice margin of the ice cap, dead moss was revealed by the retreating glacier and could be ^{14}C dated to ages around 1300 a cal BP and 1600 a cal BP. The age data shows that the Foxfonna ice cap offers convenient and low-effort access to almost 2000 a of Svalbard's climate history.
The project is ongoing and a detailed analysis will be published soon (Hartz et al., in preparation).

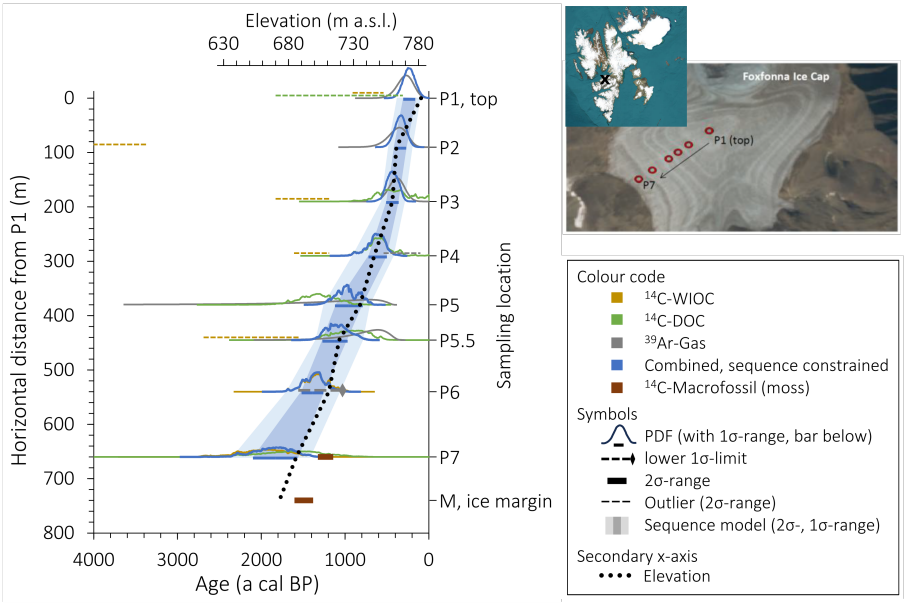

Figure 10.2: Left: Plot of the age dating results with ^{14}C-WIOC and -DOC as well as ^{39}Ar against the horizontal distance of sampling point P1 at the summit of the ice cap. Samples of dead moss from underneath the retreating ice cap were ^{14}C dated and are indicated as well. **Right:** Location of the Foxfonna ice cap and a satellite photo (toposvalbard.npolar.no) of the ice cap with the isochrones and indications of the sampling locations. Figure and overview of sampling locations courtesy to T. Jenk and W. Hartz. Overview map of Svalbard from sribblemaps.com.

11 Project Conclusion and Outlook

The work presented in this thesis can be separated into two main parts. The first aspect is the work in the field of atom optics in the ATTA laboratory, being concerned with the improvement of the experiment and the conduction of long-term measurement operations. Due to a large queue of environmental samples from various projects, this was the first and immediate focus. The performance of the ATTA apparatus had been significantly reduced since 2019 due to a larger hardware accident destroying the source chamber. Therefore, over the first two years of this PhD project, a focus was laid on optimizing the setup, finally regaining high count rates. The technical progress made during this stage of the project is summarized and is limited here to the key findings to enhance the performance. The main factor that was found to enhance the count rates to values of 6-7 ^{39}Ar atoms/h was the positioning of the collimator, which was evidently placed too far behind the metastable Ar source. Various other tests were conducted over time to characterize the apparatus and to test different parameters of the components. Furthermore, many parts of the laser system, electronic units, and vacuum components were changed and optimized to improve aspects like the monitoring system and performance stability. Also, a project to establish an online database for ATTA measurements was started with the computing division of the KIP, in close arrangement regarding progress and exact implementation. Listing all these steps goes beyond the constraints of a PhD thesis, however, several supervised bachelor and master theses are mentioned in the according sections and give an overview of the progress.
Besides the technical improvements, driven by the urgency of several environmental projects, longer intervals of sample measurements were conducted, including projects from groundwater, ocean, and first ice campaigns. Furthermore, a pilot study on the measurement of ^{39}Ar in the pore gas of permafrost was conducted, revealing enriched abundances with respect to the atmospheric value. This sparked several projects to build a better understanding of subsurface production of ^{39}Ar and its possibility to serve as a surface exposure dating tracer.
After reaching high count rates of 6-7 ^{39}Ar atoms/h again in spring 2023, a year of almost exclusive measurement operation commenced, providing many of the measurements this thesis is based on, but also from several other projects. In total 216 environmental samples were measured during the roughly 3.5 years during which the apparatus was supervised by the author.

The second aspect of this thesis is the application of the ^{39}Ar dating tracer to Alpine ice. The aim was to establish ^{39}Ar measurements as a well-understood and routinely applicable tracer for ice dating. To do so, several sampling campaigns were

conducted in close collaboration with the project partners from the Institute for Interdisciplinary Mountain Research in Innsbruck. This thesis presents two of these projects. One is concerned with the summit glacier of the Weissseespitze, where ^{14}C data was already available from a former publication. Adding ^{39}Ar data for the upper part of the ice column enabled the complete coverage of the age-depth profile with age data points and, thus, the fitting of an analytical age-depth model. A precise age scale reaching back more than 6000 a is established and can be applied to other depth-resolved tracer data. The second discussed project is about the low-altitude Jamtalferner glacier, a glacier that has experienced large advances and retreats in the last centuries, closely impacting human activities around it. ^{39}Ar data shows younger ages (< 200 a) for the intermediate part of the glacier and can resolve the older ages (> 300 a) at the tongue. In combination with ^{3}H data and surface exposure ages from moraines, based on ^{10}Be and pilot ^{39}Ar measurements, it can resolve the younger glacial history of the mountain valley.
In addition to these projects, two glacier applications led by external project partners have been worked on that will soon be published and which are only briefly summarized here. One provides a complete Holocene ice core record for Europe, and the other one extends the ice core record of Svalbard at an easy-access glacier site.
Besides the application of ^{39}Ar measurements to glaciers, two more fundamental aspects of ^{39}Ar dating of ice samples are addressed in this thesis. First, the question of possible atmospheric contamination of long-stored ice samples by diffusion of Ar into the ice is evaluated. The results show that there is no immediate problem for samples that are stored for a few decades at temperatures below -20° C. However, more precise measurements in the future are needed to further constrain this process. Second, the comparatively large ice consumption of an ATTA measurement was taken as a motivation to design, test, and apply a new gas extraction system. For valuable ice samples, the requirement of several kilograms of ice can cause a measurement of ^{39}Ar, or also ^{81}Kr, to be considered too costly. By presenting a gas extraction system that can be coupled to the waste line of a CFA, a method routinely applied to many ice cores, a measurement of ^{39}Ar or ^{81}Kr can in the future be conducted without any extra need of ice.

Many topics can be given as an outlook. On the technical side, the ATTA technology still needs further improvements to become a routinely applicable and reliably working method. Especially in the case of ^{39}Ar, there is an urgent need for higher count rates to reach higher precision. One of the major next steps will be the design of a magnetically enhanced discharge source as presented by Yan et al. (2023). Furthermore, many small improvements are needed to optimize the current design of the discharge source. A source design with lower liquid-nitrogen consumption and theoretically better cooling performance was already introduced by Robertz (2023), however, it yet needs to be fully characterized and equipped with an aluminum-nitride tube to exceed the performance of the current design. Furthermore, the thermal drifts of the current collimator are a well-known problem and should soon be reduced by implementing the new and more stable collimator design in the measurement lab.

Also, investigating the possibility of a helical-resonator type source, instead of the open antenna used at the moment could enhance the stability of the system. Other ATTA laboratories employ this design and do not experience thermal drifts of their collimator.
Parallel to the current ATTA setup, a new ATTA laboratory is being set up, offering the new capability to measure also ^{85}Kr. With two functional ATTA labs in the future, the contradiction of technical progress and routine measurements will hopefully soon be overcome.

A very different aspect might influence the dating with ^{39}Ar in the future. In a recent, although not yet peer-reviewed publication, DEAP Collaboration et al. (2025) have measured the half-life of ^{39}Ar in the DEAP-3600 detector on several thousand kg of Ar by decay detection. After 3.4 a of measurement time, their result amounts to $T_{1/2,^{39}\mathrm{Ar,new}} = (302 \pm 8_{\mathrm{stat}} \pm 6_{\mathrm{sys}})$ a. This is significantly different from the former result of 268 ± 3 from Golovko (2023) and would shift all ^{39}Ar ages towards older values. The publication also calculates a corrected atmospheric ^{39}Ar abundance of $(8.6 \pm 0.4) \times 10^{-16}$ ^{39}Ar/Ar.

Concerning the ice dating projects, several more samples are in the pipeline to be measured. For the age profile of the Weissseespitze, it is planned to measure more samples to create an overlap of ^{39}Ar and ^{14}C data. This will tie down the age-depth relationship even more and enable the direct comparison of the two tracers. For the Jamtalferner, measurements on an ice core from the summit of the glacier (Jamspitze) are planned, to get a better understanding of the higher part of the glacier system. With the hopefully soon-to-be-implemented capability of measuring ^{85}Kr, measurements from ice samples will become more reliable as any potential contamination with atmospheric air can be detected and corrected.

With the accelerating mass loss of glaciers in the Alps, the urgent need for further sampling campaigns to secure more records of this quickly disappearing archive is evident. The current campaigns will therefore surely be followed up by further projects where ^{39}Ar will play an important role in tying down the age distributions. With the now well-understood and well-controlled routines of sample selection, preparation, and measurement, the ATTA technology is ready to meet these needs.

A Appendix

Table A.1: AOM frequencies.

AOM	frequency [MHz]
Booster	194.0
ZSL	166.5
Col	208.0
MOT	206.0
1.RP	91.7
2.RP	211.3
Beat	120.0

Table A.2: Power supply parameters.

Power Supply	Voltage [V]	Current [I]
ZSL	47.5	11.4
MOT	20.0	10.2
MOL	0.4	1.25
Comp	16.0	4.6

Table A.3: Laser powers after TA fibers. The Greek letters are indicated in pink in figure 5.6 to give the position of the measurement. Values are given as lower limits which were usually aimed for when optimizing the setup before measurements.

Laserpath	Power [mW]
α	$>$590
β	$>$600
γ	$>$500
δ	$>$750

Table A.4: Laserpowers of each component and each frequency which have proven to ensure count rates around 6 ^{39}Ar atoms/h over more than one year and more than 100 sample measurements. The powers were measured in the fibers leading to the experiment, except the MOT H2 value that was measured in front of the respective in-coupler of the fiber bench (as the fiber bench was completely stable over the last years, the power in the H2 axis is directly related to the other MOT axes. The other axes are not as easily accessed with the current power meter). All values should not be interpreted as strict values, but rather as guidelines. Especially for the repumper frequencies, slightly lower powers have not shown any strong impact on the count rates.

Component	Cooler [mW]	RP1 [mW]	RP2 [mW]	RP3 [mW]
Col 1	210	20	25	7
Col 2	215	10	18	6
MOL H	17	12	17	
MOL V	26	12	13	
Quench	22			
ZSL	100			
Booster	19			
MOT H2	21	2.5	5	

Figure A.1: Titlepage of the Physik Journal, November 2021, showing a photo of the sampling campaign on the Jamtalferner. Photo taken by W. Aeschbach.

Figure A.2: Image of the ice surface at WSS summit, August 2022. A dust layer is melting out spatially homogeneously. Photo by A. Fischer.

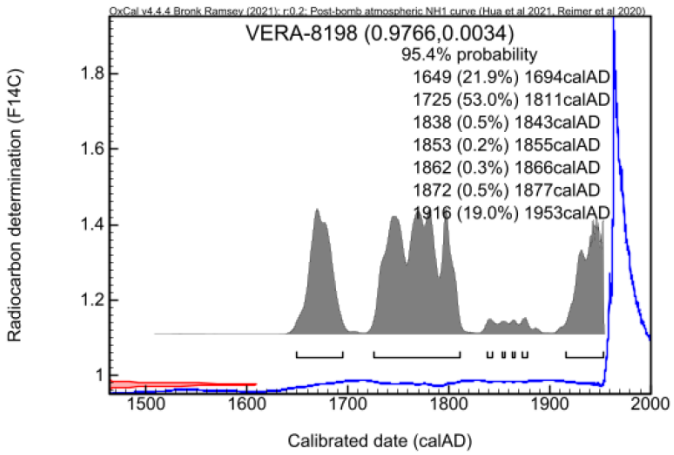

Figure A.3: Result of the 14C measurement from the wood piece from Urezzajoch. Analyzed with OxCal v4.4.4, measurement performed at the Vienna Environmental Research Accelerator facility.

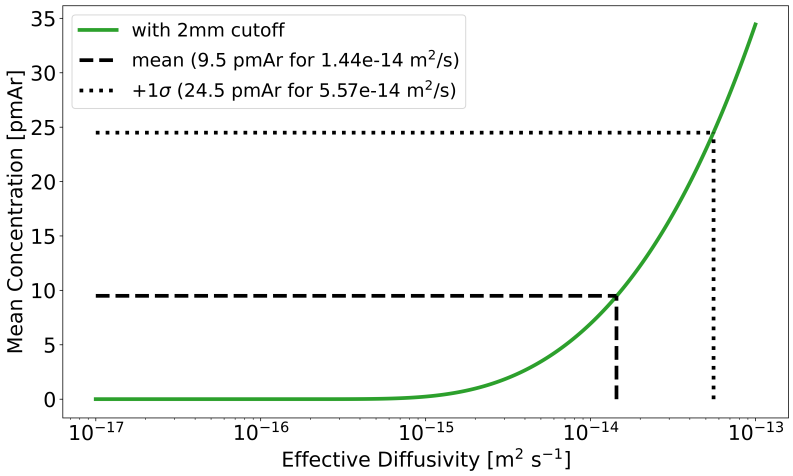

Figure A.4: Effective diffusivity vs. mean concentration for the DDG-test sample with 2 mm cutoff.

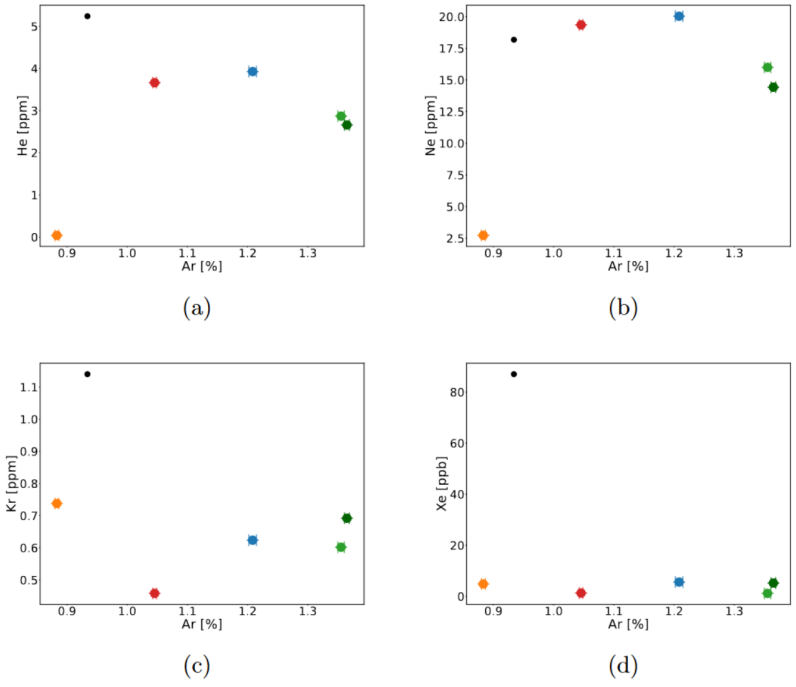

Figure A.5: Results for noble gas concentrations from the CFA leak tests with increased argon atmosphere around melthead and tube connections (compare section 9.3). The green, dark-green, and red data points are from samples with prepared large cracks and increased argon concentrations around the melt head. The orange data point is from a sample without obvious cracks and increased argon concentrations around the melt head. Blue is from the leak test of tube connections. Atomspheric ratios are indicated with a black dot. Plots taken from Marks (2024).

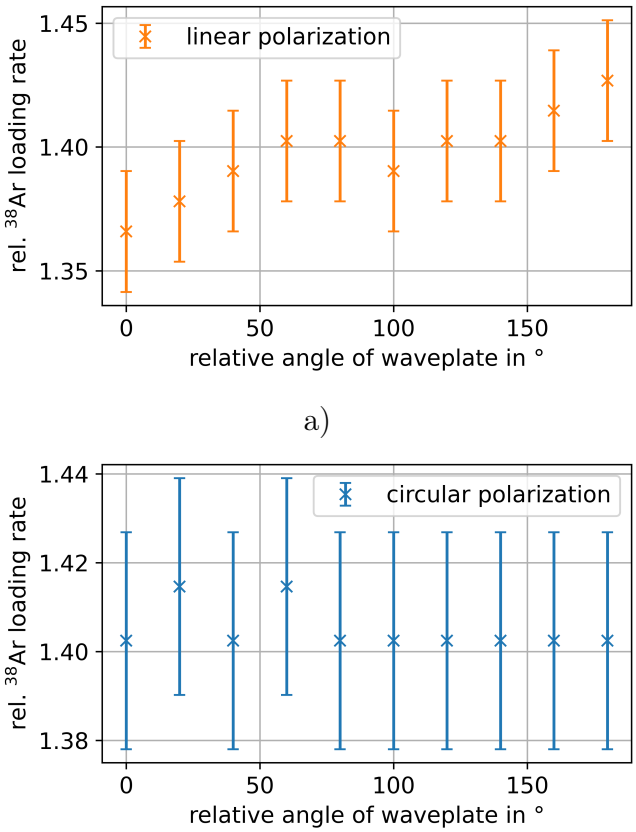

Figure A.6: The relative ^{38}Ar LR measured against the beam polarization of the pre-collimator molasses. **a)** for linear polarization, **b)** for circular polarization. Figure adapted from Kundy (2023).

Table A.5: List of all environmental samples measured during the author's supervision of the ATTA 1 lab.

Nr	Sample	Nr	Sample
1	Poly_Test	109	JamKern_P11_P12
2	Poly_upper	110	WSS_Surface_1+2
3	Poly_lower	111	StubaiKern_9to12
4	Auro_lower	112	StubaiBlock_6
5	Auro_upper	113	Svalbard_Foxfonna_P1
6	Permahot	114	HG2
7	ZeggeHO5	115	ETH Arktis 889
8	ZeggeHO6	116	Oregon_2
9	ZeggeHO7	117	ETH Arktis 888
10	ZeggeHO8	118	ETH Arktis 890
11	ZeggeHO9	119	ETH Arktis 589
12	ZeggeHO1	120	Arktis 46_4
13	ZeggeHO2	121	Arktis 28_10
14	ZeggeHO3	122	Arktis 28_8
15	HollandVO1	123	Arktis 46_4
16	Beitenholz01	124	Arktis 46_10
17	HollandHO4	125	Bermuda_12
18	HollandVT12	126	HG3
19	ZeggeHO13_water	127	Jam58
20	ZeggeHO10	128	Arktis_46_8
21	ZeggeHO11	129	Svalbard_Foxfonna_P1
22	HO12	130	Svalbard_Foxfonna_P2
23	HollandVT5	131	Arktis_46_6
24	HollandVT4	132	Arktis_46_8
25	HollandVT3	133	Arktis_46_10
26	Holland_HO11_2	134	CDG_41_01
27	HollandVT2	135	CDG_35a
28	HollandVT7	136	ETH481
29	HollandVT1	137	CDG_39
30	HollandVT8	138	Arktis_46_2
31	HollandVT6	139	CDG_34
32	HollandVT6	140	ETH_493
33	Oman#5	141	Arktis_46_6
34	Arktis_20_3_12	142	Arktis_46_12
35	jam1C	143	ETH_487
36	Arktis 20-3-18	144	ETH_487
37	Jam1C	145	CDG_36_37
38	Oman#8	146	StubaiKern_1to8
39	Oman#1	147	Arktis_46_12
40	Jam52	148	Arktis_46_2

41	Arktis 20-3-6
42	Belgien16C
43	SchwetzingenT7
44	Oman#2
45	Belgien54C
46	Belgien54C
47	SchwetzingenT4
48	Arktis-20-3-16
49	SchwetzingenE49_2
50	Jam59
51	Schwetzingen_E36_2
52	Arktis_20_3_2
53	SchwetzingenT1
54	Jam1C
55	Jam52
56	Arktis 20-3-14
57	HollandVO2
58	HollandVO3
59	HollandVO3
60	HollandVT10
61	Oman#4
62	HollandVT11
63	HollandVT13
64	HollandVT14
65	HollandVT9
66	HollandVT15
67	Holland VT17
68	HollandVT16
69	HollandVT18
70	HollandVT19
71	Oman#6
72	EST_Trigii2
73	OM20NSHQ14 9-29
74	Oman#10
75	Est_Modriku_1
76	Jam3B
77	EST_Trigii3B
78	EST_2789
79	EST_13675
80	EST_13675
81	OM20NSHQ14 9-29
82	SchwetzingenT1
83	Permahot_2
84	ColDuDome_test
149	ETH_585
150	StubaiBlock_6
151	Arktis_28_12
152	ETH_585
153	Arktis_28_6
154	Arktis_28_6
155	Svalbard_Foxfonna_P3
156	Svalbard_Foxfonna_P6
157	JamKern_P31_P32
158	Arktis_28_12
159	JamKern_P21_P22
160	Arktis_28_14
161	23_11_23_Arktis_28_14
162	Geo C
163	Arktis_28_2
164	Arktis_28_2
165	Jam_2B
166	ETH_490
167	ETH_490
168	Arktis_28_3
169	Jam 2B
170	Jam_Urezza_Block_A
171	Arktis_20_3_4
172	Arktis_20_3_10
173	Arktis_20_3_6
174	WSS_Kern_2023_1_Run_5
175	Arktis_20_3_16
176	ETH_489
177	WSS_Kern_2023_1_Run_1_2_upper3
178	ETH_489
179	WSS_Kern2023_1_Run_lower3_4
180	Jam_2B
181	SNI1_GP_PT2
182	Arktis_46_8
183	Arktis 20_3_2
184	ETH_494
185	ETH_494
186	PLM6PT4
187	Oman_9
188	ETH_489
189	Jam_23_05
190	Svalbard_Foxfonna_P3_2
191	Oman_8
192	cont_sample_1

85	Oman #9
86	Oman #22
87	Oman #29
88	Bermuda_12
89	Oregon_3
90	Oregon_6
91	Arktis_20_3_4
92	Arktis_20_3_8
93	Arktis_20_3_10
94	Arktis_20_3_20
95	Arktis_20_3_16
96	Arktis_20_3_12
97	Arktis_20_3_8
98	Arktis_20_3_2
99	Arktis_20_3_14
100	Sonklar_Surface_1
101	Arktis_28_3_10
102	Arktis_28_3_16
103	Bermuda_13
104	Bermuda_9
105	Arktis_28_3_8
106	Rock_1
107	Bermuda_14
108	Bermuda_14
193	ETH_488
194	ETH_488
195	Svalbard_Foxfonna_P4_2
196	Svalbard_Foxfonna_P5_2
197	Stei_10
198	Gran_grob_K1
199	Oman_2
200	Svalbard_Foxfonna_P8_2
201	Tödi_2_2
202	Toedi_1
203	WSS24_Oberflaechenprobe_B
204	ETH 584
205	Oman_10
206	WSS24_Oberflaechenprobe_A
207	ETH 583
208	WSS_24_Kern2_Probe1
209	WSS_24_Kern_1Probe_1
210	Stei 12-05
211	Jam 23_3
212	Gran feink 2
213	Gran_Feink_3
214	Jam_23_5B
215	Aro_1
216	Blank_rock

Bibliography

Arck, Y.: Development of a Krypton Separation Setup for Dating with Atom Trap Trace Analysis, master thesis, Heidelberg University, 2019.

Arck, Y.: Gas Tracer Techniques to Investigate Arctic Ocean Dynamics, Ph.D. thesis, Heidelberg University, 2024.

Baumbusch, C.: Preliminary Title: Gas extraction from Continuous Flow Analysis, bachelor thesis, Heidelberg University, in progress.

Beaudon, E., Moore, J. C., Martma, T., Pohjola, V. A., Wal, R. S. W. V. d., Kohler, J., and Isaksson, E.: Lomonosovfonna and Holtedahlfonna ice cores reveal east-west disparities of the Spitsbergen environment since AD 1700, Journal of Glaciology, 59, 1069–1083, https://doi.org/10.3189/2013JoG12J203, 2013.

Belostotskiy, S. G., Donnelly, V. M., Economou, D. J., and Sadeghi, N.: Spatially Resolved Measurements of Argon Metastable ($1s_5$) Density in a High Pressure Microdischarge Using Diode Laser Absorption Spectroscopy, IEEE Transactions on Plasma Science, 37, 852–858, https://doi.org/10.1109/TPS.2009.2015949, 2009.

Bender, M., Sowers, T., and Lipenkov, V.: On the concentrations of O_2, N_2, and Ar in trapped gases from ice cores, Journal of Geophysical Research: Atmospheres, 100, 18 651–18 660, https://doi.org/10.1029/94JD02212, 1995.

Bender, M. L., Floch, G., Chappellaz, J., Suwa, M., Barnola, J.-M., Blunier, T., Dreyfus, G., Jouzel, J., and Parrenin, F.: Gas age–ice age differences and the chronology of the Vostok ice core, 0–100 ka, Journal of Geophysical Research: Atmospheres, 111, https://doi.org/10.1029/2005JD006488, 2006.

Bender, M. L., Barnett, B., Dreyfus, G., Jouzel, J., and Porcelli, D.: The contemporary degassing rate of ^{40}Ar from the solid Earth, Proceedings of the National Academy of Sciences, 105, 8232–8237, https://doi.org/10.1073/pnas.0711679105, 2008.

Bereiter, B., Schwander, J., Lüthi, D., and Stocker, T. F.: Change in CO_2 concentration and O_2/N_2 ratio in ice cores due to molecular diffusion, Geophysical Research Letters, 36, https://doi.org/10.1029/2008GL036737, 2009.

Bereiter, B., Fischer, H., Schwander, J., and Stocker, T. F.: Diffusive equilibration of N_2, O_2 and CO_2 mixing ratios in a 1.5-million-years-old ice core, The Cryosphere, 8, 245–256, https://doi.org/10.5194/tc-8-245-2014, 2014.

Beyersdorfer, S.: Argon extraction from glacier ice and ocean water for dating with ^{39}Ar-ATTA, master thesis, Heidelberg University, 2016.

Bigler, M., Svensson, A., Kettner, E., Vallelonga, P., Nielsen, M. E., and Steffensen, J. P.: Optimization of High-Resolution Continuous Flow Analysis for Transient Climate Signals in Ice Cores, Environmental Science & Technology, 45, 4483–4489, https://doi.org/10.1021/es200118j, 2011.

Bogaerts, A. and Gijbels, R.: Modeling of metastable argon atoms in a direct-current glow discharge, Physical Review A, 52, 3743–3751, https://doi.org/10.1103/PhysRevA.52.3743, 1995.

Bohleber, P.: Alpine Ice Cores as Climate and Environmental Archives, in: Oxford Research Encyclopedia of Climate Science, Oxford University Press, ISBN 978-0-19-022862-0, https://doi.org/10.1093/acrefore/9780190228620.013.743, 2019.

Bohleber, P., Hoffmann, H., Kerch, J., Sold, L., and Fischer, A.: Investigating cold based summit glaciers through direct access to the glacier base: a case study constraining the maximum age of Chli Titlis glacier, Switzerland, The Cryosphere, 12, 401–412, https://doi.org/10.5194/tc-12-401-2018, 2018.

Bohleber, P., Schwikowski, M., Stocker-Waldhuber, M., Fang, L., and Fischer, A.: New glacier evidence for ice-free summits during the life of the Tyrolean Iceman, Scientific Reports, 10, 20 513, https://doi.org/10.1038/s41598-020-77518-9, 2020.

Böhm, H.: Das Paznauntal, Forschungen zur deutschen Landeskunde, Bundesforschungsanst. für Landeskunde und Raumordnung, Bonn-Bad Godesberg, 1970.

Bolzan, J. F.: Ice flow at the Dome C ice divide based on a deep temperature profile, Journal of Geophysical Research: Atmospheres, 90, 8111–8124, https://doi.org/10.1029/JD090iD05p08111, 1985.

Braumann, S. M., Schaefer, J. M., Neuhuber, S. M., Lüthgens, C., Hidy, A. J., and Fiebig, M.: Early Holocene cold snaps and their expression in the moraine record of the eastern European Alps, Climate of the Past, 17, 2451–2479, https://doi.org/10.5194/cp-17-2451-2021, 2021.

Breitenmoser, P., Beer, J., Brönnimann, S., Frank, D., Steinhilber, F., and Wanner, H.: Solar and volcanic fingerprints in tree-ring chronologies over the past 2000 years, Palaeogeography, Palaeoclimatology, Palaeoecology, 313-314, 127–139, https://doi.org/10.1016/j.palaeo.2011.10.014, 2012.

Brosi, A. R., Zeldes, H., and Ketelle, B. H.: ^{39}Ar beta-spectrum, Phys. Rev., 79, 1950.

Buizert, C.: The Ice Core Gas Age-Ice Age Difference as a Proxy for Surface Temperature, Geophysical Research Letters, 48, https://doi.org/10.1029/2021GL094241, 2021.

Buizert, C., Baggenstos, D., Jiang, W., Purtschert, R., Petrenko, V. V., Lu, Z.-T., Müller, P., Kuhl, T., Lee, J., Severinghaus, J. P., and Brook, E. J.: Radiometric ^{81}Kr dating identifies 120,000-year-old ice at Taylor Glacier, Antarctica, Proceedings of the National Academy of Sciences, 111, 6876–6881, https://doi.org/10.1073/pnas.1320329111, 2014.

Buizert, C., Cuffey, K. M., Severinghaus, J. P., Baggenstos, D., Fudge, T. J., Steig, E. J., Markle, B. R., Winstrup, M., Rhodes, R. H., Brook, E. J., Sowers, T. A., Clow, G. D., Cheng, H., Edwards, R. L., Sigl, M., McConnell, J. R., and Taylor, K. C.: The WAIS Divide deep ice core WD2014 chronology - Part 1: Methane synchronization (68–31 ka BP) and the gas age–ice age difference, Climate of the Past, 11, 153–173, https://doi.org/10.5194/cp-11-153-2015, 2015.

Buizert, C., Fudge, T. J., Roberts, W. H. G., Steig, E. J., Sherriff-Tadano, S., Ritz, C., Lefebvre, E., Edwards, J., Kawamura, K., Oyabu, I., Motoyama, H., Kahle, E. C., Jones, T. R., Abe-Ouchi, A., Obase, T., Martin, C., Corr, H., Severinghaus, J. P., Beaudette, R., Epifanio, J. A., Brook, E. J., Martin, K., Chappellaz, J., Aoki, S., Nakazawa, T., Sowers, T. A., Alley, R. B., Ahn, J., Sigl, M., Severi, M., Dunbar, N. W., Svensson, A., Fegyveresi, J. M., He, C., Liu, Z., Zhu, J., Otto-Bliesner, B. L., Lipenkov, V. Y., Kageyama, M., and Schwander, J.: Antarctic surface temperature and elevation during the Last Glacial Maximum, Science, 372, 1097–1101, https://doi.org/10.1126/science.abd2897, 2021.

Chen, C. Y., Li, Y. M., Bailey, K., O'Connor, T. P., Young, L., and Lu, Z.-T.: Ultrasensitive Isotope Trace Analyses with a Magneto-Optical Trap, Science, 286, 1139–1141, https://doi.org/10.1126/science.286.5442.1139, 1999.

Chu, S.: Nobel Lecture: The manipulation of neutral particles, Reviews of Modern Physics, 70, 685–706, https://doi.org/10.1103/RevModPhys.70.685, 1998.

Collon, P., Bichler, M., Caggiano, J., DeWayne Cecil, L., El Masri, Y., Golser, R., Jiang, C., Heinz, A., Henderson, D., Kutschera, W., Lehmann, B., Leleux, P., Loosli, H., Pardo, R., Paul, M., Rehm, K., Schlosser, P., Scott, R., Smethie, W., and Vondrasek, R.: Development of an AMS method to study oceanic circulation characteristics using cosmogenic ^{39}Ar, Nuclear Instruments and Methods in Physics Research Section B: Beam Interactions with Materials and Atoms, 223-224, 428–434, https://doi.org/10.1016/j.nimb.2004.04.081, 2004a.

Collon, P., Kutschera, W., and Lu, Z.-T.: Tracing Noble Gas Radionuclides in the Environment, Annual Review of Nuclear and Particle Science, 54, 39–67, https://doi.org/10.1146/annurev.nucl.53.041002.110622, 2004b.

Colucci, R. R., Bohleber, P., Aeschbach, W., Luetscher, M., Moseley, G. E., Wachs, D., Securo, A., Edwards, L. R., Manzan, S., Oberthaler, M. K., and Festi, D.: A multi-method approach to dating permanent cave ice deposits reveals ice of Little Ice Age origin in the Leupa Cave, in preparation.

Craig, H., Horibe, Y., and Sowers, T.: Gravitational Separation of Gases and Isotopes in Polar Ice Caps, Science, 242, 1675–1678, https://doi.org/10.1126/science.242.4886.1675, 1988.

Crank, J.: The mathematics of diffusion, Clarendon Press, Oxford, 2. edn., ISBN 0-19-853344-6 and 978-0-19-853344-3, 1975.

Cuffey, K. and Paterson, W. S. B.: The physics of glaciers, Butterworth-Heinemann/Elsevier, Burlington, MA, 4th edn., ISBN 978-0-12-369461-4, 2010.

Dallmayr, R., Goto-Azuma, K., Astrid Kjaer, H., Azuma, N., Takata, M., Schüpbach, S., and Hirabayashi, M.: A High-Resolution Continuous Flow Analysis System for Polar Ice Cores, Bulletin of Glaciological Research, 34, 11–20, https://doi.org/10.5331/bgr.16R03, 2016.

D'Amico, G., Pesce, G., and Sasso, A.: Field shift analysis of visible and near-infrared argon transitions, J. Opt. Soc. Am. B, 16, 1033–1038, https://doi.org/10.1364/JOSAB.16.001033, 1999.

DEAP Collaboration, Adhikari, P., Ajaj, R., Alpizar-Venegas, M., Amaudruz, P.-A., Anstey, J., Auty, D. J., Batygov, M., Beltran, B., Bina, C. E., Bonivento, W. M., Boulay, M. G., Bueno, J. F., Cadeddu, M., Cai, B., Cardenas-Montes, M., Chen, Y., Choudhary, S., Cleveland, B. T., Crampton, R., Daugherty, S., DelGobbo, P., Stefano, P. D., Dolganov, G., Doria, L., Duncan, F. A., Dunford, M., Ellingwood, E., Erlandson, A., Farahani, S. S., Fatemighomi, N., Fiorillo, G., Ford, R. J., Gahan, D., Gallacher, D., Garai, A., Abia, P. G., Garg, S., Giampa, P., Gimenez-Alcazar, A., Goeldi, D., Golovko, V. V., Gorel, P., Graham, K., Grobov, A., Hallin, A. L., Hamstra, M., Haskins, S., Hu, J., Hucker, J., Hugues, T., Ilyasov, A., Jigmeddorj, B., Jillings, C. J., Joy, A., Kaur, G., Kemp, A., Yazdi, M. K., Kuzniak, M., Zia, F. L., Lai, M., Langrock, S., Lehnert, B., LePage-Bourbonnais, J., Levashko, N., Lissia, M., Luzzi, L., Machulin, I., Maru, A., Mason, J., McDonald, A. B., McElroy, T., McLaughlin, J. B., Mielnichuk, C., Mirasola, L., Moharana, A., Monroe, J., Murray, A., Ng, C., Oliviero, G., Olszewski, M., Pal, S., Papi, D., Park, B., Perry, M., Pesudo, V., Pollmann, T. R., Rad, F., Rethmeier, C., Retiere, F., Garcia, I. R., Roszkowski, L., Santorelli, R., II, F. G. S., Seth, S., Shalamova, V., Skensved, P., Smirnova, T., Sobotkiewich, K., Sonley, T., Sosiak, J., Soukup, J., Stainforth, R., Stringer, M., Tang, J., Vazquez-Jauregui, E., Viel, S., Vyas, B., Walczak, M., Walding, J., Ward, M., Westerdale, S., Wormington, R., and Zuniga-Reyes, A.: Direct Measurement of the ^{39}Ar Half-life from 3.4 Years of Data with the DEAP-3600 Detector, https://doi.org/10.48550/arXiv.2501.13196, 2025.

Dietre, B., Walser, C., Lambers, K., Reitmaier, T., Hajdas, I., and Haas, J. N.: Palaeoecological evidence for Mesolithic to Medieval climatic change and anthropogenic impact on the Alpine flora and vegetation of the Silvretta Massif (Switzerland/Austria), Quaternary International, 353, 3–16, https://doi.org/10.1016/j.quaint.2014.05.001, 2014.

Divine, D., Isaksson, E., Martma, T., Meijer, H. A., Moore, J., Pohjola, V., van de Wal, R. S. W., and Godtliebsen, F.: Thousand years of winter surface air temperature variations in Svalbard and northern Norway reconstructed from ice-core data, Polar Research, 30, 7379, https://doi.org/10.3402/polar.v30i0.7379, 2011.

Ebser, S.: Optimierung und Stabilisierung von ^{39}Ar-ATTA bis hin zur erstmaligen Anwendung auf die Datierung natürlicher Wasserproben, diploma thesis, Heidelberg University, 2012.

Ebser, S.: Dating of Ice and Ocean Samples with Atom Trap Trace Analysis of ^{39}Ar, Ph.D. thesis, Heidelberg University, 2018.

Ebser, S., Kersting, A., Stoeven, T., Feng, Z., Ringena, L., Schmidt, M., Tanhua, T., Aeschbach, W., and Oberthaler, M. K.: ^{39}Ar dating with small samples provides new key constraints on ocean ventilation, Nature Communications, 9, 5046, https://doi.org/10.1038/s41467-018-07465-7, 2018.

Eichler, A., Schwikowski, M., Gäggeler, H. W., Furrer, V., Synal, H.-A., Beer, J., Saurer, M., and Funk, M.: Glaciochemical dating of an ice core from upper Grenzgletscher (4200 m a.s.l.), Journal of Glaciology, 46, 507–515, https://doi.org/10.3189/172756500781833098, 2000.

EPICA community members: Eight glacial cycles from an Antarctic ice core, Nature, 429, 623–628, https://doi.org/10.1038/nature02599, 2004.

Essell, H., Esper, J., Wanner, H., and Büntgen, U.: Rethinking the Holocene temperature conundrum, Climate Research, 92, 61–64, https://doi.org/10.3354/cr01735, 2024.

Feng, Z.: Implementierung einer Atomflussüberwachung für ^{39}Ar ATTA, bachelor thesis, Heidelberg University, 2012.

Feng, Z.: Quantum technological dating of glacier ice from the last millennium and a new self-contained facility for routine measurements, Ph.D. thesis, Heidelberg University, 2019.

Feng, Z., Ebser, S., Ringena, L., Ritterbusch, F., and Oberthaler, M. K.: Bichromatic force on metastable argon for atom-trap trace analysis, Physical Review A, 96, 013 424, https://doi.org/10.1103/PhysRevA.96.013424, 2017.

Feng, Z., Bohleber, P., Ebser, S., Ringena, L., Schmidt, M., Kersting, A., Hopkins, P., Hoffmann, H., Fischer, A., Aeschbach, W., and Oberthaler, M. K.: Dating glacier ice of the last millennium by quantum technology, Proceedings of the National Academy of Sciences, 116, 8781–8786, https://doi.org/10.1073/pnas.1816468116, 2019.

Ferreira, C. M., Loureiro, J., and Ricard, A.: Populations in the metastable and the resonance levels of argon and stepwise ionization effects in a low-pressure

argon positive column, Journal of Applied Physics, 57, 82–90, https://doi.org/10.1063/1.335400, 1985.

Festi, D., Schwikowski, M., Maggi, V., Oeggl, K., and Jenk, T. M.: Significant mass loss in the accumulation area of the Adamello glacier indicated by the chronology of a 46 m ice core, The Cryosphere, 15, 4135–4143, https://doi.org/10.5194/tc-15-4135-2021, 2021.

Fick, A.: Ueber Diffusion, Annalen der Physik, 170, 59–86, 1855.

Fischer, A., Hartl, L., Markl, G., and Kuhn, M.: Glacier mass balances and elevation zones of Jamtalferner, Silvretta, Austria, 1988/1989 et seq, https://doi.org/10.1594/PANGAEA.818772, 2016.

Fischer, A., Fickert, T., Schwaizer, G., Patzelt, G., and Groß, G.: Vegetation dynamics in Alpine glacier forelands tackled from space, Scientific Reports, 9, 13 918, https://doi.org/10.1038/s41598-019-50273-2, 2019.

Fischer, A., Schwaizer, G., Seiser, B., Helfricht, K., and Stocker-Waldhuber, M.: High-resolution inventory to capture glacier disintegration in the Austrian Silvretta, The Cryosphere, 15, 4637–4654, https://doi.org/10.5194/tc-15-4637-2021, 2021.

Fischer, A., Stocker-Waldhuber, M., Frey, M., and Bohleber, P.: Contemporary mass balance on a cold Eastern Alpine ice cap as a potential link to the Holocene climate, Scientific Reports, 12, 1331, https://doi.org/10.1038/s41598-021-04699-2, 2022.

Fourier, J. B. J.: Théorie analytique de la chaleur, 1822.

Fox, M.: Quantum optics, Oxford master series in physics, Oxford University Press, Oxford ; New York, ISBN 978-0-19-152425-7, 2006.

Friedrich, R.: Helium in polaren Eisschilden, diploma thesis, Heidelberg University, 2003.

Gabrielli, P., Barbante, C., Bertagna, G., Bertó, M., Binder, D., Carton, A., Carturan, L., Cazorzi, F., Cozzi, G., Dalla Fontana, G., et al.: Age of the Mt. Ortles ice cores, the Tyrolean Iceman and glaciation of the highest summit of South Tyrol since the Northern Hemisphere Climatic Optimum, The Cryosphere, 10, 2779–2797, https://doi.org/10.5194/tc-10-2779-2016, 2016.

Gäggeler, H., Gunten, H. R. v., Rössler, E., Oeschger, H., and Schotterer, U.: ^{210}Pb-Dating of Cold Alpine Firn/Ice Cores From Colle Gnifetti, Switzerland, Journal of Glaciology, 29, 165–177, https://doi.org/10.3189/S0022143000005220, 1983.

Golovko, V. V.: Application of the most frequent value method for ^{39}Ar half-life determination, The European Physical Journal C, 83, 930, https://doi.org/10.1140/epjc/s10052-023-12113-6, 2023.

Gordon Davy, J. and Miller, K. W.: The diffusion of helium through ice, Solid State Communications, 8, 1459–1461, https://doi.org/10.1016/0038-1098(70)90719-2, 1970.

Gu, J.-Q., Tong, A. L., Yang, G.-M., Hu, S.-M., Jiang, W., Lu, Z.-T., Purtschert, R., and Ritterbusch, F.: Reconstruction of the atmospheric ^{39}Ar/Ar history, Chemical Geology, 583, 120 480, https://doi.org/10.1016/j.chemgeo.2021.120480, 2021.

Haas, J., Bullemer, B., and Kahane, A.: Diffusion de l'helium dans la glace monocristalline, Solid State Communications, 9, 2033–2035, https://doi.org/10.1016/0038-1098(71)90354-1, 1971.

Haken, H. and Wolf, H. C.: Atom- und Quantenphysik, Springer-Lehrbuch, Springer, Berlin ; Heidelberg, ISBN 978-3-540-02621-1 and 3-540-02621-5 and 978-3-642-62142-0, https://doi.org/10.1007/978-3-642-18519-9, 2004.

Happel, J.: Rekonstruktion der historischen Inputfunktion von Argon-39 in der Atmosphäre, bachelor thesis, Heidelberg University, 2024.

Hartl, L., Felbauer, L., Schwaizer, G., and Fischer, A.: Small-scale spatial variability in bare-ice reflectance at Jamtalferner, Austria, The Cryosphere, 14, 4063–4081, https://doi.org/10.5194/tc-14-4063-2020, 2020.

Hartz, W., Jenk, T., Hodson, A., Wachs, D., Aeschbach, W., and Oberthaler, M.: Working title: Radiocarbon dating of a Svalbard horizontal ice core, in preparation.

Hawthorn, C. J., Weber, K. P., and Scholten, R. E.: Littrow configuration tunable external cavity diode laser with fixed direction output beam, Review of Scientific Instruments, 72, 4477–4479, https://doi.org/10.1063/1.1419217, 2001.

Hieronimus, E.: Estimation of the subsurface production rate of ^{39}Ar in soil using a permafrost sample analysed by Atom Trap Trace Analysis, bachelor thesis, Heidelberg University, 2022.

Hoffmann, H., Preunkert, S., Legrand, M., Leinfelder, D., Bohleber, P., Friedrich, R., and Wagenbach, D.: A New Sample Preparation System for Micro-^{14}C Dating of Glacier Ice with a First Application to a High Alpine Ice Core from Colle Gnifetti (Switzerland), Radiocarbon, 60, 517–533, https://doi.org/10.1017/RDC.2017.99, 2018.

Hoffmann, H. M.: Micro radiocarbon dating of the particulate organic carbon fraction in Alpine glacier ice: method refinement, critical evaluation and dating applications, Ph.D. thesis, Heidelberg University, 2016.

Hohensinner, S., Atzler, U., Fischer, A., Schwaizer, G., and Helfricht, K.: Tracing the Long-Term Evolution of Land Cover in an Alpine Valley 1820–2015 in the Light of Climate, Glacier and Land Use Changes, Frontiers in Environmental Science, 9, https://doi.org/10.3389/fenvs.2021.683397, 2021.

Hopkins, P.: Setting up a new argon seperation system for glacier ice and ocean water dating with ^{39}Ar-ATTA, master thesis, Heidelberg University, 2018.

Huber, C., Beyerle, U., Leuenberger, M., Schwander, J., Kipfer, R., Spahni, R., Severinghaus, J. P., and Weiler, K.: Evidence for molecular size dependent gas fractionation in firn air derived from noble gases, oxygen, and nitrogen measurements, Earth and Planetary Science Letters, 243, 61–73, https://doi.org/10.1016/j.epsl.2005.12.036, 2006.

Huhn, N.: Galtür und Ardez. Geschichte einer Spannungsreichen Partnerschaft, Ph.D. thesis, Innsbruck University, 1997.

IAEA: Live Chart of Nuclides, `https://www-nds.iaea.org/relnsd/vcharthtml/VChartHTML.html`, accessed on 06.12.2024, a.

IAEA: Water Isotope System for Electronic Retrieval (WISER) online database, `https://nucleus.iaea.org/wiser`, accessed on 06.02.2025, b.

Ikeda-Fukazawa, T., Horikawa, S., Hondoh, T., and Kawamura, K.: Molecular dynamics studies of molecular diffusion in ice Ih, The Journal of Chemical Physics, 117, 3886–3896, https://doi.org/10.1063/1.1495844, 2002.

Ikeda-Fukazawa, T., Kawamura, K., and Hondoh, T.: Diffusion of nitrogen gas in ice Ih, Chemical Physics Letters, 385, 467–471, https://doi.org/10.1016/j.cplett.2004.01.021, 2004a.

Ikeda-Fukazawa, T., Kawamura, K., and Hondoh, T.: Mechanism of Molecular Diffusion in Ice Crystals, Molecular Simulation, 30, 973–979, https://doi.org/10.1080/08927020410001709307, 2004b.

Ikeda-Fukazawa, T., Fukumizu, K., Kawamura, K., Aoki, S., Nakazawa, T., and Hondoh, T.: Effects of molecular diffusion on trapped gas composition in polar ice cores, Earth and Planetary Science Letters, 229, 183–192, https://doi.org/10.1016/j.epsl.2004.11.011, 2005.

Jenk, T. M., Szidat, S., Bolius, D., Sigl, M., Gäggeler, H. W., Wacker, L., Ruff, M., Barbante, C., Boutron, C. F., and Schwikowski, M.: A novel radiocarbon dating technique applied to an ice core from the Alps indicating late Pleistocene ages, Journal of Geophysical Research: Atmospheres, 114, https://doi.org/10.1029/2009JD011860, 2009.

Jiang, W., Williams, W., Bailey, K., Davis, A. M., Hu, S.-M., Lu, Z.-T., O'Connor, T. P., Purtschert, R., Sturchio, N. C., Sun, Y. R., and Mueller, P.: ^{39}Ar Detection at the 10^{-16} Isotopic Abundance Level with Atom Trap Trace Analysis, Physical Review Letters, 106, 103 001, https://doi.org/10.1103/PhysRevLett.106.103001, 2011.

Jiang, W., Bailey, K., Lu, Z. T., Mueller, P., O'Connor, T. P., Cheng, C. F., Hu, S. M., Purtschert, R., Sturchio, N. C., Sun, Y. R., Williams, W. D., and Yang, G. M.: An atom counter for measuring ^{81}Kr and ^{85}Kr in environmental samples, Geochimica et Cosmochimica Acta, 91, 1–6, https://doi.org/10.1016/j.gca.2012.05.019, 2012.

Jouzel, J., Masson-Delmotte, V., Cattani, O., Dreyfus, G., Falourd, S., Hoffmann, G., Minster, B., Nouet, J., Barnola, J. M., Chappellaz, J., Fischer, H., Gallet, J. C., Johnsen, S., Leuenberger, M., Loulergue, L., Luethi, D., Oerter, H., Parrenin, F., Raisbeck, G., Raynaud, D., Schilt, A., Schwander, J., Selmo, E., Souchez, R., Spahni, R., Stauffer, B., Steffensen, J. P., Stenni, B., Stocker, T. F., Tison, J. L., Werner, M., and Wolff, E. W.: Orbital and Millennial Antarctic Climate Variability over the Past 800,000 Years, Science, 317, 793–796, https://doi.org/10.1126/science.1141038, 2007.

Junkermann, A.: Ongoing PhD Project, Ph.D. thesis, Heidelberg University, in progress.

Kahane, A., Klinger, J., and Philippe, M.: Dopage Selectif De La Glace Monocristalline Avec De L'Helium Et Du Neon, Solid State Communications, 7, 1055–1056, https://doi.org/10.1016/0038-1098(69)90469-4, 1969.

Katori, H. and Shimizu, F.: Lifetime measurement of the $1s_5$ metastable state of argon and krypton with a magneto-optical trap, Physical Review Letters, 70, 3545–3548, https://doi.org/10.1103/PhysRevLett.70.3545, 1993.

Kaufmann, P. R., Federer, U., Hutterli, M. A., Bigler, M., Schüpbach, S., Ruth, U., Schmitt, J., and Stocker, T. F.: An Improved Continuous Flow Analysis System for High-Resolution Field Measurements on Ice Cores, Environmental Science & Technology, 42, 8044–8050, https://doi.org/10.1021/es8007722, 2008.

Kindermann, C.: Optimization of ArTTA: New Statistical Analysis and Investigation of the High Vacuum System, master thesis, Heidelberg University, 2024.

Kobashi, T., Ikeda-Fukazawa, T., Suwa, M., Schwander, J., Kameda, T., Lundin, J., Hori, A., Motoyama, H., Döring, M., and Leuenberger, M.: Post-bubble close-off fractionation of gases in polar firn and ice cores: effects of accumulation rate on permeation through overloading pressure, Atmospheric Chemistry and Physics, 15, 13 895–13 914, https://doi.org/10.5194/acp-15-13895-2015, 2015.

Krastel, J.: Laborexperimente zur diffusiven Ausgasung von Helium und Neon in Gletschereis und Datierung des Jamtalferners mit Hilfe der Argon Trap Trace Analyse, bachelor thesis, Heidelberg University, 2022.

Kundy, L.: Argon Trap Trace Analysis - Improved Transverse Laser Cooling and Investigation of Repumper Frequencies, master thesis, Heidelberg University, 2023.

Lal, D. and Peters, B.: Cosmic Ray Produced Radioactivity on the Earth, in: Kosmische Strahlung II / Cosmic Rays II, edited by Sitte, K., pp. 551–612,

Springer, Berlin, Heidelberg, ISBN 978-3-642-46079-1, https://doi.org/10.1007/978-3-642-46079-1_7, 1967.

Langenbacher, L.: ^{39}Ar Dating and Age-Depth Modelling the Weissseespitze Glacier Summit, bachelor thesis, Heidelberg University, 2024.

Legrand, M., McConnell, J. R., Preunkert, S., Wachs, D., Chellman, N. J., Rehfeld, K., Bergametti, G., Wensman, S. M., Aeschbach, W., Oberthaler, M., and Friedrich, R.: Alpine ice record of large dust, sea-salt, and biogenic aerosol changes over Europe during deglaciation, submitted.

Licciulli, C., Bohleber, P., Lier, J., Gagliardini, O., Hoelzle, M., and Eisen, O.: A full Stokes ice-flow model to assist the interpretation of millennial-scale ice cores at the high-Alpine drilling site Colle Gnifetti, Swiss/Italian Alps, Journal of Glaciology, 66, 35–48, https://doi.org/10.1017/jog.2019.82, 2020.

Liu, Z., Zhu, J., Rosenthal, Y., Zhang, X., Otto-Bliesner, B. L., Timmermann, A., Smith, R. S., Lohmann, G., Zheng, W., and Elison Timm, O.: The Holocene temperature conundrum, Proceedings of the National Academy of Sciences, 111, E3501–E3505, https://doi.org/10.1073/pnas.1407229111, 2014.

Loosli, H. H.: A dating method with ^{39}Ar, Earth and Planetary Science Letters, 63, 51–62, https://doi.org/10.1016/0012-821X(83)90021-3, 1983.

Loosli, H. H. and Oeschger, H.: Detection of ^{39}Ar in atmospheric argon, Earth and Planetary Science Letters, 5, 191–198, https://doi.org/10.1016/S0012-821X(68)80039-1, 1968.

Lu, Z.-T., Schlosser, P., Smethie, W., Sturchio, N., Fischer, T., Kennedy, B., Purtschert, R., Severinghaus, J., Solomon, D., Tanhua, T., and Yokochi, R.: Tracer applications of noble gas radionuclides in the geosciences, Earth-Science Reviews, 138, 196–214, https://doi.org/10.1016/j.earscirev.2013.09.002, 2014.

Marcott, S. A., Shakun, J. D., Clark, P. U., and Mix, A. C.: A Reconstruction of Regional and Global Temperature for the Past 11,300 Years, Science, 339, 1198–1201, https://doi.org/10.1126/science.1228026, 2013.

Marks, J.: ^{39}Ar dating of glacier ice: Improvement of the sample preparation, investigation of Ar diffusion in ice and glacier studies, master thesis, Heidelberg University, 2024.

Matthews, J. A. and Briffa, K. R.: The 'Little Ice Age': Re-Evaluation of an Evolving Concept, Geografiska Annaler: Series A, Physical Geography, 87, 17–36, https://doi.org/10.1111/j.0435-3676.2005.00242.x, 2005.

May, B. L.: Radiocarbon microanalysis on ice impurities for dating of Alpine glaciers, Ph.D. thesis, Heidelberg University, 2009.

McConnell, J. R., Lamorey, G. W., Lambert, S. W., and Taylor, K. C.: Continuous Ice-Core Chemical Analyses Using Inductively Coupled Plasma Mass Spectrometry, Environmental Science & Technology, 36, 7–11, https://doi.org/10.1021/es011088z, 2002.

Meienburg, F.: ^{39}Ar groundwater study in the Samail ophiolite, Oman in the context of carbon sequestration, master thesis, Heidelberg University, 2022.

Meienburg, F.: Ongoing PhD Project, Ph.D. thesis, Heidelberg University, in progress.

Metcalf, H. J. and van der Straten, P.: Laser Cooling and Trapping, Graduate Texts in Contemporary Physics, Springer New York, ISBN 978-0-387-98728-6 978-1-4612-1470-0, https://doi.org/10.1007/978-1-4612-1470-0, 1999.

Metcalf, H. J. and van der Straten, P.: Laser Cooling and Trapping, Graduate Texts in Contemporary Physics, Springer New York, ISBN 978-1-4612-1470-0, 2012.

Moraw, L.: Vacuum System Optimization for an Enhanced Metastable Argon Flux for ATTA, bachelor thesis, Heidelberg University, 2024.

Musy, S. and Purtschert, R.: Reviewing ^{39}Ar and ^{37}Ar underground production in shallow depths with implications for groundwater dating, Science of The Total Environment, 884, 163 868, https://doi.org/10.1016/j.scitotenv.2023.163868, 2023.

Musy, S., Casolaro, P., Dellepiane, G., Berger, A., Braccini, S., and Purtschert, R.: Quantification of ^{37}Ar emanation fractions from irradiated natural rock samples and field applications, Journal of Environmental Radioactivity, 251-252, 106 966, https://doi.org/10.1016/j.jenvrad.2022.106966, 2022.

NEEM community members: Eemian interglacial reconstructed from a Greenland folded ice core, Nature, 493, 489–494, https://doi.org/10.1038/nature11789, 2013.

Neukom, R., Steiger, N., Gomez-Navarro, J. J., Wang, J., and Werner, J. P.: No evidence for globally coherent warm and cold periods over the preindustrial Common Era, Nature, 571, 550–554, https://doi.org/10.1038/s41586-019-1401-2, 2019.

Neumann, F. P.: ^{39}Ar as a New Tracer for Surface Exposure Dating: A Pilot Study Using Atom Trap Trace Analysis, master thesis, Heidelberg University, 2024.

Nicolai, F.: Design and construction of a fiber-coupled tapered amplifier system, master thesis, Heidelberg University, 2017.

Nye, J. F.: The distribution of stress and velocity in glaciers and ice-sheets, Proceedings of the Royal Society of London. Series A. Mathematical and Physical Sciences, 239, 113–133, https://doi.org/10.1098/rspa.1957.0026, 1957.

Nye, J. F.: Correction Factor for Accumulation Measured by the Thickness of the Annual Layers in an Ice Sheet, Journal of Glaciology, 4, 785–788, https://doi.org/10.3189/S0022143000028367, 1963.

Oeschger, H., Gugelmann, A., Loosli, H., Schotterer, U., Siegenthaler, U., and Wiest, W.: ^{39}Ar dating of groundwater, in: Isotope techniques in groundwater hydrology 1974, Vol. II. Proceedings of a symposium, 1974.

Osman, M. B., Tierney, J. E., Zhu, J., Tardif, R., Hakim, G. J., King, J., and Poulsen, C. J.: Globally resolved surface temperatures since the Last Glacial Maximum, Nature, 599, 239–244, https://doi.org/10.1038/s41586-021-03984-4, 2021.

PAGES 2k Consortium: Continental-scale temperature variability during the past two millennia, Nature Geoscience, 6, 339–346, https://doi.org/10.1038/ngeo1797, 2013.

Pavlova, P. A., Jenk, T. M., Schmid, P., Bogdal, C., Steinlin, C., and Schwikowski, M.: Polychlorinated Biphenyls in a Temperate Alpine Glacier: 1. Effect of Percolating Meltwater on their Distribution in Glacier Ice, Environmental Science & Technology, 49, 14 085–14 091, https://doi.org/10.1021/acs.est.5b03303, 2015.

Pol, K., Masson-Delmotte, V., Johnsen, S., Bigler, M., Cattani, O., Durand, G., Falourd, S., Jouzel, J., Minster, B., Parrenin, F., Ritz, C., Steen-Larsen, H. C., and Stenni, B.: New MIS 19 EPICA Dome C high resolution deuterium data: Hints for a problematic preservation of climate variability at sub-millennial scale in the "oldest ice", Earth and Planetary Science Letters, 298, 95–103, https://doi.org/10.1016/j.epsl.2010.07.030, 2010.

Raab, E. L., Prentiss, M., Cable, A., Chu, S., and Pritchard, D. E.: Trapping of Neutral Sodium Atoms with Radiation Pressure, Physical Review Letters, 59, 2631–2634, https://doi.org/10.1103/PhysRevLett.59.2631, 1987.

Ramsey, C. B.: Radiocarbon Calibration and Analysis of Stratigraphy: The OxCal Program, Radiocarbon, 37, 425–430, https://doi.org/10.1017/S0033822200030903, 1995.

Rausch, R.: Das Periodensystem der Elemente online, `https://periodensystem-online.de`, accessed on 11.12.2024.

Rayleigh, L. and Ramsay, W.: Argon, a New Constituent of the Atmosphere, Philosophical Transactions of the Royal Society of London. A, 186, 187–241, 1895.

Raymond, C. F.: Deformation in the Vicinity of Ice Divides, Journal of Glaciology, 29, 357–373, https://doi.org/10.3189/S0022143000030288, 1983.

Reid, R.: The properties of gases and liquids, McGraw-Hill, 1966.

Reitmaier, T., Walser, C., Haas, J. N., and Dietre, B.: Alpine Archäologie in der Silvretta, Archäologie Schweiz, 2013.

Rhodes, R. H., Fain, X., Stowasser, C., Blunier, T., Chappellaz, J., McConnell, J. R., Romanini, D., Mitchell, L. E., and Brook, E. J.: Continuous methane measurements from a late Holocene Greenland ice core: Atmospheric and in-situ signals, Earth and Planetary Science Letters, 368, 9–19, https://doi.org/10.1016/j.epsl.2013.02.034, 2013.

Ricci, L., Weidemüller, M., Esslinger, T., Hemmerich, A., Zimmermann, C., Vuletic, V., König, W., and Hänsch, T. W.: A compact grating-stabilized diode laser system for atomic physics, Optics Communications, 117, 541–549, https://doi.org/10.1016/0030-4018(95)00146-Y, 1995.

Ringena, L. E.: Demonstration of a Dual Atom Trap Trace Analysis Setup for ^{39}Ar and ^{85}Kr, Ph.D. thesis, Heidelberg University, 2021.

Ritterbusch, F.: Realization of a collimated beam of metastable atoms for ATTA of Argon 39, diploma thesis, Heidelberg University, 2009.

Ritterbusch, F.: Dating of groundwater with Atom Trap Trace Analysis of ^{39}Ar, Ph.D. thesis, Heidelberg University, 2013.

Ritterbusch, F., Ebser, S., Welte, J., Reichel, T., Kersting, A., Purtschert, R., Aeschbach-Hertig, W., and Oberthaler, M. K.: Groundwater dating with Atom Trap Trace Analysis of ^{39}Ar, Geophysical Research Letters, 41, 6758–6764, https://doi.org/10.1002/2014GL061120, 2014.

Ritterbusch, F., Tian, L., Tong, A.-M., Gu, J.-Q., Jiang, W., Lu, Z.-T., Shao, L., Tang, M.-X., Yang, G.-M., Zhang, M.-J., and Zhao, L.: A Tibetan ice core covering the past 1,300 years radiometrically dated with ^{39}Ar, Proceedings of the National Academy of Sciences, 119, e2200835 119, https://doi.org/10.1073/pnas.2200835119, 2022.

Robertz, J.: Refining Argon Trap Trace Analysis - Crucial Features and Characterization Tools for Reliable Routine Measurements, Ph.D. thesis, Heidelberg University, 2023.

Röthlisberger, R., Bigler, M., Hutterli, M., Sommer, S., Stauffer, B., Junghans, H. G., and Wagenbach, D.: Technique for Continuous High-Resolution Analysis of Trace Substances in Firn and Ice Cores, Environmental Science & Technology, 34, 338–342, https://doi.org/10.1021/es9907055, 2000.

Sagol, F. K., Schwamborn, G., Freitag, J., Kipfstuhl, S., Wilhelms, F., and Hörhold, M.: Dating and interpreting a firn core from the East Antarctic Plateau, master thesis, Istanbul Technical University, 2024.

Satoh, K., Uchida, T., Hondoh, T., and Mae, S.: Diffusion Coefficient and Solubility Measurements of Noble Gases in Ice Crystals, in: Proc. NIPR Symp. Polar Meteorol. Glaciol., vol. 10, pp. 73–81, 1996.

Schaefer, J. M., Codilean, A. T., Willenbring, J. K., Lu, Z.-T., Keisling, B., Fülöp, R.-H., and Val, P.: Cosmogenic nuclide techniques, Nature Reviews Methods Primers, 2, 18, https://doi.org/10.1038/s43586-022-00096-9, 2022.

Schmidt: Investigations of Lake Kivu with ^{39}Ar Atom Trap Trace Analysis, Ph.D. thesis, Heidelberg University, 2021.

Schüpbach, S., Federer, U., Kaufmann, P. R., Hutterli, M. A., Buiron, D., Blunier, T., Fischer, H., and Stocker, T. F.: A New Method for High-Resolution Methane Measurements on Polar Ice Cores Using Continuous Flow Analysis, Environmental Science & Technology, 43, 5371–5376, https://doi.org/10.1021/es9003137, 2009.

Schwander, J. and Stauffer, B.: Age difference between polar ice and the air trapped in its bubbles, Nature, 311, 45–47, https://doi.org/10.1038/311045a0, 1984.

Schwenzer, S.: Composition and Characterisation of an Absolute Metastable ^{40}Ar Flux Measurement, bachelor thesis, Heidelberg University, 2022.

Sowers, T., Bender, M., and Raynaud, D.: Elemental and isotopic composition of occluded O_2 and N_2 in polar ice, Journal of Geophysical Research: Atmospheres, 94, 5137–5150, https://doi.org/10.1029/JD094iD04p05137, 1989.

Spagnesi, A., Bohleber, P., Barbaro, E., Feltracco, M., De Blasi, F., Dreossi, G., Stocker-Waldhuber, M., Festi, D., Gabrieli, J., Gambaro, A., Fischer, A., and Barbante, C.: Preservation of chemical and isotopic signatures within the Weißseespitze millennial old ice cap (Eastern Alps), despite the ongoing ice loss, Frontiers in Earth Science, 11, https://doi.org/10.3389/feart.2023.1322411, 2023a.

Spagnesi, A., Wachs, D., Marks, J., Urbach, K., Aeschbach, W., Bohleber, P., Fischer, A., Gabrieli, J., and Barbante, C.: The novel CFA - cryotrap coupling for ^{39}Ar extraction from ice cores' air bubbles: technical notes and preliminary approach, internal report (CNR ISP), 2023b.

Steinhilber, F., Abreu, J. A., Beer, J., Brunner, I., Christl, M., Fischer, H., Heikkilä, U., Kubik, P. W., Mann, M., McCracken, K. G., Miller, H., Miyahara, H., Oerter, H., and Wilhelms, F.: 9,400 years of cosmic radiation and solar activity from ice cores and tree rings, Proceedings of the National Academy of Sciences, 109, 5967–5971, https://doi.org/10.1073/pnas.1118965109, 2012.

Stowasser, C., Buizert, C., Gkinis, V., Chappellaz, J., Schüpbach, S., Bigler, M., Fain, X., Sperlich, P., Baumgartner, M., Schilt, A., and Blunier, T.: Continuous measurements of methane mixing ratios from ice cores, Atmospheric Measurement Techniques, 5, 999–1013, https://doi.org/10.5194/amt-5-999-2012, 2012.

Suwa, M. and Bender, M. L.: O_2/N_2 ratios of occluded air in the GISP2 ice core, Journal of Geophysical Research: Atmospheres, 113, https://doi.org/10.1029/2007JD009589, 2008.

Talalay, P., Yang, C., Cao, P., Wang, R., Zhang, N., Fan, X., Yang, Y., and Sun, Y.: Ice-core drilling problems and solutions, Cold Regions Science and Technology, 120, 1–20, https://doi.org/10.1016/j.coldregions.2015.08.014, 2015.

Tian, L., Ritterbusch, F., Gu, J.-Q., Hu, S.-M., Jiang, W., Lu, Z.-T., Wang, D., and Yang, G.-M.: ^{81}Kr Dating at the Guliya Ice Cap, Tibetan Plateau, Geophysical Research Letters, 46, 6636–6643, https://doi.org/10.1029/2019GL082464, 2019.

Trautmann, A.: Feshbach Spectroscopy of Sodium and Sodium-Lithium Mixtures, diploma thesis, Heidelberg University, 2011.

Uglietti, C., Zapf, A., Jenk, T. M., Sigl, M., Szidat, S., Salazar, G., and Schwikowski, M.: Radiocarbon dating of glacier ice: overview, optimisation, validation and potential, The Cryosphere, 10, 3091–3105, https://doi.org/10.5194/tc-10-3091-2016, 2016.

Urbach, K. L.: Making the most of ice samples: argon extraction with membrane contactors within a continuous flow analysis system, bachelor thesis, Heidelberg University, 2023.

von Reventlow, B.: Argon diffusion in glacier ice, bachelor thesis, Heidelberg University, 2022.

Wanner, H., Beer, J., Bütikofer, J., Crowley, T. J., Cubasch, U., Flückiger, J., Goosse, H., Grosjean, M., Joos, F., Kaplan, J. O., Küttel, M., Müller, S. A., Prentice, I. C., Solomina, O., Stocker, T. F., Tarasov, P., Wagner, M., and Widmann, M.: Mid- to Late Holocene climate change: an overview, Quaternary Science Reviews, 27, 1791–1828, https://doi.org/10.1016/j.quascirev.2008.06.013, 2008.

Wanner, H., Mercolli, L., Grosjean, M., and Ritz, S. P.: Holocene climate variability and change; a data-based review, Journal of the Geological Society, 172, 254–263, https://doi.org/10.1144/jgs2013-101, 2015.

Wanner, H., Pfister, C., and Neukom, R.: The variable European Little Ice Age, Quaternary Science Reviews, 287, 107 531, https://doi.org/10.1016/j.quascirev.2022.107531, 2022.

Weinhart, A. H., Freitag, J., Hörhold, M., Kipfstuhl, S., and Eisen, O.: Representative surface snow density on the East Antarctic Plateau, The Cryosphere, 14, 3663–3685, https://doi.org/10.5194/tc-14-3663-2020, 2020.

Welte, J.: Atom Trap Trace Analysis of ^{39}Ar, Ph.D. thesis, Heidelberg University, 2011.

Welte, J., Steinke, I., Henrich, M., Ritterbusch, F., Oberthaler, M. K., Aeschbach-Hertig, W., Schwarz, W. H., and Trieloff, M.: Hyperfine spectroscopy of the $1s_5$-$2p_9$ transition of ^{39}Ar, Review of Scientific Instruments, 80, 113 109, https://doi.org/10.1063/1.3257691, 2009.

Welte, J., Ritterbusch, F., Steinke, I., Henrich, M., Aeschbach-Hertig, W., and Oberthaler, M. K.: Towards the realization of atom trap trace analysis for ^{39}Ar, New Journal of Physics, 12, 065 031, https://doi.org/10.1088/1367-2630/12/6/065031, 2010.

Winkelvoß, M.: Compact Beam Combiner Setup without Power Loss for Laser Beams of same Wavelength, bachelor thesis, Heidelberg University, 2021.

Winkelvoß, M.: Design and Characterization of a Mechanically Robust Atom Beam Collimator for Atom Trap Trace Analysis, master thesis, Heidelberg University, 2024.

Xu, J., Calaprice, F., Galbiati, C., Goretti, A., Guray, G., Hohman, T., Holtz, D., Ianni, A., Laubenstein, M., Loer, B., Love, C., Martoff, C. J., Montanari, D., Mukhopadhyay, S., Nelson, A., Rountree, S. D., Vogelaar, R. B., and Wright, A.: A study of the trace ^{39}Ar content in argon from deep underground sources, Astroparticle Physics, 66, 53–60, https://doi.org/10.1016/j.astropartphys.2015.01.002, 2015.

Yan, J.-W., Li, H., Jiang, W., Lu, Z.-T., Ritterbusch, F., and Yang, G.-M.: A magnetically enhanced RF discharge source for metastable krypton production, Review of Scientific Instruments, 94, 033 202, https://doi.org/10.1063/5.0142696, 2023.

Yan, Y., Bender, M. L., Brook, E. J., Clifford, H. M., Kemeny, P. C., Kurbatov, A. V., Mackay, S., Mayewski, P. A., Ng, J., Severinghaus, J. P., and Higgins, J. A.: Two-million-year-old snapshots of atmospheric gases from Antarctic ice, Nature, 574, 663–666, https://doi.org/10.1038/s41586-019-1692-3, 2019.

Yi, Y. S. and Han, Y.: Theoretical Insights into Gas Migration Within Ice on Earth and Icy Celestial Bodies, ACS Earth and Space Chemistry, 8, 2611–2620, https://doi.org/10.1021/acsearthspacechem.4c00266, 2024.

Zappala, J. C.: Atom Trap Trace Analysis: Developments & Applications, Ph.D. thesis, University of Chicago, 2017.

Zehenter, P.: Characterization of a Magnetically Enhanced RF Discharge Source for ArTTA, bachelor thesis, Heidelberg University, 2024.

Danksagung

Ich kann mich noch gut daran erinnern, dass ich mir am Anfang dieser Doktorarbeit gar nicht so recht vorstellen konnte mich für 4 Jahre einem Projekt zu verpflichten. Gleichzeitig hatte ich extreme Lust darauf endlich mal mit viel Zeit tief in ein Thema einzusteigen und zu versuchen es zu durchsteigen, anders als die zig Themen die man im Studium immer nur in groben Umrissen kennengelernt hat. Jetzt, am Ende der 4 Jahre bin ich extrem dankbar für die Möglichkeit die mir geboten wurde. Mit so vielen tollen Kollegen und Mitmenschen in ein spannendes neues Thema einzusteigen, an zwei Instituten beheimatet zu sein und sich überall als Teil ein größeren Ganzen zu sehen ist ein absolutes Privileg.

Zu allererst, möchte ich meinen Betreuern danken. Einmal Werner Aeschbach, der mir die Möglichkeit geboten hat in seiner Gruppe nach meiner Masterarbeit auch meine Doktorarbeit zu machen. Bei dem ich jederzeit an die Tür klopfen konnte wenn ich eine Frage hatte und der mich in seiner Ruhe immer bestärkt hat. Außerdem Markus Oberthaler, in dessen Gruppe und Labor ich gelandet bin, der mich mit offenen Armen willkommen geheißen hat und von dessen Leidenschaft und Wissbegierde ich sehr profitiert habe.
Vielen Dank Norbert Frank, bei dem ich nicht nur meine erste Vorlesung zur Umweltphysik gehört habe, sondern der die Zweitkorrektur dieser Arbeit übernommen hat.
Ich hatte das Glück in einer tollen Kollaboration mit Kollegen von anderen Instituten zusammenarbeiten zu können. Für das Einführen in die Gletscher- und Eisthematik, die vielseitige Unterstützung und die schönen Probenkampagnen in den Bergen bedanke ich mich bei Andrea Fischer und Martin Stocker-Waldhuber und ganz besonders bei Pascal Bohleber.
Und dann natürlich ein großer Dank an die zwei Arbeitsgruppen, die HydroTrapper und Matterwaver, von denen ich Teil sein durfte. Die Arbeitsatmosphäre war immer so freundschaftlich, dass man eigentlich gar nicht von *Arbeits*atmosphäre sprechen kann. So viele spannende Projekte habe ich im Umgang mit allen kennengelernt und dadurch immer weiteres Interesse auch in anderen Themen entwickeln können. Nicht zu vergessen die unzähligen Freitagsfrühstücke, Doktorhutbauabende und pfälzer Weinfeste.
Ganz im besonderen gilt der Dank aber der ATTA-Gruppe. Ich könnte mir kein besseres Team vorstellen. Angefangen mit meinen VorgängerInnen Max und Lisa, die mir in den ersten harten Monaten im ATTA Labor unter die Arme gegriffen haben. Meinen langjährigen Mitstreitern Julian und Florian, und später auch Niclas und Alex, die in der Zeit mehr Freunde als Kollegen geworden sind und mit denen wir noch jedes Problem im Labor lösen konnten. Und ganz besonders Yannis, der schon

seit meiner Masterarbeitszeit immer für gute Gespräche über Gott und die Welt, fleißiges Probenmessen und genaues Korrekturlesen zu haben war. Und natürlich allen anderen Gruppenmitgliedern die über die Jahre das Arbeiten bereichert haben und mich an allen Ecken und Enden unterstützt haben. Auch Florian Ritterbusch, dem ATTA-Urgestein, möchte ich für den Input, die interessanten Gespräche und die tolle Zusammenarbeit am CFA-Projekt danken.
Ohne die Unterstützung in den Instituten durch die Werkstätten und die Verwaltung wäre diese Arbeit niemals möglich gewesen. Ganz besonderer Dank geht da an Christiane Jäger, Knut Azeroth, David Jansen und Julia Bing vom KIP, sowie Rebekka Benetatos und Angelika Gassama vom IUP.
Noch ein großer Dank an all die tollen Menschen die mein Leben bereichern, meine Wg, Boulderaffen und Bastelbrüder, Freunde und Verwandte.
Zuletzt, aber eigentlich an erster Stelle geht mein Dank an meine Eltern, Schwester und an Mareike, dafür dass ihr an meiner Seite seid und mir ermöglicht der Mensch zu sein der ich bin.

Erklärung

Ich versichere, dass ich diese Arbeit selbstständig verfasst habe und keine anderen als die angegebenen Quellen und Hilfsmittel benutzt habe.

Heidelberg, den 03.03.2025 .....